Multiphysics-based Fluidic Manipulation of Particles: An Experimental and Numerical Study

by
Yu Deng

A dissertation submitted to the Department of Mechanical Engineering,
Cullen College of Engineering
in partial fulfillment of the requirements for the degree of

DOCTOR OF PHILOSOPHY

in Mechanical Engineering

Chair of Committee: Dong Liu

Committee Member: Li Sun

Committee Member: Tsorng-Whay Pan

Committee Member: Di Yang

Committee Member: Cunjiang Yu

University of Houston
December 2020

ACKNOWLEDGMENTS

I would like to express my greatest gratitude and appreciation to my advisor, Dr. Dong Liu, Professor of Mechanical Engineering at University of Houston, for all his guidance and help throughout the projects in my entire graduate study. Dr. Liu is always generous of giving his encouragement and sharing his knowledge, which motivated me in pursuit of more rigorous attitude towards scientific research and my life.

This research was supported by the National Science Foundation (Grant No. 1134119). I would like to acknowledge this support and the financial support from University of Houston.

Finally, I would also like to thank my family for being so supportive during the course of my graduate education.

ABSTRACT

Noninvasive manipulation of various bioparticles, such as cells, enables their use as the building blocks to construct complex bioscaffold for tissue engineering, which has the potential to transform the basic research in biology/biomedicine as well as the clinical treatment of some intractable diseases. This dissertation aims at exploiting neural stem cells (NSCs) impregnated with superparamagnetic iron oxide nanoparticles (SPIONs), to develop an effective cure for spinal cord injury (SCI). In SCI patients, long distance axonal connections are lost because most axons in the adult mammalian central nervous system fail to regenerate after injury. Using an external magnetic field, the SPIONs labeled NSCs will spontaneously self-assemble into structured lattices along a *virtual* axis defined by the field flux lines, thereby forming a scaffold to guide the directional regrowth of axons.

In the first part of this work, *in vitro* experiments were conducted to (1) establish the procedures for SPIONs impregnation and (2) to evaluate the toxicity of SPIONs and the morphology and proliferation of the two-dimensional (2D) and three-dimensional (3D) bioscaffold self-assembled by SPIONs labeled 3T3 cells and NSCs. The experimental data proves the efficacy of the proposed approach in fabricating injectable and alignable bioscaffold for neural tissue engineering, and also prepare the context for the fundamental study of external-field-driven particle manipulation.

In the second part of this work, a multiphysics numerical framework was formulated to investigate the aggregation kinetics and pattern formation of particles in a fluid medium. In view of the similarities between electrostatic and magnetostatic fields, both electric and magnetic driving mechanisms, dielectrophoresis (DEP) and

magnetophoresis (MAP) were considered. The arbitrary Lagrangian-Eulerian (ALE) method coupled with Maxwell stress Tensor (MST) approach was applied to solve the particle-fluid-field interaction problem, in which the motion of the particles (both translation and rotation), the flow field and the external electric/magnetic field are closely coupled.

The insights gained from the experimental and theoretical studies of this work will help to advance the fundamental understanding of externally-driven field-particle interactions and the particle self-assembly process. This work also provides a potential tool to further medical treatment of SCI and other regenerative diseases in a noninvasive manner.

TABLE OF CONTENTS

LIST OF TABLES

LIST OF FIGURES

Chapter 1. Introduction

The motivation of this PhD dissertation came first from the urgent call for effective cure of spinal cord injury (SCI), which, as a primary nervous system disorder, has caused severe and chronic debilitation or even permanent disability to millions of people in the US and worldwide. SCI is difficult to heal partially because the central nervous system (CNS) has very limited capacity to repair itself after an injury. Mature CNS neurons have an intrinsic indolence to regenerate, for instance, the injured axons attempt to regenerate spontaneously but quickly lose the ability to do so within 24 hours after failing to grow across an injury gap [1,2]. Consequently, when the entire cross section of the spinal cord is replaced with scar tissues and/or fluid-filled cysts, the mechanical substrates that provide physical support for axonal regeneration and the three-dimensional cytoarchitectural information will be lost permanently [3,4]. As a promising solution, bioscaffolds grafted with neural stem cells (NSCs) have been explored to promote axonal regeneration in SCI, with which NSCs replace the lost neurons and oligodendrocytes to stimulate the axonal remyelination and the scaffolds restore the structural support for the NSCs and also sustains a controlled biochemical microenvironment to induce the NSC differentiation [5-8]. However, at present, virtually all bioscaffolds are made of polymer composites and have to be fabricated *in vitro* in the form of porous matrix or guidance microconduits. Subsequently, the bioscaffolds are implanted into the injured spinal cord through invasive surgical operations, which adds significantly to the physiological and psychological sufferings of the SCI patients.

Inspired by this critical challenge, the first half of this dissertation is devoted to developing a novel strategy to fabricate injectable, alignable, and bioactive scaffolds that use NSCs as the building blocks for axonal regeneration after SCI. The concept capitalizes on the ability to manipulate superparamagnetic iron oxide nanoparticles (SPIONs) with magnetic field remotely and noninvasively. The SPIONs-labeled NSCs will be injected into the injured spinal cord in colloidal suspensions. Upon the application of a magnetic field, magnetically labeled NSCs will spontaneously self-assemble into chain/column lattices and align along a *virtual* axis defined by the field flux lines, thereby forming a scaffold to guide the directional regrowth of axons. The objective of the experimental aspect of the dissertation is to demonstrate magnetic directed self-assembly of two types of cell lines into highly aligned structures for the purpose of guiding directional growth of axons in SCI therapy and creating various cellular structures useful for other tissue engineering applications.

In order to better understand the dynamics of magnetically-induced cellular alignment and pattern formation, the transport processes are formulated as a generalized multiphysics, multiphase flow problem in the second half of this dissertation. With this treatment, the NSCs are only a special case of solid phase, i.e., they are represented as "irregular-shaped particles" that meet desired properties whereas "regular particles" are usually spheres, and the external fields can be either magnetic or electric to allow both magnetokinetic and electrokinetic effects to be considered. The purpose of this generalization is to establish an universal framework for studying particle-field-flow interaction problems in a broader range of engineering applications involving particle manipulation. The particle-field-flow coupling arises from the fact that the external

field induces particle motion, which is tied to the fluid flow by hydrodynamic viscous effect, and, in turn, the particle displacement will subsequently alter the local distributions of the external field and the flow field, so on and so forth. Meanwhile, the particles interact both hydrodynamically and magnetically/electrically when they move to close proximity of each other. To fully resolve the multiphysics-driven particle dynamics, a commercial finite element-based modeling program, COMSOL Multiphysics®, is adopted in this dissertation for the numerical computation. Specifically, two types of particle-field-flow interactions, dielectrophoresis (DEP) and magnetophoresis (MAP) have been investigated, which constitute the primary means of particle manipulation in fundamental research in biomedicine and biomedical engineering. The arbitrary Lagrangian-Eulerian (ALE) method is used to update the spatial location of the moving particles and to monitor the instantaneous field distributions, since it allows the computational mesh inside the domains to move arbitrary to optimize the shapes of elements while the mesh on the boundaries and interfaces of the domain can move along materials to precisely track the boundaries and interfaces of a multi-material system. The basic solution strategy follows:

1) Based on the initial particle and field distributions, the Maxwell stress tensor approach is applied to calculate the field-induced driving forces and torques on the particles, which is chosen to accurately handle particle of irregular shape and external fields with strong non-uniformity. Together with the Cauchy stress tensor, the forces and torques exerted on the particle due to both the external field and the hydrodynamic field can be completely determined.
2) Once the driving forces and torques are computed, the motion of particles

(including both translation and rotation) is computed in the fluid domain simultaneously with the flow field. The equations of motion of the fluid and particles are coupled through the no-slip condition at the particle boundaries.

3) A moving mesh scheme is used to solve the particle-fluid-field interaction where flow field and the external electric/magnetic field are closely coupled. The instantaneous field distribution was obtained by considering the spatial location of particles.

The multiphysics simulation framework developed in this dissertation provides much more flexibility in extracting useful information for cellular alignment and patterning that is otherwise inaccessible to cell line culture study and animal experiment. It also enables a powerful tool to design and optimize particle manipulation techniques based on DEP and MAP which will benefit the research community beyond SCI repairing and tissue engineering.

This dissertation is organized as following. Chapter 2 and Chapter 3 present the experimental study of magnetically driven alignment of injectable NSC scaffold for axonal regeneration. In particular, Chapter 2 discusses the synthesis and characterization of SPIONs assemblies as well as the cytotoxicity study. Chapter 3 offers the details of the magnetic manipulation and directed assembly of SPIONs-labeled cells into two-dimensional (2D) and three-dimensional (3D) structures. The numerical modeling efforts are deliberated in Chapters 4 to 8. Chapter 4 introduces the application background of particle manipulation and the basic concepts and theories of DEP and MAP. Especially, the two primary theoretical methods, i.e., the effective dipole moment approach and the Maxwell stress tensor approach, are reviewed which

can be applied to calculate the field induced forces and torques on particles. Chapter 5 summarizes the key elements of the numerical model, including the multiphysics modules, the governing equations, the numerical methods and the solution procedures. Chapter 6 explores the mechanism and process of DEP directed pearl chaining under an uniform electric field. DEP directed particle assembly, especially the interparticle interactions and the particle trajectory during the assembly process is investigated with identical particles. Considering the effect of electrical properties on DEP interactions, Chapter 7 investigates the DEP-induced pattern formation of dissimilar particles with a focus on the difference in the particle-field-fluid interactions from that of identical particles. Chapter 8 is focused on numerical study of particle motion under MAP. Finally, the conclusion of the present work and suggest directions for future work are summarized in Chapter 9.

Chapter 2. Preliminary Study of NSC Scaffold

As a primary nervous system disorder, spinal cord injury (SCI) causes severe and chronic debilitation or even permanent disability to millions of people in the US and worldwide. SCI affects the young people (aged from 16 to 30), mainly due to motor vehicle accidents or battlefield injuries, as well as senior citizens (aged 70 and above) due to aging-related stenosis or bone quality change. A person suffering from SCI may incur between $500,000 and $3.1 million in life time medical expenses. The economic costs for SCI are well beyond $10 billion per year in the US alone [9]. Besides the heavy familial, social and economic burden, the patients' physical and emotional suffering is immense. Despite the extensive research efforts and improvement in the rehabilitation approaches, unfortunately, SCI continues to be a significant cause of disability and mortality.

Effective treatments are currently not available for the spinal cord injury (SCI)-triggered sensory and motor impairments, primarily due to the lack of successful strategies being optimally developed to promote long distance axonal regeneration. Unfortunately, most axons in the adult mammalian central nervous system (CNS) fail to regenerate after injury. This has been attributed not only to the intrinsic indolence of the mature neurons, but also to the non-permissive environment encountered by the injured axons. Therefore, novel therapeutic approaches to modify the inhibitory environment to promote axonal regeneration are urgently needed. Neural stem cells (NSCs) have shown great promise to promote axonal regeneration and functional recovery after SCI, likely an effective novel therapy.

The research conducted in this dissertation aims at developing a novel technique to fabricate injectable, alignable, and bioactive scaffolds for axonal regeneration after SCI that use NSCs as the building blocks. This work capitalizes on the ability to manipulate superparamagnetic iron oxide nanoparticles (SPIONs) with magnetic field remotely and noninvasively. In this approach, the NSCs are labeled with nanoengineered cationic magnetoliposomes (CMLs) which encapsulate numerous SPIONs, and can be injected into the injured spinal cord in colloidal suspensions. Upon the application of a magnetic field, magnetically labeled NSCs will spontaneously self-assemble into chain/column lattices and align along a virtual axis defined by the field flux lines, thereby forming a scaffold to guide the directional regrowth of axons.

2.1 Background

2.1.1 NSCs and Biological Scaffolds

SCI is difficult to heal partially because the central nervous system (CNS) has very limited capacity to repair itself after an injury. Mature CNS neurons have an intrinsic indolence to regenerate. Previous experiments [10] showed that severed axons initially attempted to regenerate spontaneously, but quickly lost the ability to do so after failing to find their way in the right direction to re-establish the nerve connection. Additionally, the non-permissive environment encountered by the injured axons, which includes the molecules in myelin (the insulating sheath surrounding nerve fibers) carrying inhibitory factors and the scar that form after the injury, contributes to their inability to regenerate [11].

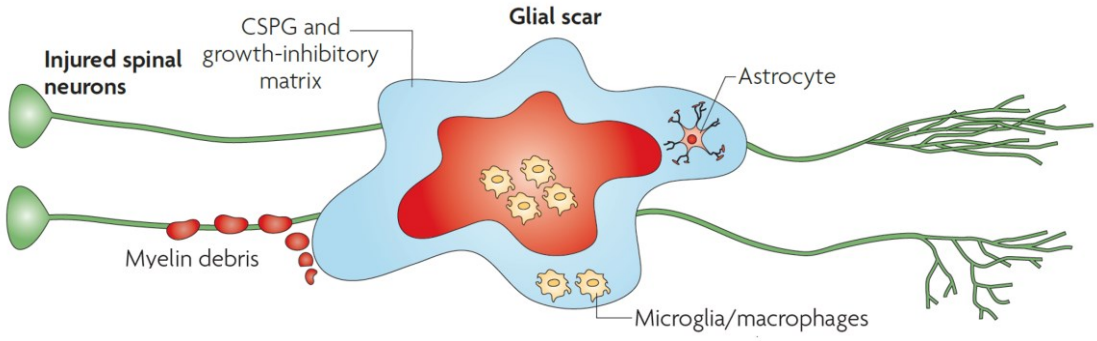

Figure 1 Schematic of injured spinal neurons with Glial scar and myelin debris [11].

Accordingly, several repair strategies have been explored to promote axonal regeneration in the injured spinal cord, those including: 1) enhancing the intrinsic regenerative capacity of injured neurons [12-14]; 2) providing permissive neurotrophic factors [15,16]; 3) transplantation of regeneration-permissive cells, such as Schwann cells, olfactory ensheathing glia or NSCs; and 4) removing the inhibitory factors in the injured spinal cord. Since the mechanism of action for each of these strategies is distinct, one would expect that combining multiple strategies would bring about greater axonal regeneration. The NSC-based cell therapy represents such a promising approach. Grafted NSCs and glial precursor cells (GPCs) have shown great potential to promote axonal regeneration after SCI. They can replace the lost neurons and oligodendrocytes to promote the remyelination of demyelinated and degenerated axons. NSCs also constitutively secrete neurotrophic factors and other permissive substances to stimulate axonal growth across an injury gap [17,18]. After transplantation into the transected spinal cord, the NSCs promote regeneration of the corticospinal tract across the injury site to reach the caudal spinal cord where the regenerating axons reform synapses.

However, a grand challenge exists for the above NSC-based cell therapy, especially in chronic SCI: when the entire cross section of the spinal cord is replaced with scar tissue and/or fluid-filled cysts, the mechanical substrates that provide mechanical support for axonal regeneration and the three-dimensional cytoarchitectural information become permanently lost [19]. Fortunately, biological scaffolds seeded with NSCs can provide a solution, which not only offer structural support for the attachment of grafted NSCs in the injury site but also sustain a controlled biochemical microenvironment to induce the differentiation of NSCs to desired cell lineages. Current scaffolds for SCI are mostly made of polymer composites that are assembled in the form of porous biomatrix or guidance microconduits, as shown in Figure 2 [19-22]. While the bioscaffolds for SCI repair show promising attributes, such as mechanical compliance, biocompatibility and degradation, high porosity and functionalization with bioactive motifs, almost all of them have to be fabricated in vitro and then implanted into the injured spinal cord through invasive surgical operations.

An ideal scaffold for SCI repair is envisioned in the proposed research, which possesses the following attributes: (1) Injectability: the constituent materials of the scaffold can be directly injected as aqueous suspensions into the injured spinal cord, and afterward the scaffold will establish itself spontaneously in vivo; (2) Alignability: the formed scaffold will be aligned along a preferential direction, i.e., longitudinally in the spinal cord, to guide the regrowth of axons to bridge the injury gap; and (3) Bioactivity: growth factors can be accommodated in the scaffold and be released in a controlled way to promote the survival of grafted NSCs and the axonal regeneration. Currently, there are no technologies capable of fabricating scaffolds with those attributes.

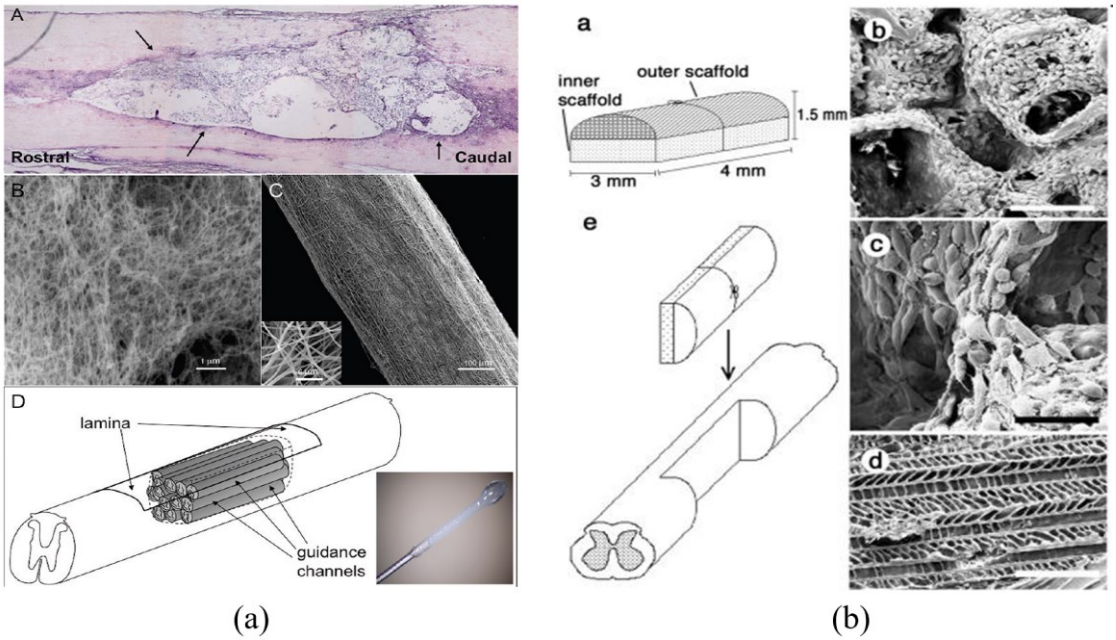

Figure 2 Current scaffolds fabricated for SCI repair [19,21].

2.1.2 Magnetic Nanoparticles and Field-directed Assembly

Superparamagnetic iron oxide nanoparticles (SPIONs) with a diameter less than 20 nm exhibit strong magnetization only when they are exposed to an external magnetic field, otherwise they show no remnant magnetism [23]. SPIONs have several attributes for biomedical applications. If cells are labeled with SPIONs, the coupling between the magnetic field and SPIONs allows remote detection of the cellular components in a body, regardless of whether there are intervening structures [24]. SPIONs can also be surface-functionalized with specific biomolecules. Furthermore, SPIONs can form very stable colloidal suspensions. As a result, SPIONs have been used as effective imaging tracer tags and drug delivery vehicles, including the magnetic drug targeting (MDT),

magnetofection and gene delivery (MF), magnetic resonance imaging (MRI) and magnetic fluid hyperthermia (MFH) [25-29].

More recently, SPIONs have been used for cellular mechanical conditioning and scaffold fabrication in tissue engineering. In the first type of application, SPIONs attached to the integrin receptors on the cell surface can induce precisely controlled magnetic forces to target and activate individual mechanosensitive ion channels [30-32]. The second type of application hinges upon the fact that when guided by an external magnetic field, SPIONs can self-assemble into one-, two- or three-dimensional ordered supraparticle structures [33,34]. In Figure 3 , magnetic forces were used to position thrombin-coated microparticles in two-dimensional hexagonal arrays which direct the self-assembly of fibrin fibrils [35]. Fibrin matrices with defined nanoscale architecture were fabricated that support adhesion and spreading of human endothelial cells. In this dissertation, the ability to remotely control SPION-labeled neural stem cells will be harnessed to assemble chain/column lattices as scaffolds for guiding directional regeneration of axons.

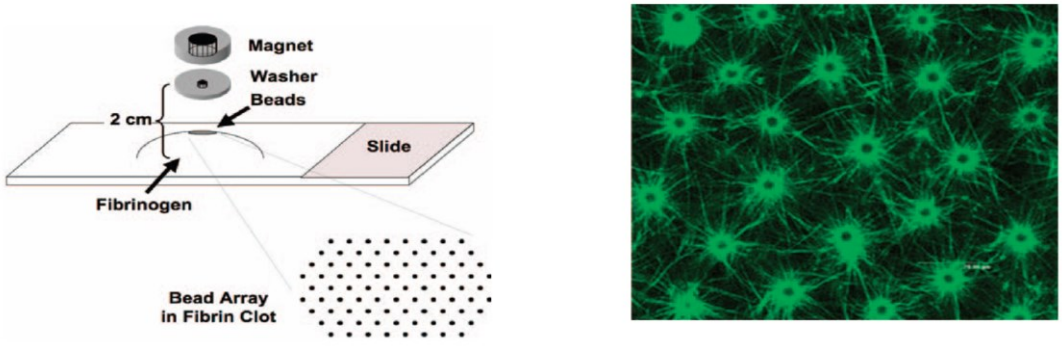

Figure 3 Magnetic field directed self-assembly of cells in 2d fibrin gel scaffold created with a magnetically oriented particle array [35].

2.1.3 Magnetoliposomes

Superparamagnetic iron oxide nanoparticles (SPIONs) are widely used as the force carriers in the magnetically-directly cell manipulation study. However, SPIONs in their native unmodified form are inefficient intracellular labels for stem cells and other mammalian cells [36-38] and they must be surface-modified to improve biocompatibility and to increase functionality. Usually, SPIONs can be coated with synthetic or organic polymers (such as dextrans or proteins) and amphiphilic molecules (such as fatty acids or phospholipids) [39]. When a group of clustered SPIONs is encapsulated in the interior of a bilayer of amphiphilic phospholipids, magnetoliposomes (MLs) are formed [40,41] as schematically shown in Figure 4.

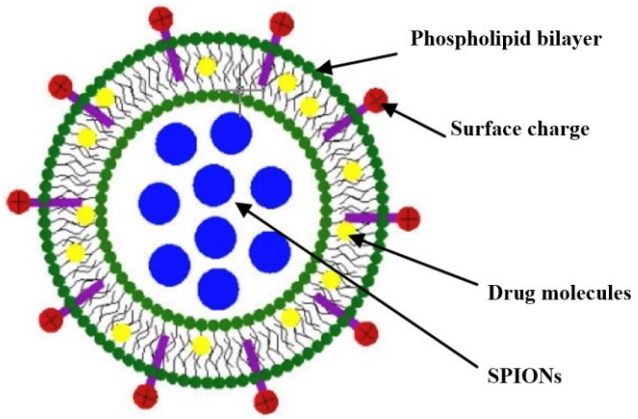

Figure 4 Schematic of magnetoliposome (ML) that can function as combined magnetic labeling and drug delivery agents.

When a magnetic field is applied, the magnetic dipole moments of individual SPIONs inside a ML superimpose and synergistically enhance the cumulative dipole moment of the ML, thus making the MLs highly efficient for MRI tracking and magnetic-force-based manipulation. Since the phospholipids are natural substances,

MLs have excellent biocompatibility. When the MLs are internalized by cells, the SPIONs will be shielded from degradation by strongly chemisorbed phospholipid layer and can persist during continuous cell proliferation. Other benefit of the MLs come from the wide variety of phospholipids that can be used to synthesize them and the ease with which their surfaces can be modified chemically by specific targeting ligands. These will great increase the cellular uptake efficiency as well as reduce cytotoxicity of the MLs. More importantly, hydrophilic and hydrophobic drugs can be hosted either within the lipid bilayer or in the inner aqueous cavity of the MLs, which makes the MLs good drug delivery carriers [39]. Release of the drugs can be triggered and controlled by increasing the local temperature (below the limit of hyperthermia) via heating the nanoparticles with radio frequency (RF) electromagnetic fields [42].

Since cellular membranes bear an overall negative charge, positively charged MLs can be easily internalized by the cell via electrostatic interaction. Thus, cationic MLs (CMLs) with superior properties are desired for effective cellular uptake and drug delivery.

2.2 Research Rationale

The underlying rationale of this dissertation research is illustrated in Figure 5. Cationic magnetoliposomes (CMLs) will first be synthesized with SPIONs encapsulated in the core and neurotrophic growth factors hosted within the lipid bilayer. The CMLs are used to magnetically label the NSCs. After cellular internalization, an external magnetic field will be applied to induce the cumulative dipole moment in the CML-labeled NSCs. The consequent magnetic interactions between NSCs cause spontaneous

formation of highly aligned chain/column lattices. The principal axis of the lattices will conform to the magnetic flux lines, serving as a virtual guide to the NSC proliferation and colonization. Sustained release of the neurotrophic growth factors stored in the CMLs will be triggered and controlled by a RF electromagnetic field. If desired, MRI can be used to noninvasively track various cellular events using the SPION core as contrast agents. In the foregoing procedures, synthesis of CMLs and magnetic labeling of NSCs will be conducted in vitro. Aqueous suspension of the CML-labeled NSCs can be injected directly into the injured spinal cord. Aligned NSC chain/column lattices will be spontaneously self-assembled in vivo when the magnetic field is applied. Thus all three critical requirements of an ideal scaffold for spinal cord nerve repair, i.e., injectability, alignability and bioactivity, can be satisfied. In this chapter, the synthesis of SPIONs and CMLs and the study of their cytotoxicity will be firstly discussed.

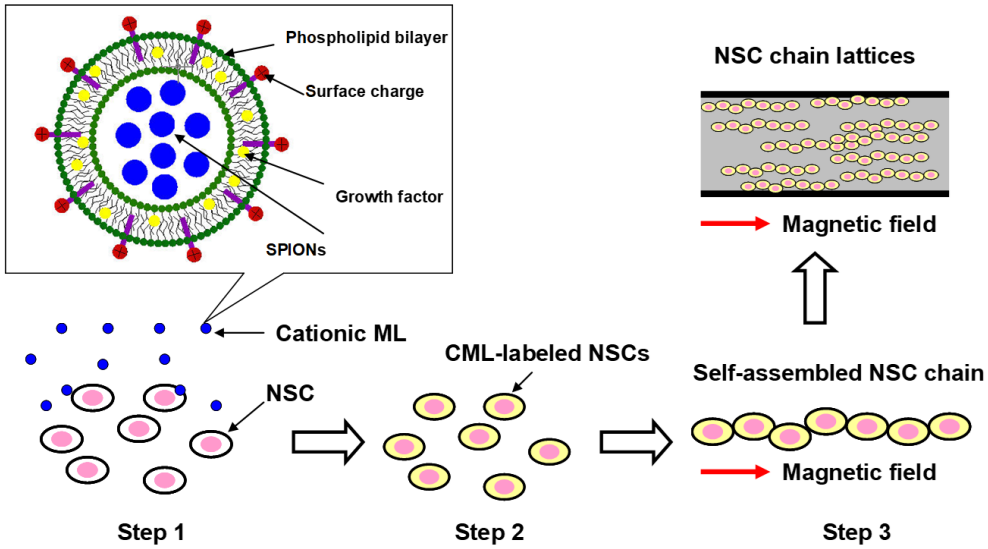

Figure 5 Magnetically directed self-assembly of NSC chain lattices labeled with CMLs.

2.3 SPION Synthesis

SPIONs, as the building blocks of MLs, are synthesized in-house via a co-

precipitation process where iron oxides are formed from aqueous Fe^{2+}/Fe^{3+} salt solutions by the addition of a base under inert atmosphere at room temperature as shown in Figure 6(a). The size and composition of SPIONs are controlled by the type of salts used (e.g. chlorides, sulfates, nitrates), the Fe^{2+}/Fe^{3+} ratio, the reaction temperature, the solution pH value and the ionic strength of the media. The size, composition and microstructure of the SPIONs have been characterized by X-ray diffraction (XRD) and transmission electron microscopy (TEM), as shown in Figure 6(b). Magnetic properties including the size dependent superparamagnetism and inter-particle interactions have been investigated using magnetic hysteresis and temperature-dependent field cool and zero-field magnetization measurements, as shown in Figure 6(c).

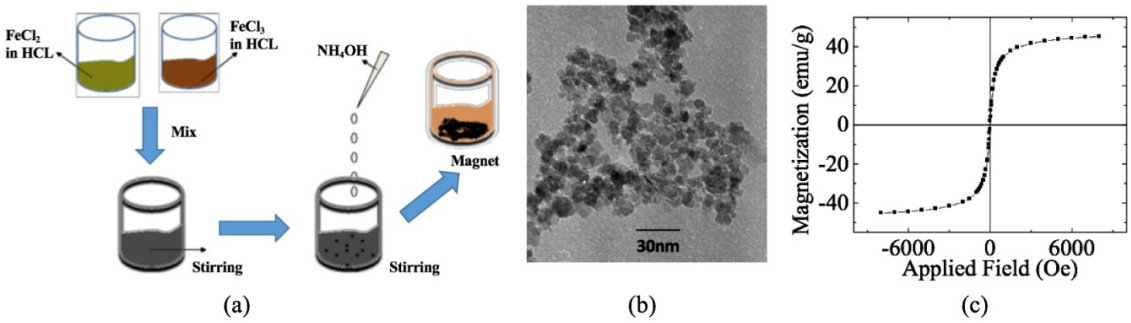

Figure 6 Electrochemical synthesis of SPIONs: a) Schematic of Fe3O4 SPION synthesis process, b) TEM micrograph of SPIONs, and c) room temperature superparamagnetic response of SPIONs.

2.4 CML Synthesis

Since phospholipids in aqueous environments tend to self-assemble to form closed bilayer structure [43], liposome is presented to describe the colloidal, vesicular structure consisted of one or multiple phospholipid bilayers membranes. As shown in

Figure 7, Phospholipid bilayer membrane is a two-monolayer lipid structure, where each lipid is composed of oil-soluble hydrocarbon hydrophobic tail and water-soluble hydrophilic head.

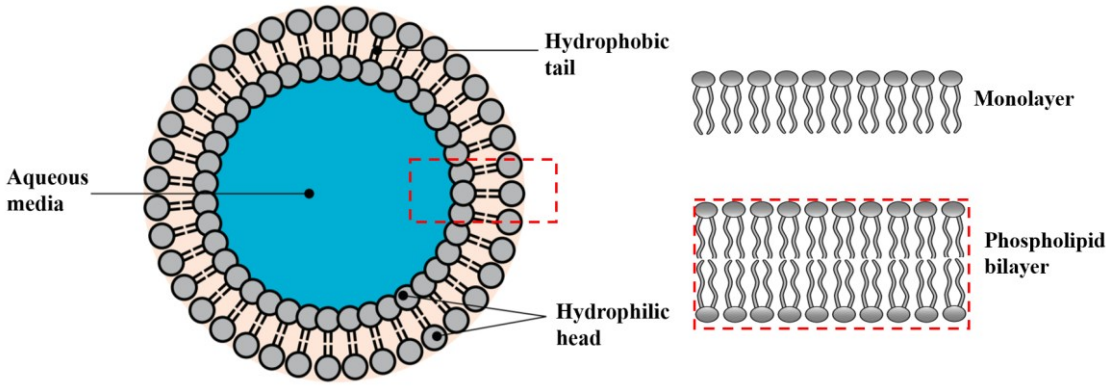

Figure 7 Schematic liposome structure [44].

The proper use of liposomes requires fine control of the lipid composition, size distribution, unilamellarity, encapsulation efficiency (EE) and biocompatibility [45]. A variety of biocompatible lipids, such as egg phosphatidylcholine (EPC), Dimyristoylphosphatidylcholine (DMPC), Dilauroylphosphatidylcholine (DLPC) and dioleoylphosphatidylethanolamine (DOPE), can be used to formulate liposomes with precisely tailored chemical, biological and mechanical properties. Three additional factors must be considered when choosing lipids for CML synthesis: the charge of lipids, the degree of saturation and the length of acyl chain [46]. Generally, lipids with longer, saturated chain is preferred since it presents lower permeability which will increase the stability. Also, during the liposome synthesis process, the temperature should be kept above the phase transition temperature. Based on these considerations, DOPE and DMPC were selected for the synthesis of CMLs in this work due to their

electronegativity, long and saturated chain and low phase transition temperature.

According to the lamellarity (number of bilayers) and size, liposomes can be generally classified into small unilamellar vesicles (SUVs), large unilamellar vesicles (LUVs), multilamellar vesicles (MLVs) and multivesicular vesicle (MVV), as showed in Figure 8. Considering to maximize the SPIONs encapsulation in CMLs, size and homogeneity of the liposome play more crucial role compared to the lamellarity of liposome. Therefore, LUVs with relatively large internal volume are preferred in this work.

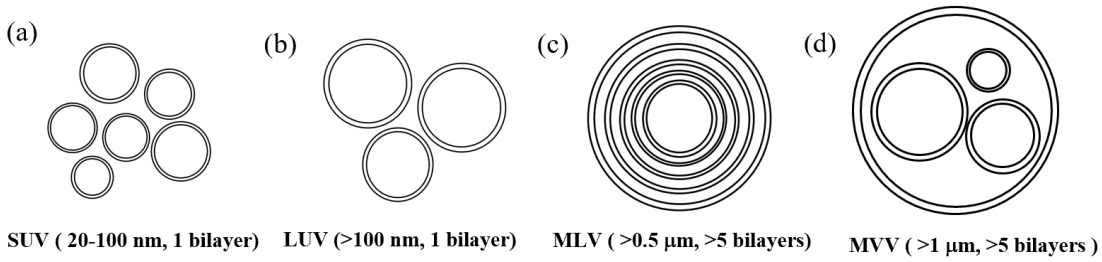

Figure 8 Type of liposomes according to lamellarity and size, (a) SUV, (b) LUV, (c) MLV, (d) MVV.

Liposomes can be produced using several methods, such as reverse-phase evaporation, injection, electroformtion, thin-film hydration, heating method etc., as detailed in Table 1. Although some methods, like thin-film hydration (Bangham method) are well systematically studied, considering the type of synthesized liposome and the accessibility, reverse-phase evaporation which enables sufficient inner volume to entrap aqueous solutions (SPIONs in this work) was first investigated.

Table 1 Conventional Methods of Liposome Production

Methods	Advantages/Disadvantage	Liposome Type	REF
Reverse-phase evaporation	Pros: Suitable EE, Simple process Cons: Time consuming, Sterilization issue	LUVs, MLVs	[47]
Ethanol/ether injection	Pros: Simple process Cons: Organic solvent residue	SUVs SMVs	[48]
Electroformation	Pros: Homogeneous size distribution Con: High cost	GUVs	[49]
Thin-film hydration	Pros: Simple process Cons: Low EE, Organic solvent residue	MLVs	[50]
Heating method	Pros: Simple design, Organic solvent free Cons: High temperature	SUVs, MLVs	[51]
SMVs-small multilamellar vesicles, GUVs- giant unilamellar vesicles (>1 μm)			

2.4.1 Reverse-phase Evaporation Method

The reverse-phase evaporation method was first employed in an effort to identify a suitable liposomal synthesis route. The procedures are shown schematically in Figure 9 (a). In order to form the lipid films, the required amount of lipid 1,2-dimyristoyl-sn-glycero-3-phosphorylcholine (DMPC), and dimyristoylphosphatidylcholine (DMTAP) with desired ratio 1:1 was dissolved in organic solvent chloroform (CHCl3). With in-house synthesized SPION solution mixed with lipid solvent, the solution was sonicated to ensure homogeneous distribution. Then, either rotary evaporation or freeze drying can be applied to remove the solvent. If the volume is small (<1mL), the solvent can be evaporated under a dry nitrogen or argon stream in a fume hood. For larger volumes, the organic solvent should be removed by rotary evaporation which will yield thin lipid film on the side of a round bottom flask [46]. In this work, excess solvent was removed

from the lipid solution by evaporation at 37°C in a rotary evaporator to produce a thin lipid film on the container wall surface. Subsequently, the lipid film was thoroughly dried to remove residual organic solvent by placing the flask on a vacuum pump overnight. Afterwards, the bilayer-structured CMLs were formed by hydrating the lipid film with aqueous phosphate-buffered saline (PBS) solution, followed by ultrasonication. To further fine-tune the size of CMLs, the PBS solution was filtrated multiple times through carbonate membranes with nanopores (220 and 450 nm). The micrograph in Figure 9 (b) shows the reverse evaporation method produces fairly uniform CMLs with diameters of generally less than 500 nm.

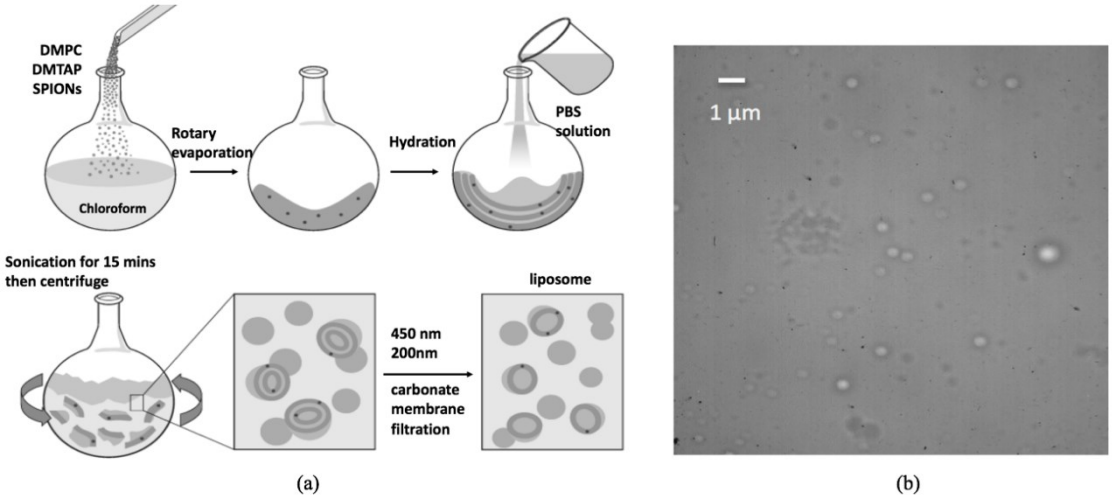

Figure 9 (a) Procedures of CMLS synthesis in reverse-phase evaporation method, (b) Micrograph of CMLs produced.

With the reverse-phase evaporation method, liposome vesicles with desired properties is able to achieve, high encapsulation efficiency, high aqueous space-to lipid ratio and widely variable chemistry of lipid components [52]. However, the major deficiency of reverse-phase evaporation is that both lipids and encapsulation compounds have to homogeneously distributed in the same solvent before drying to

lipid film. Although in this work, SPIONs solution is compatible with the organic solvent used, it is limiting the utility for encapsulating drug molecules or other active agents for further applications.

2.4.2 Inverted Emulsion Method

Considering the limitation of reverse-phase evaporation method, inverted emulsion method was then studied which allows two monolayers of phospholipid bilayer membrane to be assembled independently [53].

The CML synthesis route using the inverted emulsion method is shown schematically in Figure 10, which involve the assembly of two independently formed monolayers of lipid. The detailed procedures for one sample preparation are as follows. First, dissolved lipids, where 2 mg 1,2-dioleoyl-sn-glycero-3-phosphoethanolamine (DOPE) dissolved in 2 mL dodecane, are combined in a glass flask and sonicated for 30 minutes to ensure even distribution in the solvent. The aqueous SPION solution with PBS is emulsified by mixing with half of solvent of the dodecane oil containing dissolved DOPE. As tiny droplets of SPION solution are formed, the DOPE molecules dispersed in the oil phase adsorb onto the droplet surface to form a lipid monolayer, which will serve as the inner leaflet of the final bilayer structure. The size of the surface-covered emulsion droplets determines the size of CMLs, which can be fine-tuned by ultrasonication and filtration through carbonate membrane with nanoscale pores. In this work, the mixture in Tube A is through a liposome extruder at 35°C using carbonate membranes of 450 nm and then 200 nm pore sizes, respectively, twice for each membrane. Subsequently, PBS solution, half of solvent of the dodecane oil containing

dissolved DOPE in Tube B, and filtrated mixture in Tube A are added to Tube C one after another. After centrifugation at 1000 rpm for 10 minutes, a second layer of lipid is picked up on the surface, thus forming the bilayered CMLs. The micrograph in Figure 11 shows the CMLs produced by the invert emulsion method with diameters usually less than 500 nm and with uniform size distribution. Thus, inverted emulsion method is adopted for synthesizing the CMLs in this work.

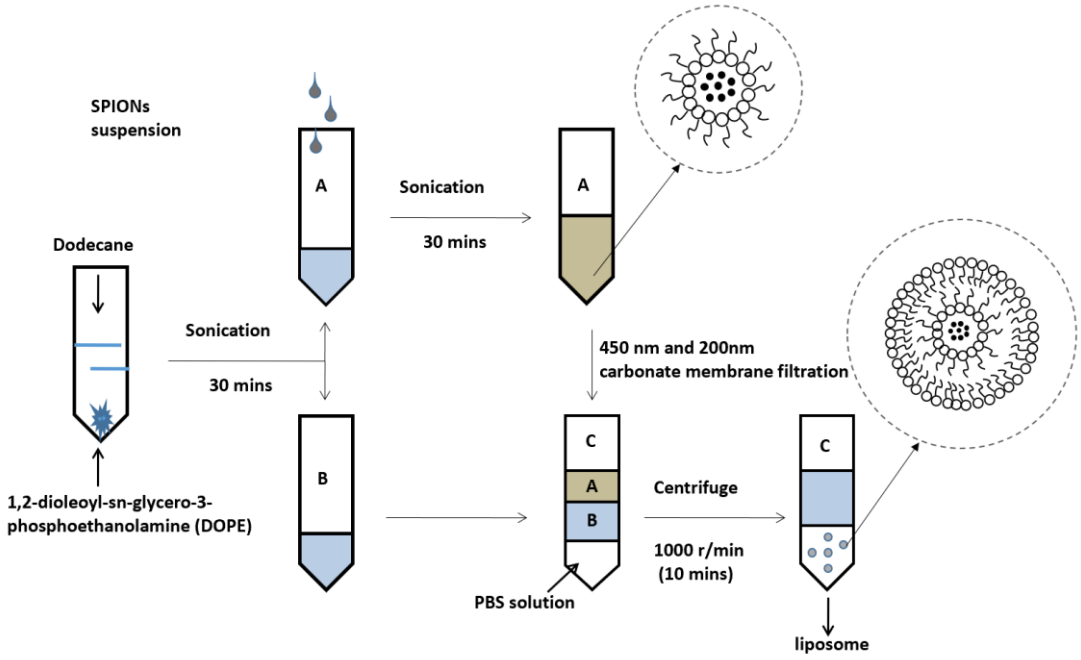

Figure 10 Procedures of CMLS synthesis in inverted emulsion method (lipids indicated by lollipop structures).

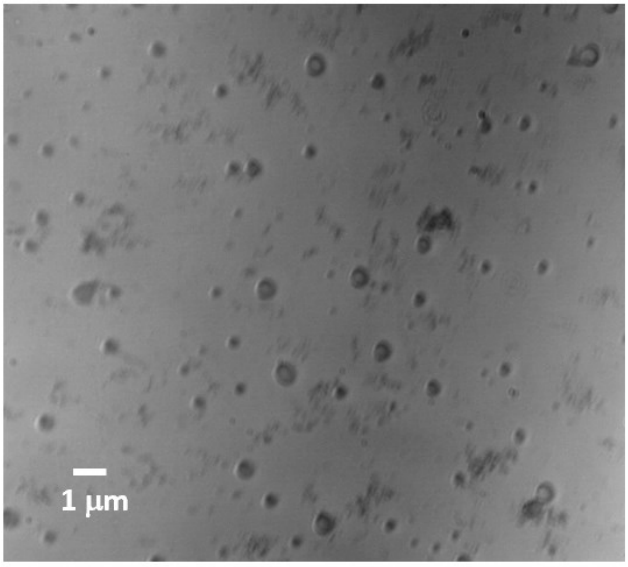

Figure 11 Micrograph of CMLs produced from inverted emulsion.

2.5 Magnetic Nanoparticle Assembly

At the later stage of the experimental investigation of this dissertation, a biocompatible commercial magnetic nanoparticle assembly, NanoShuttle™, a product of Nano3D Biosciences, became available, which has been marketed as being highly effective in meeting the requirements for magnetic cellular manipulation. To increase functionality of magnetic nanoparticles, instead of coated with amphiphilic molecules as MCLs, NanoShuttle is obtained by assembling gold (Au), magnetic iron oxide and poly-L-lysine as shown in Figure 12 [54]. With the gold-phage in NanoShuttle, it can present as signal reporter for fluorescence and dark-field microscopy due to the gold (Au) optical properties [55], which optimizes the optical property of the magnetic nanoparticle assembly.

When cells incubated with NanoShuttle, cells are magnetized by poly-L-Lysine feature which facilitates nonspecific attachment of nanoparticles to the cell membranes

via electrostatic interaction. Once particles attached to the membrane of cells, the magnetic nanoparticles remain for 7-8 days before releasing into cell extracellular matrix. If the nanoparticle is internalized, it will exit the cell but still attached to the cell membrane [56]. With this unique feature of NanoShuttle, it is able to provide a sustainable magnetic force which is crucial in the bioscaffold self-assembly, especially for three-dimensional (3D) structure which requires long distance axonal regeneration. Therefore, at the later stage of the experimental investigation, NanoShuttle is utilized in magnetic cellular manipulation, mainly in the 3D cell self-assembly process.

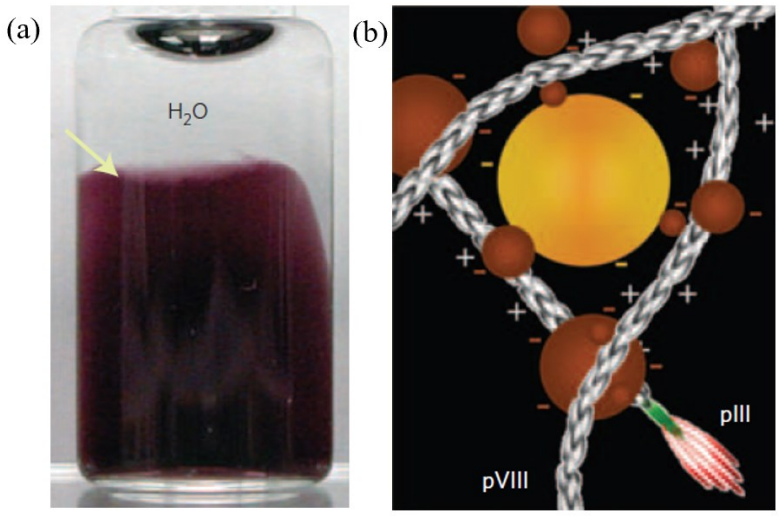

Figure 12 (a) Vial of magnetic iron oxide-containing hydrogel (arrow) in water, (b) Scheme of electrostatic interactions of magnetic iron oxide (brown spheres) and gold (yellow spheres) nanoparticles with phage (elongated structures; PIII and PVIII indicate surface capsid proteins). Nanoparticles are not drawn to scale [54].

2.6 Biocompatibility Study

Biocompatibility is defined as the ability of a material to perform its desired function without causing any local or systemic adverse response in the recipient of the material [57], and it plays a vital role in evaluating the potentials of magnetic

nanoparticle assemblies in vivo applications. The primary indicator of the biocompatibility of a given material is the cytotoxicity, also known as the cell viability, which is the quality of being toxic to cells [58]. As the commercial magnetic carriers, NanoShuttle is biocompatible where iron oxide and phage are recognized as safe by the FDA, and gold nanoparticles are in clinical trials for therapeutic use with no indications for systemic toxicity [59]. Systematic cytotoxicity study has been performed with several cell lines, such as Pulmonary fibroblast (PFs), smooth muscle cells (SMCs), epithelial cells (EpiCs), pulmonary endothelial cells (PECs) and 3T3-L1 which present that NanoShuttle^{TM} has no effect on the cell proliferation, and viability [60-62]. Hence, in this section, the cytotoxicities of the CMLs synthesized in house is evaluated to ensure their suitability in the subsequent study of magnetic manipulation of cells.

2.6.1 Cytotoxicity Study of SPIONs

Cytotoxicity of the SPIONs, the building blocks of CMLs, was first investigated by using Rat-2 fibroblast cells as the model system. The Rat-2 fibroblast cell line offers fast doubling time and relative ease of maintenance and has been used to assess the toxicological response of several biomolecular systems, such as polypropene mesh, fibrinogen, and zirconia [63-65]. The cytotoxicity was studied using a Trypan blue staining assay. Trypan blue is an azo dye that is cell membrane impermeable and only enters cells with compromised membranes. Upon entry into the cell, trypan blue binds to intracellular proteins rendering the cells a blue color. The trypan blue staining assay allows for a direct identification and enumeration of live (unstained) and dead (blue) cells in a given population. In this assay, a cell suspension is simply mixed with trypan

blue and then visually examined to determine whether cells take up or exclude the dye. In the cytotoxicity study, the Rat-2 fibroblast cells were cultured with bare SPIONs, SPIONs coated with $N(CH_3)_4OH$ (tetramethyl-ammonium hydroxide for better dispersion) and SPIONs coated with dextran (a hydrophilic polysaccharide composed of α-1,6-linked d-glucopyranose which has been widely used for sustained protein and drug delivery in tissue-engineered scaffolds), respectively. After 24-hour exposure, three samples were treated with Trypan blue staining assay as indicated in Figure 13 and demonstrate different biocompatibility results, as showed in Figure 14, where the non-viable cells are represented as the dark color. Figure 14(a) indicates N(CH3)4OH-coated SPIONs destroy all trace of cell activity and membrane structure. Figure 14(b) shows that the viability of Rat-2 fibroblast cells is reduced to less than 20%. Figure 14(c) shows that confluent cell structure with dextran-coated SPIONs is maintained and viability is greater than 90%, comparable to the control experiment without nanoparticles added.

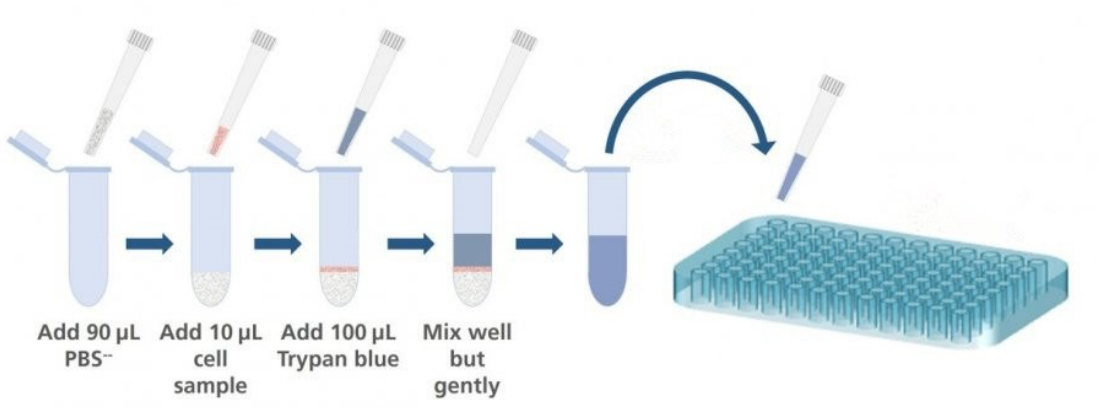

Figure 13 The routine process of Trypan Blue Staining Assay [66].

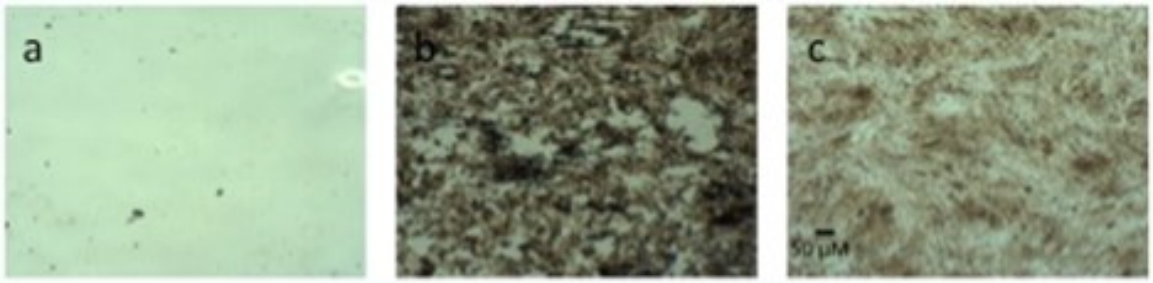

Figure 14 Optical micrographs of a confluent culture of Rat-2 fibroblast cells after 24-hour exposure to: a) N(CH3)4OH-coated SPIONs; b) bare SPIONs; and c) dextran-coated SPIONs

2.6.2 Cytotoxicity Study of CMLs

The 3-(4,5-dimethylthiazol-2-yl)-5-(3-carboxymethoxyphenyl)-2-(4-sulfophenyl)-2H-tetrazolium (MTS) assay was used to study the viability of Rat-2 fibroblast cell line co-cultured with CMLs. This assay is a colorimetric technique for quantification of viable cell in proliferation or chemosensitivity assays [67]. With the NAD(P)H-dependent dehydrogenase enzymes in metabolically active cells, the MTS tetrazolium compound is reduced and produces a colored formazan dye in the presence of phenazine methosulfate (PMS) which is soluble in cell culture medium and has an absorbance maximum at 490-500 nm in PBS. Thus, the cell viability is presented by the quantity of formazan product that is proportional to the quantity of living cells in culture. The MTS assay is a "one-step" MTT assay and offers the convenience of adding reagents directly to the cell culture without the intermittent steps required by the MTT assay.

In the experiment, fibroblast cells at two initial cellular concentrations, low (125,500 per mL) and high (223,000 per mL), were used. The CMLs concentration was varied for each cell concentration, i.e., 2.5 mg/mL, 1.5 mg/mL, 0.5 mg/mL and 0 mg/mL. After adding 20µL/well of MST assay solution, the sample was incubated for 1 hours at

37℃ in humidified, 5%CO_2 atmosphere. Then, the absorbance was measured and recorded at 490 nm. The measured MTS signals for both two were invariant over time. Therefore, the time-dependent trend of MTS data observed in the viability study was solely due to cellular events.

The MTS measurement data were recorded every 0.5 incubation hour in a 4.5-hour span. The results are shown in Figure 15, where the slope of the data represents the cellular decease rate. The results demonstrate that the viability of CML-labeled cells at all CMLs concentrations (0.5, 1.5 and 2.5 mg/mL) is almost identical. Thus, the conclusion can be drawn that the cellular viability is not affected by the CMLs.

.

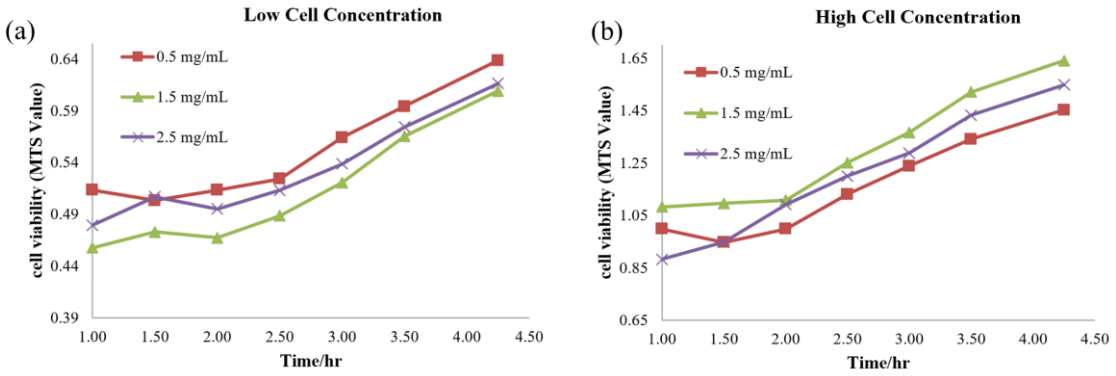

Figure 15 Cell viability at different CML concentrations using MTS assay for (a) a low initial cell concentration, 125,500 per mL and (b) a high initial cell concentration, 223,000 per mL

Chapter 3. Magnetic Manipulation and Directed Assembly of SPIONs-Labeled Cells

The efficiency of neural stem cell (NSC)-based therapy for spinal cord injury (SCI) repair depends critically on how well the regenerating NSCs can orient themselves along a preferential direction (i.e., longitudinally in the spinal cord) to re-establish the nerve connection. This research attempts to utilize the spontaneous self-assembly of magnetically-labeled NSCs into aligned chain/column lattices to restore the directional information lost in SCI. Hence, following the cytotoxicity study, in vitro experiments were conducted to demonstrate magnetic assembly and manipulation of various cell lines.

3.1 Two-dimensional Magnetic Manipulation

3.1.1 3T3 Fibroblast Cell Line

Magnetic manipulation of SPIONs-labeled cells was first investigated by using 3T3 fibroblast as the model system to quantify the effect of CML concentration on the magnetic alignment of cells. The 3T3 fibroblast cell line, which is originally from the primary mouse embryonic fibroblast cells, have been widely applied in tissue engineering due to its high growth rate and good stability, especially for some early-stage verification of methodology and procedure [68-70].

Before the experiments, the fibroblast cells were seeded with dilute CML solutions of three different concentrations, 0.2, 0.4 and 1.0 mg/mL, respectively. Then the cells were incubated for 72 hours in standard culture medium at 37 and 5% CO2, both with and without exposure to external magnetic fields. The uniform magnetic field

was created by two neodymium-iron-boron rare-earth magnet bars placed in parallel on a transparent fixture (shown in Figure 16 (a)). The strength of the magnetic field can be controlled by adjusting the distance between the magnet bars. The control group of cells not seeded with CMLs are shown in Figure 16 (b), which appear to grow in random directions after 72-hour incubation. Figure 16 (c) shows similar growth pattern of the fibroblast cells labeled with CMLs (0.2 mg/mL) but without being exposed to the magnetic field, where the darker color in the cells indicate the presence of internalized SPIONs. Figure 16 (d)-(f) depict the magnetic alignment of the CML-labeled cells after being incubated for 72 hours in the magnetic field. It is found that the cells grow along the direction of the magnetic field line, and the degree of alignment improves as the CML concentration increases, e.g., from 0.2 mg/mL in Figure 16 (d) to 1.0 mg/mL in Figure 16 (f).

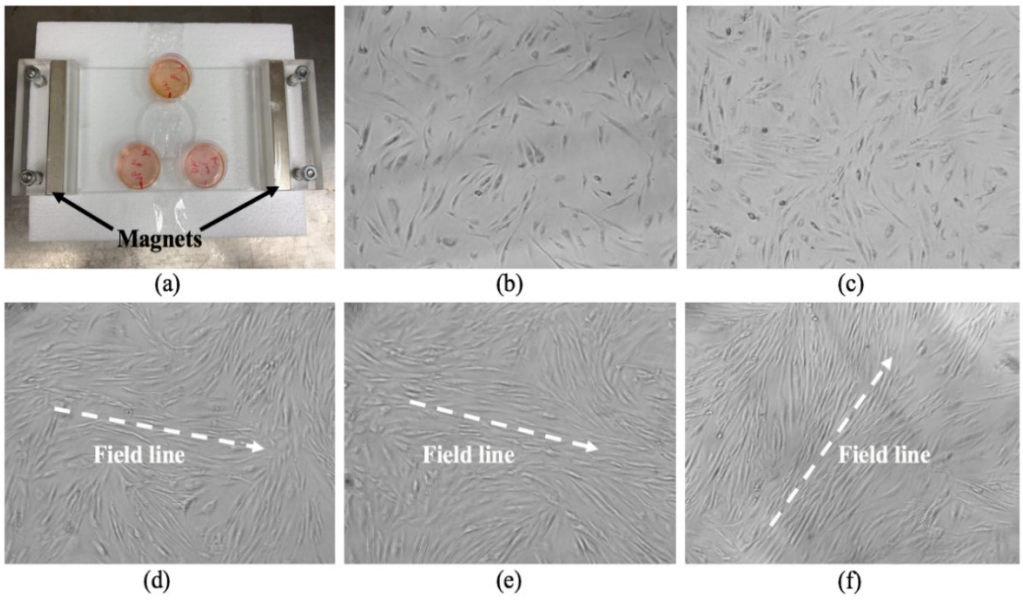

Figure 16 Magnetic alignment of fibroblast cells. (a) Test fixture with adjustable magnetic field strength; (b) fibroblast cells without CML-seeding; (3) CML-seeded cells without exposure to the magnetic field; (d) magnetically aligned cells at 0.2 mg/mL CML concentration; (e) magnetically aligned cells at 0.4 mg/mL CML concentration; and (f) magnetically aligned cells at 1.0 mg/mL CML concentration.

3.1.2 Oligodendrocyte Precursor Cells (OPCs)

As mentioned before, SCI is difficult to heal partially because the central nervous system (CNS) has very limited capacity to repair itself after an injury. Mature CNS neurons have an intrinsic indolence to regenerate. Oligodendrocyte precursor cells (OPCs), which are a subtype of glial cells in the central nervous system, are capable to regenerate oligodendrocytes and differentiate into neurons to promote axonal regeneration [71,72]. Hence, magnetic directed assembly of oligodendrocyte precursor cells (OPCs) labelled with SPIONs was then explored after the prelimentary study of magnetic manipulation of 3T3 cells.

As suggested by the biocompatibility study, the SPIONs are coated with dextran to ensure sufficient cellular viability after uptake. In the experiments, OPCs were seeded with dilute SPION solution and incubated for 24 ~ 48 hours in standard culture medium at 37°C and 5% CO_2. Before the assembly experiment, the cells were washed multiple times with PBS to remove excess SPIONs and were then trypsinized. The glass slide carrying a drop of SPION-labeled OPCs was placed in a magnetic field created by two neodymium-iron-boron rare-earth magnets. The magnetic field strength was measured to be about 200 G. It was found magnetically directed assembly of OPCs occurs almost immediately. The optical microscopy images in Figure 17 show the sequential processes of cellular internalization, harvest and magnetic directed self-assembly.

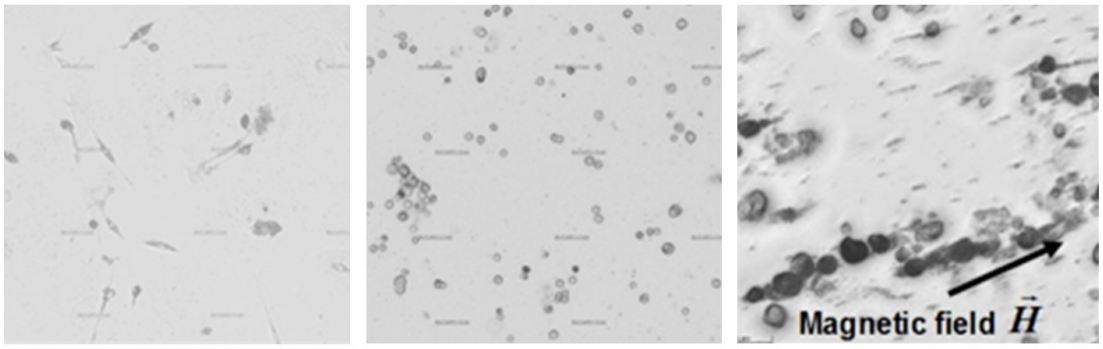

(a) (b) (c)

Figure 17 Microphotographs of OPCs labeled with SPIONs: (a) Cells expanded *in vitro* in a culture flask, note the evidence of intracellular uptake of SPIONs; (b) Cells harvested by using trypsin are still alive after 24 ~ 48 hours exposure to SPIONs; and (c) cell alignment after the magnetic field is applied.

3.2 Three-dimensional Magnetic Manipulation

Although two-dimensional (2D) cell culture has allowed acquisition of early-stage optimization about the methodology and procedure, there is a large gap in the complexity and fidelity between conventional 2D cell culture *in vitro* and tissue environments found *in vivo* [60]. In vitro, cells are attached to planar surfaces as 2D monolayer with rigid substrates which makes cells vulnerable to the morphological and functional change. Gene expression, signaling and morphology in cell growth are found to be different from those *in vivo* [73-77].

To mimic the tissue environments in vivo, three-dimensional (3D) cell culture in vitro systems provides improved tissue-like characteristics with cell-cell-extracellular matrix interaction which is hard to imitate in 2D [78,79]. Hence, to overcome these drawbacks, alternative test platform and procedures were investigated to enable 3D cell culture and magnetic manipulation.

3.2.1 3T3 Fibroblast Cell Line

Considering limitations of 3T3 cell as the monolayer layer with 2D culture, test

platform was revised and constructed to achieve the 3D culture *in vitro*. As illustrated in Figure 18, in addition to a primary magnetic field applied horizontally to control the cell alignment and pattern formation, a secondary magnetic field is applied along the vertical direction that levitates the magnetically labeled cells to the upper surface of the culture medium. By doing so, an improved 3D cell-growth condition can be established that enables elicit phenotypes occurring in natural matrix environments, and the cells are more amenable to manipulation by the primary field.

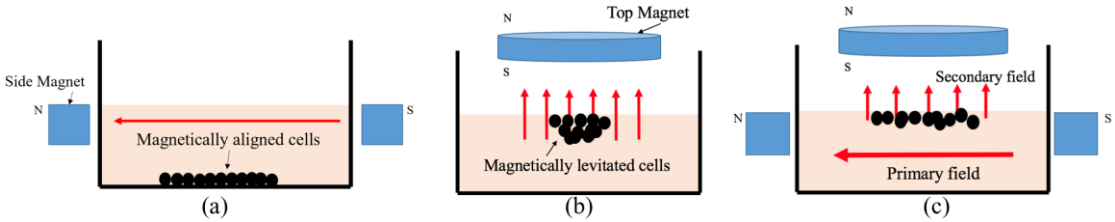

Figure 18. 3D cell culture scheme with magnetic levitation/alignment

The actual setup is shown in Figure 19 (a), where the primary field for magnetic manipulation is produced by two magnetic bars and the secondary field for magnetic levitation is generated by a disk-shaped magnet placed over the culture dish. As indicated in Figure 19 (b), two particles were levitated and aligned with the magnetic field with the test platform.

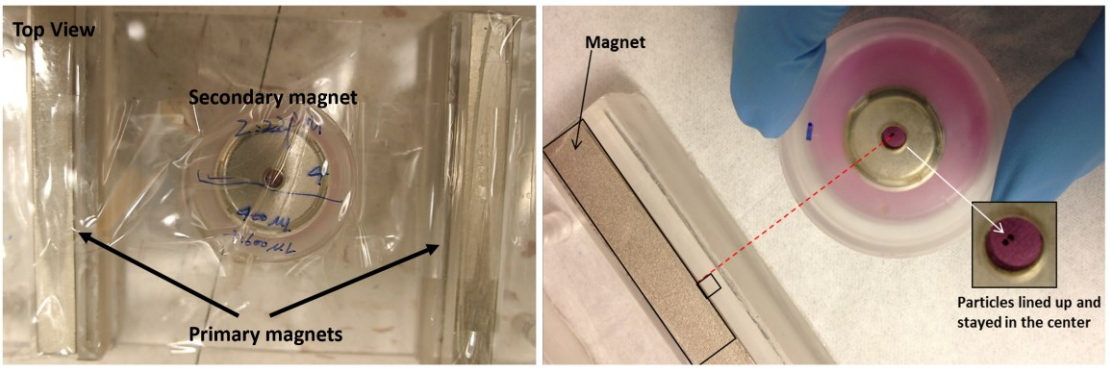

Figure 19 Test setup for 3D 3T3 cell self-assembly.

Briefly, the SPIONs-labeled 3T3 cells in this work were prepared as following:

1) Culture the cells to 80% confluence in a T-25 cell culture flask with 5 mL culture media, add 200 μL Nanoshuttle, and gently agitate the flask to evenly distribute the contents;
2) Incubate the cells for 24 hours, by the end of which the cells are magnetically labeled;
3) Remove the culture media, rinse off the residual nanoparticles with PBS, and harvest the cells with Trypsin solution;
4) Separate the cells into several 35x10mm petri culture dishes and add culture media till the average cell concentration is 247,500 cells per mL in each dish;
5) Place the culture dishes on the test setup and incubate the cells

To test the effect of magnetic levitation on the cell culture, only the secondary (disk-shaped) magnet is used in the first experimental configuration. Figure 20 (a) shows that, after 5 hours, magnetically labeled 3T3 cells are successfully levitated and form a loosely connected aggregate floating at the upper surface of the culture medium. At this point, the levitated cells are still fairly dispersed and the aggregation is held together mainly by the magnetic attraction forces. As time elapses, the cell assembly becomes more concentrated while cell-cell interaction was triggered. The micrographs taken after 2-day and 3-day incubation are shown in Figure 20 (b) to (d), respectively. Clearly,

Clusters of levitated 3T3 cells in the solution were concentrated by the applied magnetic field. Additionally, it is found that, given enough time, the overall morphology

of the cultured tissue is largely determined by the size and shape of the secondary magnet, suggesting the possibility of controlling the tissue formation by tailoring the distribution of the external magnetic fields.

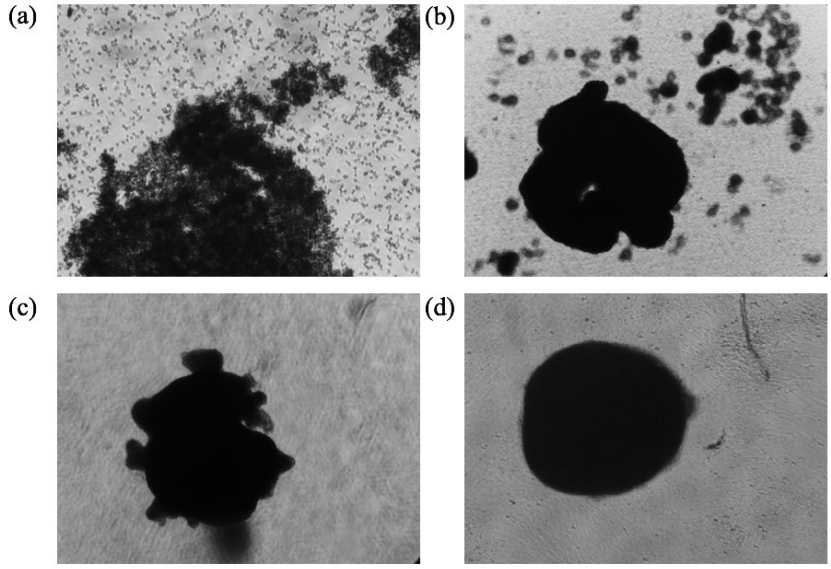

Figure 20 3D magnetic culture of 3T3 cells. (a) cells aggregate after 5-hour magnetic levitation; (b) and (c) cells form a cluster after 2-day and 3-day incubation under the larger magnet; (d) cells form a more concentrated cluster after 3-day incubation under the smaller magnet.

To further study the 3D 3T3 cell structure after the levitation, the secondary magnet was removed and the 3D cell structure was incubated for two more days. Without the levitation by the external magnetic field, Figure 21 demonstrates that the cells continue to grow and attached to the planar surfaces. Since there is no constraint from the magnetic forces, the cell growth follows a diffusive manner along all directions with an almost uniform growth rate, as indicated by a nearly circular pattern. Hence, the cellular viability of 3T3 cells is not impaired by the magnetic levitation of 3D cell culturing, and once magnetic levitation removed, 3T3 cells continuously grow in the conventional 2D monolayer culture.

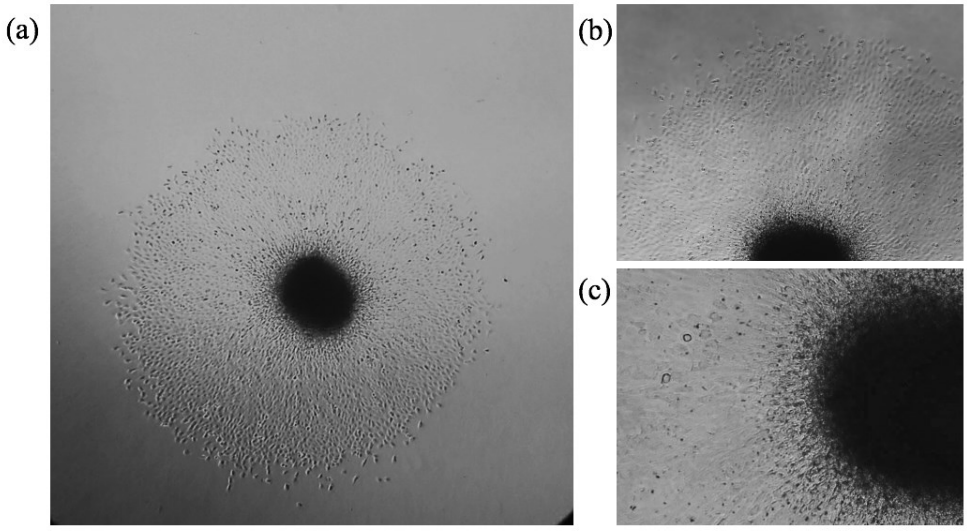

Figure 21 Viability of cellular self-assembly was tested. The assembly was transferred to a new plate and monitored under no effect of magnetic force after 2 days.

In the second experimental configuration, both the primary and secondary fields were present to achieve magnetic levitation and assembly simultaneously. 3T3 cells of were cultured with both magnetic fields on for 1.5 days. The column lattice formed by the cells along the field direction can be clearly observed in Figure 22(a). Micrographs of the cultured tissue at various magnifications are shown in Figure 22(b)-(e). As compared to the concentrated cell cluster in Figure 20 when only the secondary field was used, the packing density of cells is lower, however, the directional structure of the column lattice is well retained. Therefore, under an external magnetic field, the SPIONs labeled 3T3 cells spontaneously self-assemble into structured lattices along a virtural axis defined by the field flux lines. With its injectability, alignability and bioactivity, the study of 3T3 cells self-assembly process provides a fundamental understanding in bioscaffold for SCI treatment.

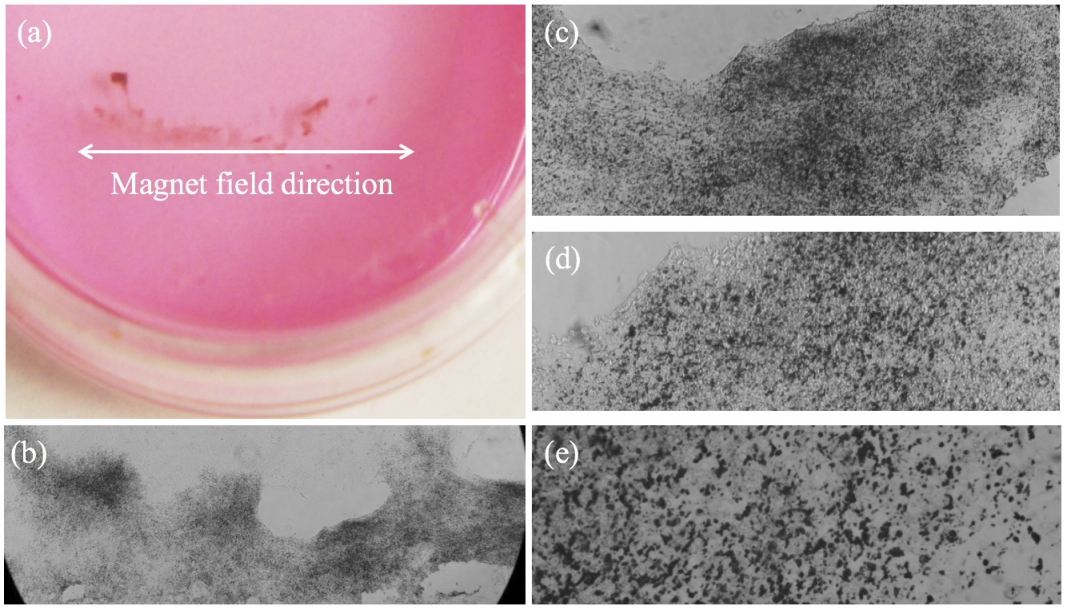

Figure 22 Chain lattice formed by levitated 3T3 cells with (a) no magnification, (b) 40 × magnification, (c) 100 × magnification, (d) 200 × magnification; and (e) 400 × magnification.

3.2.2 Neural Stem Cells (NSCs)

With the study of magnetic manipulation of 3T3 cells, NSCs were then investigated considering its unique feature and applications in SCI [80-82]. NSCs are self-renewing cells and they are the multipotent cells that generate the neurons and glia of the nervous, which can replace the lost neurons and oligodendrocytes to promote the remyelination of demyelinated and degenerated axons [83,84].

Compared to 3T3 monolayer culture feature , there are commonly two culturing method for NSCs in vitro, monolayer and suspension [85]. With conventional adherent monolayer culture method, the population propagation of NSCs is restricted on the planar substrate of the culture surface as showed in Figure 23 (a), while NSCs are maintained as free-floating cell without adherent conditions and tend to aggregate to neurospheres when cultured in suspension which allow the acquisition of 3D cell culture

(Figure 23 (b)).

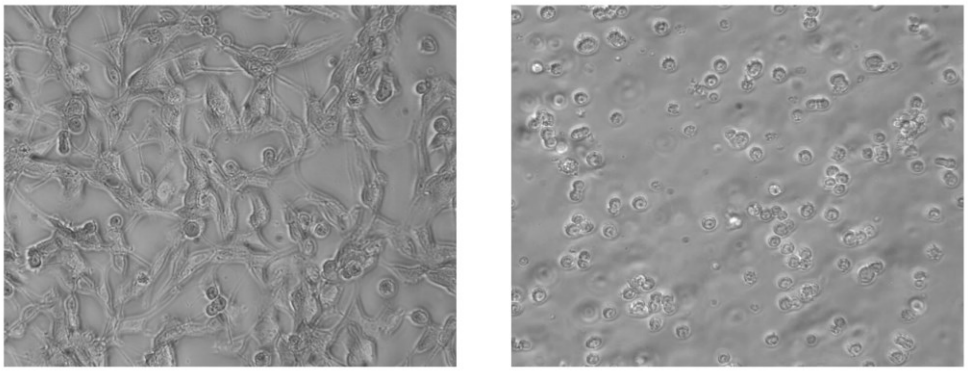

(a) (b)

Figure 23 NSCs culture in (a) monolayer, (b) suspension.

The NSCs aggregated in the form of neurospheres float freely in the culture medium, making them very responsive to magnetic manipulation. However, since SPIONs can only diffuse into cells at/near the outer surface of the neurosphere, the 3D spherical structure of neurospheres poses a serious limitation on the internalization of SPIONs. In contrast, NSCs can be labeled more effectively by the adherent monolayer culture method due to the 2D nature of the assay, but the substrate-cell adhesion reduces the cellular mobility and hinders the NSC alignment and pattern formation when the magnetic field is applied. In order to optimize the efficacy of magnetic manipulation, a hybrid version of suspension and adherent monolayer culture method was developed that enables both higher level of SPION internalization and lower resistance to cellular migration.

In the new procedure, an adherent monolayer culture was first used for NSCs to facilitate SPION uptake as it provides the larger overall cellular surface area exposed to the hydrogel. To do so, NSCs were seeded with Nanoshuttle and incubated for 24-48 hours in standard culture media at 37°C and 5% CO2. Before the magnetic assembly

experiment, the cells were washed multiple times with PBS to remove excess SPIONs and were then trypsinized into a suspension as free-floating cells. Figure 24 (b) shows the presence of SPIONs in the cells right after seeding. After 72 hours, the cells were trypsinzed and dispensed in new plate after centrifuged, the SPIONs were still observable inside the cell membrane (Figure 24 (c)) and no significant loss of SPIONs was found during the proliferation process.

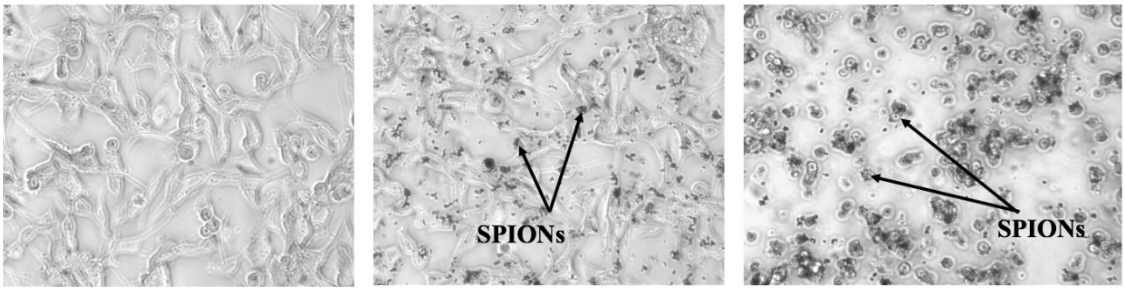

Figure 24 (a) NSCs without SPIONs, (b) NSCs immediately after seeding 100 µl SPIONs carrier, (c)labeled NSCs after 72-hour culture.

Then, the uniform magnetic field was created by two neodymium-iron-boron rare-earth magnet bars placed in parallel on a transparent fixture (shown in Figure 25 (a)). The strength of the magnetic field can be controlled by adjusting the distance between the magnet bars. 9 well plate was placed between the magnet bar where the SPION-labeled NSCs were cultured in suspension. With 24 hours incubation, it was found that NSCs were aggregates as several neurospheres and self-aligned as shown in Figure 25 (b).

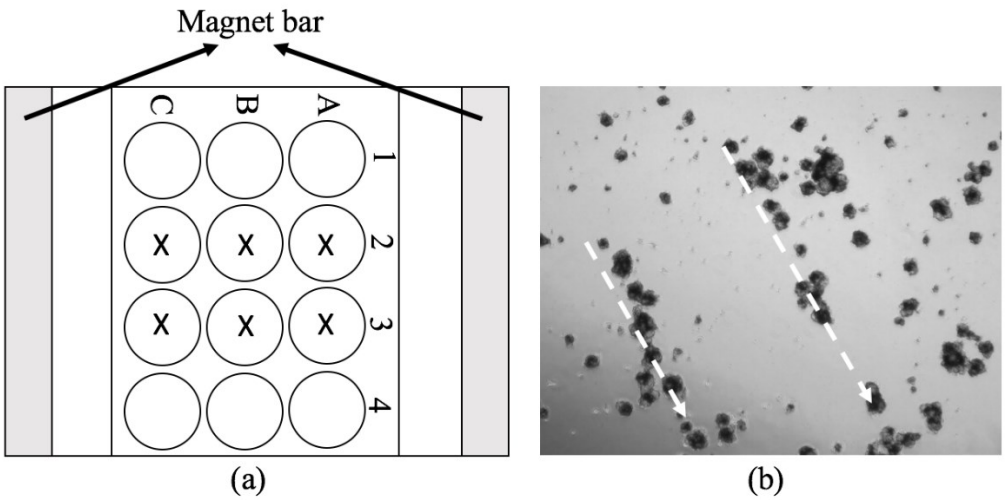

Figure 25 (a) Test fixture with adjustable magnetic field strenght, (b) SPIONs-labeled NSCs after 24-hour incubation

However, as continuously culturing in 3D suspension method, the structure of self-aligned NSCs became unstable. Instead of growing along self-aligned structure, NSCs and attached neurospheres tend to aggregates. While in SCI treatment, long-time bioactivity and shaped-stability are required because it takes 72 hours for axon growth and regeneration when co-cultured with scaffold. Therefore, to achieve the stable structure, the optimal procedures were then studied.

To mimic the linear morphology of nerves in the spinal cord, in this work, a magnet ring was employed to produce a curvilinear magnetic field. Following the hybrid culturing method, the NSCs were first cultured with the monolayer culture method for SPION uptake and then in suspension for magnetic manipulation. Subsequently, eight samples were studied. A magnet ring was placed above a 24 wells culture plate, as shown in in Figure 26, which serves the functions of both magnetic levitation and guided assembly of the NSC structure. The magnetic forces induced on the NSCs drive them to follow the profile of the magnetic field. After 48 hours

incubation, a curvilinear, arc-like structure was formed as shown in Figure 27(a).

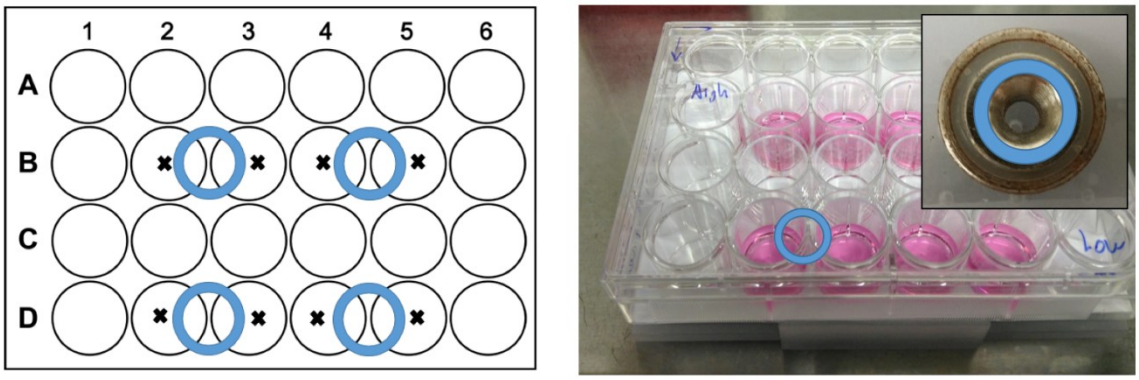

Figure 26 Test set up for NSC scaffold.

In order to identify the components of the structure, it was then stained with 4', 6-diamidino-2-phenylindoleis (DAPI) following the procedures below. DAPI is a fluorescent stain that binds strongly to adenine-thymine-rich regions in DNA, which fluoresces brightly at short exposure to purple light (wavelength 455 nm) and exhibits blue fluorescence [86]. The DAPI solution was prepared at a concentration of 1:1000 in PBS. After adding the DAPI solution, the solution containing the NSC structure was processed on an orbital shaker at room temperature for 30 minutes. Then, the DAPI solution was removed and more PBS was added. Using a fluorescent microscope, large numbers of stained cells can be observed, as shown in Figure 27(a) (b), which still maintain a stable arc structure. Multiple experiments were repeated to verify the structural stability and similar results were obtained which attests to the robustness of the NSC structure formed by this method.

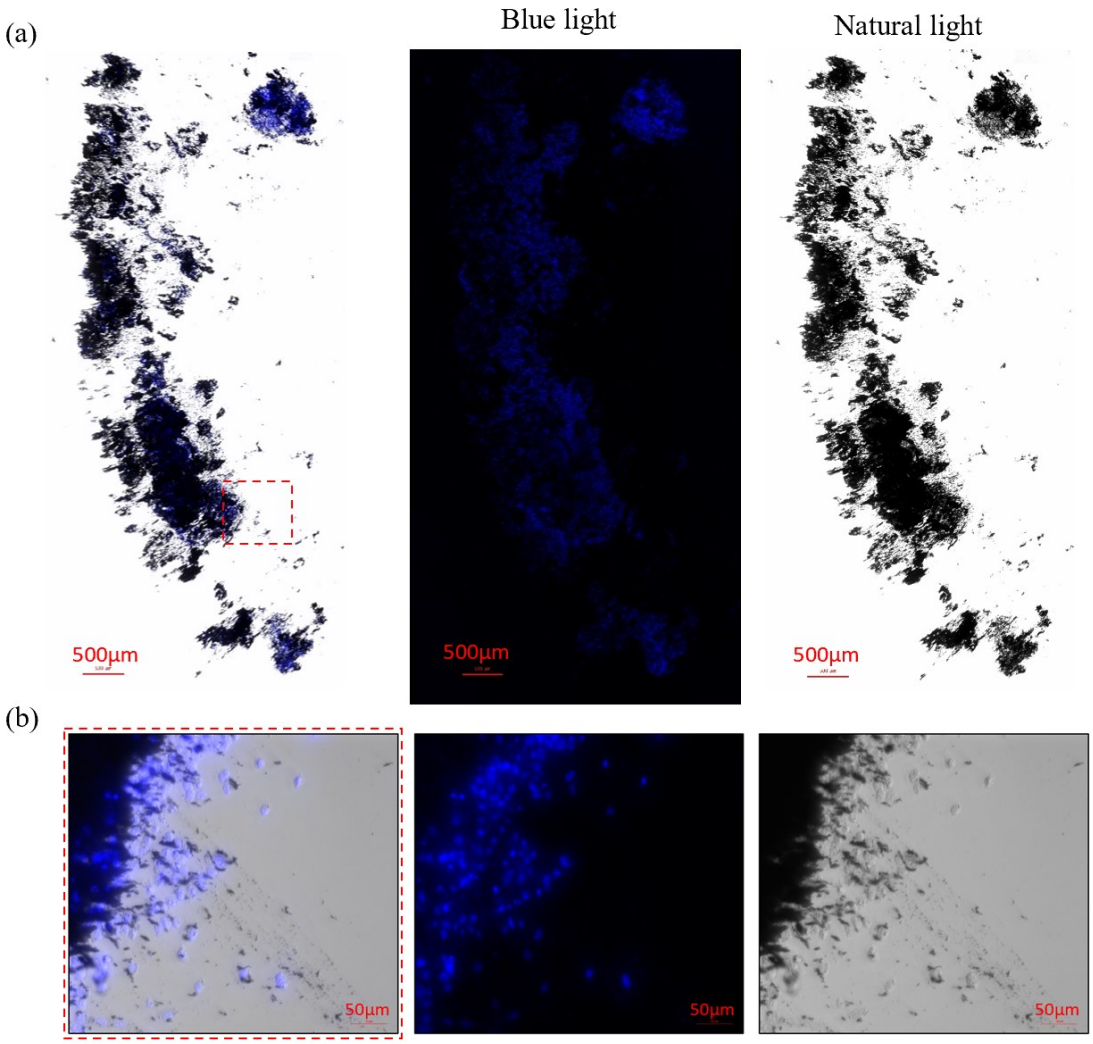

Figure 27 Self-assembled NSCs column structure after 48 hours cultivation, (a) 10 × magnification, (b) 20 × magnification

The NSC structure was further cultured for 72 hours under both top magnet ring and two side neodymium-iron-boron rare-earth magnet bars. Figure 28 shows that the individual NSCs continue to proliferate while the scaffold maintained a column shape. As a result, the scaffold becomes denser visually which indicates the NSC structure not only grows in the plane parallel to the magnet ring but also increases its thickness in the transverse plane, thus forming a truly 3D morphology.

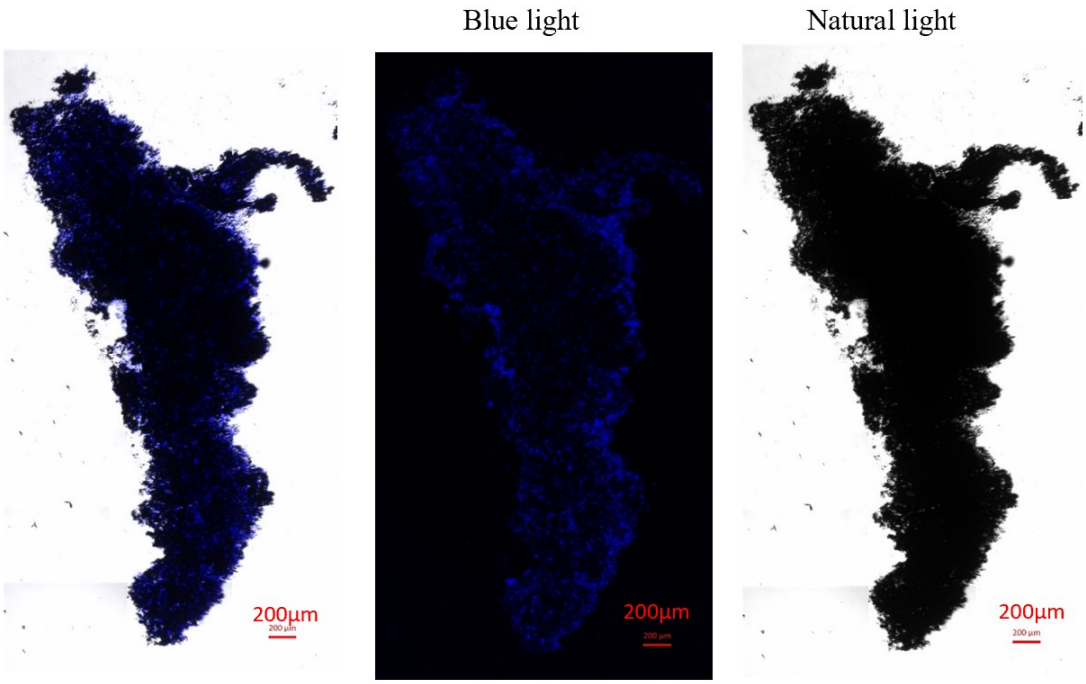

Figure 28 Self-assembled NSCs column structure after 72 hours cultivation

Chapter 4. Overview of Particle Manipulation Methods

In the fundamental research and clinical applications of biology and biomedicine, there is an increasing need for precise manipulation of bioparticles, such as cells, bacteria and viruses. Accordingly, a myriad of techniques have been developed to achieve particle focusing, separation and trapping by exploiting the interactions between the particles and the applied external fields, including optical [87,88], acoustic [], mechanical [89], microfluidic [90], electrical [91-93] and magnetic[94-96] fields. In particular, the uses of electric and magnetic fields have attracted significant interest due to their non-invasiveness, versatility and efficiency. In this chapter, the physical mechanisms and the mathematical formulations of electrical and magnetic manipulation of particles will be reviewed and some comparisons will be drawn to highlight the advantages and disadvantages of these two approaches.

4.1 Electrical Manipulation of Particles

Electrically-induced electrokinetic effects, such as electrophoresis (EP) and dielectrophoresis (DEP), can be employed for particle manipulation. EP operates on the electrostatic attraction between the electric field and charged particles [97,98],. It is insensitive to the size and physical properties of the particles, thus providing a feasible tool to control objects as large as cells and as small as single molecular. Further, EP has no specific requirements for the design of the electric field, i.e., it can be implemented under both uniform and nonuniform fields. However, in spite of the great flexibilities, EP does not work for electrically neutral particles, which encompass a large collection of important bioparticles that are dielectric in nature, such as water, air, glass.

Fortunately, this shortcoming can be overcome by DEP. When a dielectric particle is exposed to an external field, it will be polarized. During the polarization process, the positive and negative charges are redistributed momentarily while the particle remains electrically neutral, thus giving rise to an induced dipole across the particle. If the electrical field is non-uniform, the net Columbic force experienced by the dipole becomes nontrivial and will put the particle into motion [99,100]. Compared to EP, the dielectrophoretic behavior of particles is affected considerably by the physical properties of the particle, which makes DEP more selective and efficient for bioparticle detection and manipulation. In this work, the electrical manipulation of particles will focus on the use of DEP.

Dielectrophoretic motion of particles depends on a few factors, including the dielectric properties of the particle and the surrounding fluid medium, the geometry and dimensions of the particle, and the distribution of the applied field [101]. When multiple particles are present, the close proximity of neighboring particles not only alters the local electric field (and, therefore, the dielectrophoretic force) but also induces complex hydrodynamic interactions among the particles. Hence, it is an intricate task to acquire a good understanding of the DEP process for particle manipulation applications. Two prevailing approaches have been developed for this purpose, including the effective dipole moment approach and the Maxwell stress tensor (MST) approach.

4.1.1 Effective Dipole Moment Approach

For a point dipole exposed to an external field $\vec{E}$, it experiences an electric force $\vec{F}_{dipole} = (\vec{p} \cdot \nabla)\vec{E}$, where $\vec{p}$ is the dipole moment. The dipole induced on a dielectric

particle can be viewed as a collection of infinite number of point dipoles over the volume of the particle. Thus, the dielectrophoretic force on the particle $\vec{F}_{DEP}$ can be calculated as [101]

$$\vec{F}_{DEP} = \int_V (\vec{P} \cdot \nabla)\vec{E}\, dV, \tag{1}$$

where $\vec{P}$ is the polarization density in the particle owing to the induced dipole moment. A general evaluation of the integral in Eq. (34) is difficult since both $\vec{P}$ and $\vec{E}$ depend on the particular geometry of the particle and its orientation relative to the applied field. If the particle is considerably smaller than the nonuniformity of the electric field, the effective dipole moment approach provides a straightforward way to compute the dielectrophoretic force and the dielectrophoretic torque.

To do so, an effective dipole moment $\vec{p}_{eff}$ is first defined which is equivalent to the actual dipole moment of the particle when placed in the same medium and at the same location. For a spherical particle, the effective dipole moment $\vec{p}_{eff}$ is expressed as [102]

$$\vec{p}_{eff} = 4\pi a^3 \varepsilon_m \left(\frac{\varepsilon_p - \varepsilon_m}{\varepsilon_p + 2\varepsilon_m}\right)\vec{E}, \tag{2}$$

where a is the particle radius, ε_m and ε_p are the electrical permittivities of the fluid medium and the particle, respectively, and $\vec{E}$ is the applied electric field. Introducing the Clausius-Mossotti (CM) factor

$$K \equiv \left(\frac{\varepsilon_p - \varepsilon_m}{\varepsilon_p + 2\varepsilon_m}\right), \tag{3}$$

which provides a measure of the relative polarizability of the particle with respect to the

fluid, the expression of $\vec{p}_{eff}$ can be re-written as

$$\vec{p}_{eff} = 4\pi a^3 \varepsilon_m K \vec{E}. \tag{4}$$

As will be seen later, this expression also facilitates the extension of DEP in AC fields.

Subsequently, the effective dielectrophoretic force $\vec{F}_{DEP}$ becomes

$$\vec{F}_{DEP} = \left(\vec{p}_{eff} \cdot \nabla\right)\vec{E} \tag{5}$$

or, explicitly

$$\vec{F}_{DEP} = 2\pi a^3 \varepsilon_m \left(\frac{\varepsilon_p - \varepsilon_m}{\varepsilon_p + 2\varepsilon_m}\right) \nabla E^2 = 2\pi a^3 \varepsilon_m K\left(\varepsilon_p, \varepsilon_m\right) \nabla E^2 \tag{6}$$

According to Eq. (6), the dielectrophoretic force $\vec{F}_{DEP}$ does not always align with the gradient of E^2, but, rather, it depends on the sign of K. If $K > 0$, the particle is more polarizable than the fluid medium and $\vec{F}_{DEP}$ will drive the particle towards the region of higher electric field gradient. This process is called positive DEP (pDEP). Conversely, if $K < 0$, the particle will be repelled from the field maxima and be attracted to the field minima, i.e., negative DEP (nDEP) occurs.

In addition to translational motion, the particle is also subject to rotation, which is governed by the electrorotation (ROT) torque $\vec{\tau}_{DEP}$

$$\vec{\tau}_{DEP} = \vec{p}_{eff} \times \vec{E}. \tag{7}$$

It is forthgoing to apply Eqs. (6) and (7) in analyzing DEP driven by a direct current (DC) electric field. When an alternating current (AC) field is used, a time-dependent expression can be obtained for the instantaneous dielectrophoretic force [103]

$$\vec{F}_{DEP} = 2\pi a^3 \varepsilon_m Re[K] \nabla E^2, \tag{8}$$

where Re$[K]$ represents the real part of a complex Clausius-Mossotti factor, which is

given as

$$K = \frac{\varepsilon_p^* - \varepsilon_m^*}{\varepsilon_p^* + 2\varepsilon_m^*}. \tag{9}$$

Here ε_m^* and ε_p^* are the complex permittivities of the fluid medium and the particle, respectively, and

$$\varepsilon^* = \varepsilon - i\frac{\sigma}{\omega}. \tag{10}$$

According to this expression, the complex permittivity ε^* is related to the electrical conductivity of the material σ and the angular frequency of the electric field ω ($= 2\pi f$ where f is the frequency of the field).

Due to its simplicity, the effective dipole moment method has been widely employed in the study of DEP. However, several serious limitations exist. First, this method is valid only when the particle size is small compared to the nonuniformity in the electric field. Under certain circumstance, for example, when the particles are closely packed or they are located near the electrodes, the local field becomes highly distorted and nonuniform, the effective dipole moment approach will lose its ground. Second, it is difficult to derive general expressions for $\vec{F}_{DEP}$ for particles of irregular (e.g., non-spherical) shape, whereas Eq. (2) developed for spherical particles cannot give a full account of the dynamics of the particle motion and large errors will arise when DEP is coupled to the hydrodynamic interactions with the surrounding medium.

4.1.2 Maxwell Stress Tensor Approach

When particle-particle interactions are no longer negligible or the particles are located in the vicinity of the electrodes, the prediction of $\vec{F}_{DEP}$ using the effective dipole

moment method becomes questionable. An alternative method is offered by the Maxwell stress tensor (MST) approach, which is applicable to particles of arbitrary shape even with particle-particle and particle-field interactions [104].

The Maxwell stress tensor $\overleftrightarrow{T}$ orginiates from the interaction between the electromagnetic forces and the mechanical momentum of an object. For a point charge q moving freely in a homogeneous electromagnetic field, it experiences a force that can be calculated from the Lorentz force formula [105]

$$\vec{F} = q\left(\vec{E} + \vec{v} \times \vec{B}\right), \tag{11}$$

where $\vec{E}$ is the electric field, $\vec{\mathrm{v}}$ is the charge velocity, and $\vec{B}$ is the magnetic flux density. For a continuous distribution of charges, the total electromagnetic force must be evaluated from a volume integral

$$\vec{\mathrm{F}} = \int_{\upsilon} \rho(\vec{E} + \vec{\mathrm{v}} \times \vec{B})\, dV, \tag{12}$$

where ρ is the charge density. The Maxwell stress tensor is introduced to simplify the force equation.

In a static field, by applying the Gauss's theorem, Eq. (12) can be rewritten as

$$\vec{\mathrm{F}} = \oint_s \overleftrightarrow{T} \cdot d\vec{a}, \tag{13}$$

where the integration is performed over the entire outer surface of the particle, and $\overleftrightarrow{T}$ is the Maxwell stress tensor

$$\overleftrightarrow{T} = \varepsilon\left(\vec{E}\vec{E} - \frac{1}{2}E^2\overleftrightarrow{I}\right) + \frac{1}{\mu}\left(\vec{B}\vec{B} - \frac{1}{2}B^2\overleftrightarrow{I}\right). \tag{14}$$

Here, μ is the magnetic permeability and $\overleftrightarrow{I}$ is the unit tensor. Similar to the stress tensor in continuum mechanics, T_{ij} is a symmetric second-order tensor, i.e., $T_{ij} = T_{ji}$.

Physically, T_{ii} represents the normal stress (the pressure) acting on the element surface, whereas the rest of the elements T_{ij} $(i \neq j)$ are the shear stresses. For DEP applications, only the electric field is relevant and, thus,

$$\overleftrightarrow{T} = \varepsilon\left(\vec{E}\vec{E} - \frac{1}{2}E^2\overleftrightarrow{I}\right). \tag{15}$$

Subsequently, the DEP force becomes

$$\vec{F}_{DEP} = \oint\left(\overleftrightarrow{T} \cdot \overrightarrow{n}\right)dA, \tag{16}$$

and the electrorotation torque $\vec{\tau}_{DEP}$ can be obtained

$$\vec{\tau}_{DEP} = \oint \overrightarrow{r} \times \left(\overleftrightarrow{T} \cdot \overrightarrow{n}\right)dA, \tag{17}$$

where $\overrightarrow{r}$ is the position vector, $\overrightarrow{n}$ is the unit normal vector at a point on the particle surface, and A is the surface area.

4.2 Magnetic Manipulation of Particles

Electrical manipulation of particles by DEP is label free, low in power consumption and highly sensitive to particle types [106-108] However, this technique requires the micro/nanofabrication of electrodes and suffers from possible particle damages due to Joule heating when an electrical current is passed through the electrolyte solution [109,110]. Recently, magnetic particle manipulation has found unique niche applications for being completely noninvasive and cold-state at operation. Furthermore, magnetic manipulation is independent of the pH value and ionic strength of the solution and the surface charge of particles.

Magnetic manipulation of particles depends on the extent the constituent

material can be magnetized by an external magnetic field, which is measured by the magnetic susceptibility χ_m. In ferromagnetic materials, the inherent magnetic dipoles are permanent and they align spontaneously to the external field. In fact, the magnetization in ferromagnetic materials can be 10^4 times larger than the applied field in most cases [111]. By comparison, the responses of diamagnetic and paramagnetic materials to the external field are fairly weak and only exist when the field is present. In diamagnetic materials, the induced magnetic dipoles orient in a direction opposite to the external field, leading to a negative magnetic susceptibility on the order of -10^{-6} to -10^{-3}. In paramagnetic materials, the magnetic field is slightly enhanced due to the superposition of the induced magnetic dipoles with the external field. The magnetic susceptibility of paramagnetic materials is in the range of 10^{-6} to 10^{-1}. At present, magnetic particle manipulation is conducted almost exclusively for paramagnetic materials, since the magnetization is too strong in ferromagnetic materials and too weak in diamagnetic materials to allow controllable particle motion.

Magnetic particles can be magnetized and forced into motion in the presence of a nonuniform magnetic field due to the magnetic dipole-field interactions, very analogous to what happens in DEP. The so-called magnetophoresis (MAP) process was first applied for biological particle sorting and proven to be very effective in yielding high sensitivity, resolution and specificity [112-114]. Lately, the number of investigations on MAP surged exponentially as the demand for particle sorting, separation and focusing applications in biomedical research increased dramatically and a variety of novel magnetic nanoparticles (MNPs) were made available owing to the development of new synthesis techniques [115-117]. Compared to the mature research

field of DEP, most studies of MAP are application-driven and application-specific, and there is no systematic theoretical and numerical investigations of MAP, particularly, related to its coupling with the hydrodynamic field and particle-particle interactions. Therefore, MAP is then studied.

4.2.1 Effective Dipole Moment Approach

The magnetic force on a single magnetic dipole can be derived as [118]

$$\vec{F}_M = \nabla\left(\vec{m} \cdot \vec{B}\right), \tag{18}$$

where $\vec{\mathrm{m}}$ is the magnetic dipole moment. Since $\vec{\mathrm{m}}$ is not a function of the spatial coordinates, $(\vec{B} \cdot \nabla)\vec{\mathrm{m}} = 0$, and the magnetic field is irrotational, $\nabla \times \vec{\mathrm{B}} = 0$, the magnetic force reduces to

$$\begin{aligned} \vec{F}_M = & \left(\vec{B} \cdot \nabla\right)\vec{m} + (\vec{m} \cdot \nabla)\vec{B} + \vec{B} \times (\nabla \times \vec{m}) + \vec{m} \times \left(\nabla \times \vec{B}\right) \\ & = (\vec{m} \cdot \nabla)\vec{B}. \end{aligned} \tag{19}$$

Similarly, the torque on magnetic dipole can be derived as [105]

$$\vec{N} = \vec{m} \times \vec{B}. \tag{20}$$

Since a real particle, no matter how small its size is, cannot be represented by a single dipole, an effective dipole moment $\vec{m}_{eff}$ must be defined to enable easy and valid prediction of the magnetic force and torque on a particle. For a homogenous spherical particle suspended in a magnetically linear medium, $\vec{m}_{eff}$ is given by [102]

$$\vec{m}_{eff} = 4\pi a^3 \left[\frac{\mu_0 - \mu_m}{\mu_0 + 2\mu_m}\vec{H} + \frac{\mu_0}{\mu_0 + 2\mu_m}\vec{M}_p\right], \tag{21}$$

where a is the radius of particle, μ_0 is the magnetic permeability of free space (= $4\pi \cdot 10^{-7}$ H/m), μ_m is the magnetic permeability of the medium, $\vec{M}_p$ is the volume

magnetization of the particle, and $\vec{H}$ is the external magnetic field. The relation between $\vec{H}$, $\vec{\mathrm{B}}$ and $\vec{M}$ is

$$\vec{\mathrm{B}} = \mu_0(\vec{H} + \vec{M}). \tag{22}$$

When considering the limiting case where the magnetic particle is in vacuum, $\mu_0 = \mu_m$, Eq. (21) becomes

$$\vec{m}_{eff} = \frac{4}{3}\pi a^3 \vec{M}_p. \tag{23}$$

Thus, it can be seen that the first term on the RHS of Eq. (21) is due to the net moment of the medium by the displacement of particle and the second term is contributed by the magnetization of the particle itself.

Further, if the particle is made of a linear magnetic material, it follows

$$\vec{M}_p = \chi_p \vec{H}, \tag{24}$$

where $\chi_p = \frac{\mu_p}{\mu_0} - 1$ (μ_p is the magnetic permeability of the particle). Subsequently, Eq. (21) can be reformatted in analogy to the effective dipole moment of a dielectric particle

$$\vec{m}_{eff} = 4\pi a^3 \frac{\mu_p - \mu_m}{\mu_p + 2\mu_m} \vec{H} = 4\pi a^3 K_M \vec{H}. \tag{25}$$

The factor $\mathrm{K}_M = \frac{\mu_p - \mu_m}{\mu_p + 2\mu_m}$ has a similar physical meaning as the Clausius-Mossotti factor in dielectrics. Combining Eqs. (19) and (25), the MAP force from the effective dipole moment approach becomes

$$\vec{F}_{MAP} = (\vec{m}_{eff} \cdot \nabla)\vec{B} = 4\pi a^3 \mu_m \frac{\mu_p - \mu_m}{\mu_p + 2\mu_m} (\vec{H} \cdot \nabla)\vec{H}, \tag{26}$$

since $(\vec{H} \cdot \nabla)\vec{H} = \frac{1}{2} \nabla \vec{H}$, it leads to

$$\vec{F}_{MAP} = 2\pi a^3 \mu_m \left(\frac{\mu_p - \mu_m}{\mu_p + 2\mu_m}\right) \nabla H^2. \tag{27}$$

Thus, MAP can also be categorized to positive MAP and negative MAP, depending on the relative permeability of the particle and the medium. If $\mu_p > \mu_m$, the particle will be attracted to the maxima of the magnetic field and the MAP is "positive". Conversely, if $\mu_p < \mu_m$, MAP is negative and the particle is repelled from the maxima.

Similarly, the magnetic toque exerted on the particle using the effective dipole moment approach is

$$\vec{\tau}_{MAP} = \vec{m}_{eff} \times \vec{B} = \mu_m \vec{m}_{eff} \times \vec{H}. \tag{28}$$

4.2.2 Maxwell Stress Tensor Approach

The effective dipole moment approach for the MAP analysis suffers similar drawbacks as for DEP. Thus, the Maxwell stress tensor approach is extended to compute the magnetic force density $\vec{f}_m$ as [119]

$$\vec{f}_m = \nabla \cdot \overleftrightarrow{T}_M, \tag{29}$$

where the Maxwell stress tensor $\overleftrightarrow{T}_M$ is given by

$$\overleftrightarrow{T}_M = \mu \left(\vec{H}\vec{H} - \frac{1}{2} H^2 \overleftrightarrow{I}\right). \tag{30}$$

The MAP force can be obtained by integrating Eq. (74) over the volume of the particle and applying Gauss's theorem

$$\vec{F}_{MAP} = \int_V \nabla \cdot \overleftrightarrow{T}_M dV = \oint \left(\overleftrightarrow{T}_M \cdot \vec{n}\right) dA = \oint \mu \left(\vec{H}\vec{H} - \frac{1}{2} H^2 \overleftrightarrow{I}\right) \cdot \vec{n}\, dA$$
$$= \oint \left(\mu (\vec{H} \cdot \vec{n}) \vec{H} - \frac{1}{2} \mu H^2 \vec{n}\right) dA, \tag{31}$$

and the magnetic torque $\vec{\tau}_{MAP}$ is [120]

$$\vec{\tau}_{MAP} = \oint \vec{r} \times \left(\overleftrightarrow{T}_M \cdot \vec{n}\right) dA, \tag{32}$$

where $\vec{r}$ is the position vector and $\vec{n}$ is the unit normal vector at a point on the particle surface.

Chapter 5. Numerical Model and Physical Equations

This chapter first provides a brief review of the basic theories of fluid mechanics and electromagnetism to lay the foundation for studying the complex problem of multiphysics-based fluidic manipulation of particles. Then, the physical modules and numerical methods implemented in the software package, COMOSOL®, will be introduced.

5.1 Fluid Mechanics

In this work, the fluid is treated as incompressible and Newtonian. The continuity equation and the Navier-Stokes equation of fluid motion are

$$\nabla \cdot \vec{u} = 0 \tag{33}$$

and

$$\frac{\partial(\rho\vec{u})}{\partial t} + \rho(\vec{u} \cdot \nabla\vec{u}) = \nabla \cdot \vec{\vec{\sigma}} + \rho\vec{g}, \tag{34}$$

where ρ is the density of the fluid, $\vec{u}$ is the velocity, t is time, $\vec{g}$ is the acceleration of gravity and $\vec{\vec{\sigma}}$ is the Cauchy stress tensor

$$\vec{\vec{\sigma}} = -p\vec{\vec{I}} + 2\mu\vec{\vec{D}}[\vec{u}], \tag{35}$$

in which p is the fluid pressure, μ is the fluid viscosity, and $\vec{\vec{D}}[\vec{\mathrm{u}}]$ is the rate of strain tensor

$$\vec{\vec{D}}[\vec{u}] = \frac{1}{2}[\nabla\vec{u} + (\nabla\vec{u})^T]. \tag{36}$$

5.2 Electric Field

In a dielectric material, the Gauss's law relates the free charge density ρ_e to the electric displacement (electric flux density) $\vec{\mathrm{D}}$ as

$$\nabla \cdot \vec{D} = \rho_e. \tag{37}$$

Further, $\vec{\mathrm{D}}$ is defined as

$$\vec{D} \equiv \varepsilon_0 \vec{E} + \vec{P}, \tag{38}$$

where ε_0 is the electric permittivity of free space ($\varepsilon_0 = 8.85 \times 10^{-12}\ F/m$), $\vec{E}$ is the electric field, and $\vec{P}$ is the polarization density. If the material is homogeneous and linear, $\vec{P} = \varepsilon_0 \chi_e \vec{E}$, the electric displacement $\vec{\mathrm{D}}$ can be rewritten as

$$\vec{D} = \varepsilon_0 \vec{E} + \vec{P} = \varepsilon_0 (1 + \chi_e)\vec{E} = \varepsilon_0 \varepsilon_r \vec{E} = \varepsilon \vec{E}. \tag{39}$$

In this equation, χ_e is the electric susceptibility, $\varepsilon_r = 1 + \chi_e$ is the relative permittivity, and $\varepsilon = \varepsilon_0 \varepsilon_r$ is the absolute permittivity.

Now, substituting Eq. (39) into Eq.(37), Gauss's law transforms to

$$\nabla \cdot \left(\varepsilon \vec{E}\right) = \rho_e. \tag{40}$$

In electrostatics, the electric field is irrotational, i.e., $\nabla \times \vec{E} = 0$. Thus, an electrostatic potential ϕ can be defined as

$$\vec{E} = -\nabla \phi. \tag{41}$$

Subsequently, Gauss's equation becomes

$$\nabla^2 \phi = \frac{\rho_e}{\varepsilon}. \tag{42}$$

Based on proper boundary conditions, the solutions of Eqs.(40) –(42) provide a complete description of the electric field that will be used for further calculation of the electric force and torque in dielectrophoresis.

5.3 Magnetic Field

The magnetic field in a magnetic material follows Ampere's law

$$\nabla \times \vec{H} = \vec{J}, \tag{43}$$

where $\vec{H}$ is the magnetic field and $\vec{J}$ is the current density. For the applications of magnetic manipulation of particles, magnetophoresis, a magnetokinetic effect, is employed as the driving mechanism, which utilizes permanent magnets as the source. Therefore, no current flow is involved and Eq. (43) is simplified to

$$\nabla \times \vec{H} = 0. \tag{44}$$

Consider the magnetic field as irrotational, a magnetic scale potential ψ can be defined as

$$\vec{H} = -\nabla\psi. \tag{45}$$

Further, $\vec{H}$ is related to the magnetization $\vec{M}$ and the magnetic flux density $\vec{B}$ by

$$\vec{H} = \frac{\vec{B}}{\mu_0} - \vec{M}, \tag{46}$$

where μ_0 is the magnetic permeability of free space ($\mu_0 = 1.257 \times 10^{-6}\ H/m$). For a linear material, the magnetization is proportional to the field, i.e., $\vec{M} = \chi_m \vec{H}$, where χ_m is the magnetic susceptibility. Thus, a new relation between $\vec{H}$ and $\vec{B}$ can be deduced

$$\vec{B} = \mu_0(1 + \chi_m)\vec{H} = \mu_0\mu_r\vec{H} = \mu\vec{H}, \tag{47}$$

where $\mu_\mathrm{r} = 1 + \chi_m$ is the relative permeability and $\mu = \mu_0(1 + \chi_m)$ is the permittivity of the material.

Based on Gauss's law for magnetism

$$\nabla \cdot \vec{B} = 0, \tag{48}$$

it follows

$$\nabla \cdot \vec{B} = \nabla \cdot \mu\vec{H} = \nabla \cdot \mu(-\nabla\psi) = 0. \tag{49}$$

Consequently, Gauss's equation for linear magnetic material with no current flow becomes

$$\nabla^2\psi = 0. \tag{50}$$

The solutions of Eqs. (48) – (74) determine the magnetic field that will be used to compute the magnetic force and torque in magnetophoresis.

5.4 Particle Motion

The key to particle manipulation is the ability to precisely control the motion of the particles of interest in the fluid medium. In the presence of an applied electric or magnetic field, the coupling between the hydrodynamic forces and the electric/magnetic forces arising from the external fields plays a crucial role in the particle motion.

Figure 29 shows the schematic of the physical domain, in which two representative particles are suspended in a viscous fluid. It is understandable that a total number of *N* particles may be present and the *i*-th particle is the particle of interest that is interacting with the rest of $N - 1$ particles. The solid boundary of the *i*-th particle is denoted by by Γ_i and the space occupied by the fluid is indicated by Ω. The location of the *i*-th particle is represented by the vector $\vec{x}_{c,i}$ that connects the center of the particle to the origin of the coordinate system. The motion of the *i*-th particle is described by its translational and rotational behaviors, governed by the classical mechanics:

Translational momentum

$$m_i \frac{d\vec{U}_i}{dt} = \sum_{j \neq i}^{N} \vec{F}_{i,j}, \tag{51}$$

Angular momentum

$$I_i \frac{d\vec{\omega}_i}{dt} = \sum_{j \neq i}^{N} \vec{T}_{i,j}. \tag{52}$$

In these equations, m_i is the mass of the particle, $\vec{U}_i$ is the translational velocity, I_i is the moment of inertia, $\vec{\omega}_i$ is the angular velocity, $\vec{F}_{i,j}$ is the external force exerted by the j-th particle, and $\vec{T}_{i,j}$ is the external torque induced by the j-th particle.

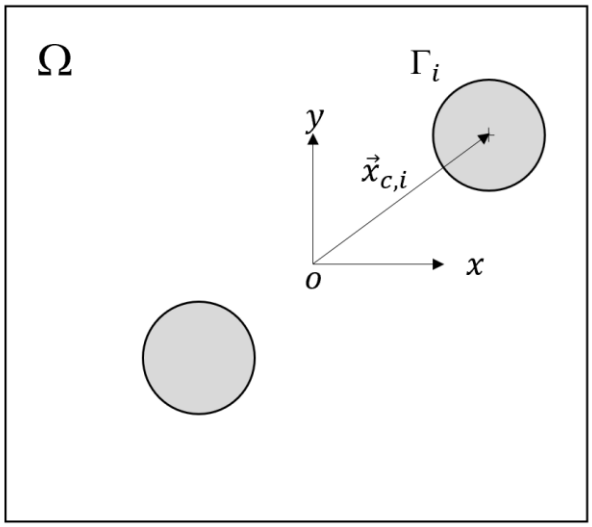

Figure 29. Scheme of simulation domain.

The force terms on the RHS of the translational momentum equation (Eq.(51)) include the hydrodynamic forces due to viscous drag in the fluid as well as the induced forces due to the applied electric or magnetic field. The former can be calculated by integrating the Cauchy stress tensor over the particle surface once the flow field is known

$$\vec{F}_{h,i} = \int_{\Gamma_i} (\overleftrightarrow{\sigma_i} \cdot \vec{n}\,) dA = \int_{\Gamma_i} [-p\overleftrightarrow{I} + \mu(\nabla\vec{u} + \nabla\vec{u}^T)] \cdot \vec{n}\, dA. \tag{53}$$

The external forces, i.e., the dielectrophoretic or magnetophoretic force, can be obtained by integrating the corresponding Maxwell stress tensors $\overleftrightarrow{T}_{E,i}$ and $\overleftrightarrow{T}_{M,i}$ over the particle surface as below

$$\vec{F}_{DEP,i} = \int_{\Gamma_i} (\overleftrightarrow{T}_{E,i} \cdot \vec{n}\,) dA \tag{54}$$

and

$$\vec{F}_{MAP,i} = \int_{\Gamma_i} (\overleftrightarrow{T}_{M,i} \cdot \vec{n}\,) dA, \tag{55}$$

where $\vec{n}$ is the unit normal vector at a point on the particle surface, A is the surface area, and the Maxwell stress tensors are

$$\overleftrightarrow{T}_{E,i} = \varepsilon \left(\vec{E}\vec{E} - \frac{1}{2} E^2 \overleftrightarrow{I} \right) \tag{56}$$

and

$$\overleftrightarrow{T}_{M,i} = \mu \left(\vec{H}\vec{H} - \frac{1}{2} H^2 \overleftrightarrow{I} \right). \tag{57}$$

The derivations of $\overleftrightarrow{T}_{E,i}$ and $\overleftrightarrow{T}_{M,i}$ are detailed in Chapter 4.

The rotational motion of the particle is determined by the torques acting on the particle due to the respective forces, which include the hydrodynamic torque $\vec{T}_{h,i}$, the dielectrophoretic torque $\vec{T}_{DEP,i}$ and the magnetophoretic torque $\vec{T}_{MAP,i}$

$$\vec{T}_{h,i} = \int_{\Gamma_i} (\vec{x}_{s,i} - \vec{x}_{c,i}) \times (\overleftrightarrow{\sigma_i} \cdot \vec{n}) dA, \tag{58}$$

$$\vec{T}_{DEP,i} = \int_{\Gamma_i} (\vec{x}_{s,i} - \vec{x}_{c,i}) \times (\overleftrightarrow{T}_{E,i} \cdot \vec{n}) dA, \tag{59}$$

and

$$\vec{T}_{MAP,i} = \int_{\Gamma_i} (\vec{x}_{s,i} - \vec{x}_{c,i}) \times (\vec{\overline{T}}_{M,i} \cdot \vec{n}) dA. \tag{60}$$

It is seen from the above equations that the translation and rotation of the particle are closely tied to the flow field in a two-way coupled manner, i.e.,, the particle motion is retarded by the viscous drag and, meanwhile, it disturbs the fluid motion in the near field around it. Thus, the coupling between the particle and the fluid is enforced by the no-slip condition at the surface of the particle

$$\vec{u}_i = \vec{U}_i + \vec{\omega}_i \times (\vec{x}_{s,i} - \vec{x}_{c,i}), \tag{61}$$

where $\vec{x}_{s,i}$ and $\vec{x}_{c,i}$ are the position vectors for the center and an arbitrary point on the surface of the particle, respectively, as shown in Figure 30.

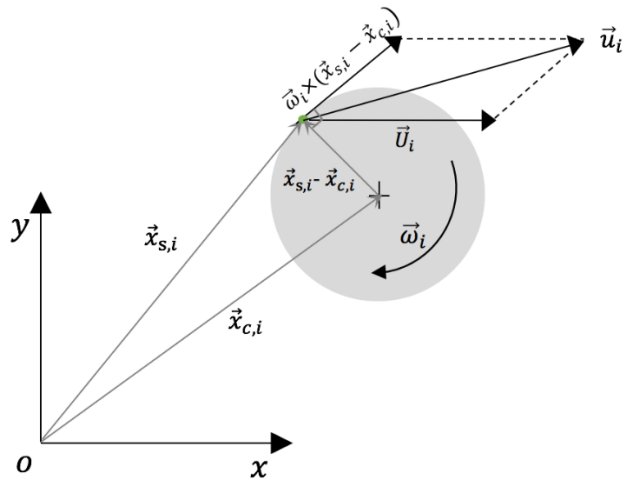

Figure 30 Schematic diagram of velocity in the surface of particle.

5.5 Numerical Models

It remains a huge challenge to acquire solutions to the highly coupled equation systems represented by Eqs. (51) to (74). Luckily, with the burgeoning development in computational techniques, a variety of numerical methods are available to provide high-

fidelity simulations for such a multi-physics problem with good performance-to-cost ratio. For this work, the finite element method (FEM) is chosen which is widely applied in many engineering and scientific field, such as structural analysis, heat transfer, fluid dynamics and electromagnetic potential [121-124]. As the numerical method for solving partial differential equation, FEA subdivides structures to small elements and approximate solutions to boundary value problems with different types of discretization method which is capable to simulate complex geometry [125].

For implementation, a FEM-based software package, COMOSOL Multiphysics®, is chosen as the platform to simulate particle manipulation by dielectrophoresis and magnetophoresis. COMOSOL® is designed to address a wide range of physical processes, including fluid flow, solid mechanics, electrodynamics and more [126,127]. The predefined modules in the library of COMOSOL® allow the users to set up and solve multiphysics problems without having to attend to the mathematical details of the governing equations. At the same time, customized differential equations can be added for specific problems, which can be input in either classic form, coefficient form or weak form. Moreover, besides the capability of combing multiple differential equations within a single physical module, multiphysics problems can be also studied by coupling multiple physical modules within the adjacent model domains.

5.6 Arbitrary Lagrangian-Eulerian (ALE) Method

The arbitrary Lagrangian-Eulerian (ALE) finite element method is utilized in COMSOL to address the strong coupling between the particle-field, particle-fluid and particle-particle interactions. As ALE combined the feature of both Lagrangian and

Eulerian method, it allows the computational mesh inside the domains to move arbitrary to optimize the shapes of elements while the mesh on the boundaries and interfaces of the domain can move along materials to precisely track the boundaries and interfaces of a multi-material system [128].

The Lagrangian formulation solves the partial differential equations in a material coordinate system which is fixed to the material in its reference configuration and following the material as it deforms, whereas in the Eulerian method, the partial differential equations of a problem are usually formulated in a spatial coordinate system with coordinate axes fixed in space. When studying structural mechanics and other fields of physics dealing with anisotropic, solid materials, it is most convenient to adopt the material coordinates since the anisotropic material properties are independent of the current spatial orientation of the material in the Lagrangian formulation. If the focus is on simulating the physical state at fixed points in space, the Eulerian formulation is usually more convenient, especially when liquid and gases are involved, the quantities at fixed positions in space such as pressure, temperature, concentration are more important than following the state of individual material particles. However, an essential problem with the pure Eulerian formulation is that it cannot handle moving domain boundaries while the set of spatial points inside the domain boundaries vary with time. Therefore, arbitrary Lagrangian-Eulerian (ALE) method is introduced to rewrite the physics equations on a freely moving mesh.

To allow the moving boundaries, the Eulerian equations must be revised to describe all physical quantities as a function of some coordinate system in which the domain boundaries are fixed. Therefore, in COMSOL, to coordinate with ALE method,

the mesh coordinate is introduced and offered to represent such system. The domain is fixed in the mesh coordinate system, which is defined freely and separately from the spatial and material systems. There is a one-to-one mapping from the mesh coordinates to the current spatial configuration of the domain, while, initially, the mesh coordinate system is set to coincide with the geometry coordinates, i.e., points in the domain are identified by their position in the original geometry. As the domain and mesh deform due to the motion in the model, the mapping from the mesh coordinates to the spatial coordinates may become increasingly ill-conditioned, especially in narrow gap and highly unstructured domain. With remeshing operation, a new mesh can be created in the current configuration and all the quantities can be mapped to the new mesh scheme. When the simulation restarts, the points in the domain are internally identified by their new mesh coordinates, which coincide with the spatial coordinates at the state where the simulation is re-meshed. Thus, the geometry and mesh coordinates of a given point differ after remeshing the deformed geometry.

ALE, as an intermediate method between the Lagrangian and Eulerian method, does not require to match either the spatial or material frame and is taken to revise the position of the moving particles and modify mesh element at each time step. In the special case where the mapping from the mesh coordinates to the spatial coordinates follows the material deformation, the Lagrangian method is recovered. Similarly, when the mapping is an identity mapping, the ALE method becomes entirely Eulerian. Therefore, ALE combines the best features of both the Lagrangian and Eulerian methods and allows moving boundaries without the need for the mesh movement to follow the material, thereby enabling high accuracy of simulation. While at the same time, periodic

remapping of conserved physical quantities to mesh coordinate is required which is relatively computationally expensive.

5.7 Multiphysics Modules

A variety of predefined multiphysics modules from COMOSOL® are applied with a time-dependent fully coupled solver to solve the particle-field, particle-fluid and particle-particle interaction problem. The flow chart of the solution strategy is shown in in Figure 31.

With the applied external field, Electrostatics (es) or Magnetic, No currents (mnfc) module are first analyzed the distribution of electric field and magnetic field respectively. In the presence of the nonuniform electric/magnetic field, DEP/ MAP forces and torques are induced and calculated by integrating the Maxwell stress tensor over the surface of particles. The resulting forces and torque direct the particles to move and induce a flow in the suspended media where flow field is solved by the Laminar flow (spf) module. While at same time, the arbitrary Lagrangian-Eulerian (ALE) method coupled with Global ordinary differential equation are applied to update the spatial location of the moving particles. Subsequently, with the updated particle location, the electric/magnetic field is altered which triggers the Electrostatics (es) or Magnetic, No currents (mnfc) module for new position analysis.

The Electrostatics (es) module is utilized to compute the electric field, electric displacement field and potential distribution needed for the study of dielectrophoresis. When adding the Electrostatics (es) to model, the default user interfaces is Charge Conservation, Zero Charge (the default boundary condition) and Initial Value. Charge

Conservation is the main interfaces which adds the equation for charge conservation according to Gauss' law for the electric displacement field. It provides an interface for defining the constitutive relation and related properties, such as the relative permittivity. The Zero charge node adds the condition that there is zero charge on the boundary where $\vec{n} \cdot \vec{D} = 0$. The initial values node adds an initial value for the electric potential V that can serve as initial condition for a transient simulation or the nonlinear solver. Other interior and exterior boundary conditions including edge, point, and pair are also feasible.

For the simulation of magnetophoresis, the Magnetic, No currents (mnfc) module is applied to compute magnetostatic fields from permanent magnets and other current free magnetic sources which sovles Gauss' Law for magnetic field using the scalar magnetic potential ψ as the dependent variable. The default user interfaces are the Magnetic Flux conservation, Magnetic Insulation and Initial Values. The main user interface is the Magnetic Flux Conservation feature, which adds the equation for the magnetic potential and provides an interface for defining the material properties and the constitutive relation for the magnetic flux density. It is used when there are no currents and all the magnetic fields are originated by permanent magnets or external systems not included in the model. Magnetic Insulation as the default boundary condition, sets the normal component of magnetic flux density to zero, $\vec{n} \cdot \vec{B} = 0$. In the Initial Condition interface, an initial value for the magnetic scalar potential can be edited to serve as an initial value for the nonlinear solve. Other interfaces, such as magnetic scalar potential, external magnetic flux density is also available.

Under the single-phase flow branch, Laminar Flow (spf) module is applied to

compute the flow field. The laminar flow interface has the equations, boundary conditions, and volume forces for modeling freely moving fluid using the Navier-Stokes equations. Velocity field ($\vec{u}$) and Pressure (P) are defined as the dependent variables. The default user interfaces are the Fluid Properties, Initial Values and Wall (the default boundary condition is no slip). Fluid Properties is the main user interface in the module, at which the fluid material and its properties are defined for the Naiver-Stokes equations. The initial values serves as initial conditions for a transient simulation or for a nonlinear solver in a stationary simulation, which can specified the initial velocity field and pressure. The Wall node includes a set of boundary condition describing fluid-flow condition as stationary, moving and leaking wall where no slip is the default boundary condition to model solid walls. Other features, such as boundary condition and volume forces can also be implemented and edited.

The Moving Mesh (ale) module coupled with Global Ordinary Differential Equations and Differential Algebraic Equations (ge) module is used to update the spatial location of the moving particles and to monitor the instantaneous field distributions. The governing equations of particle motion (Eqs. (51) to (74)) are added in the Differential Equations and Differential Algebraic Equations (ge) module for simulation. Moving Mesh interface is used to specify stationary or transient deformation of the simulation domain. The default interface is Fixed mesh, which specify the selected domains remain at their reference material shape and do not move., and Prescribed mesh displacement where the deformation explicitly is defined by the input expression (default is no mesh displacement). Other interfaces, Free deformation which constrains the mesh displacement only by the boundary condition on the surrounding boundaries,

and Prescribed mesh velocity are also selected in this work.

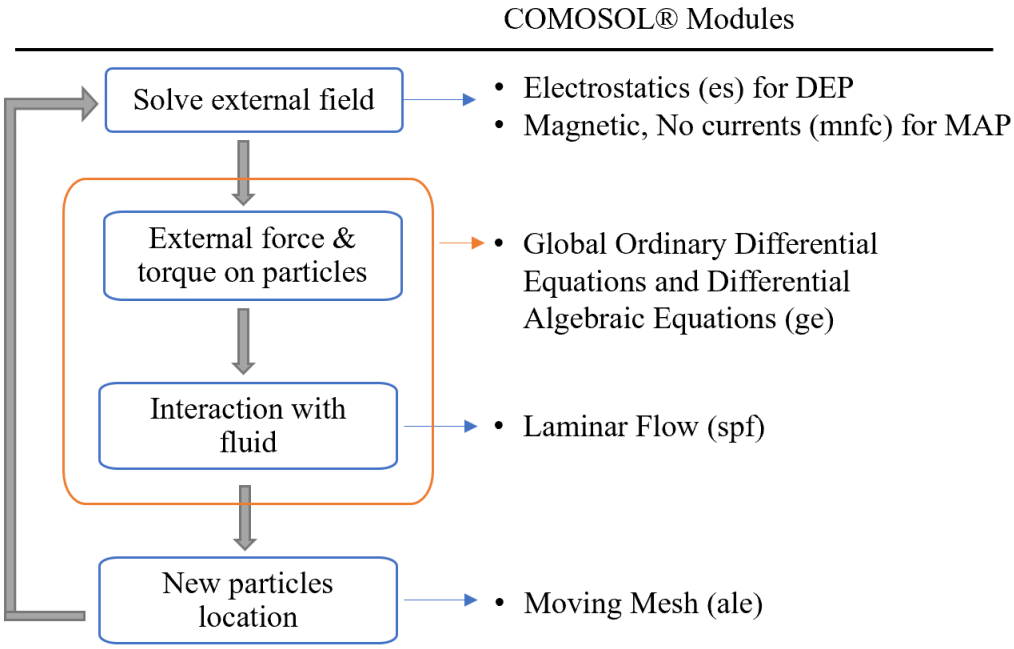

Figure 31 Diagram of simulation step with corresponding COMOSOL® modules.

5.8 Collision Model

An important issue in the particle interaction problem is the particle collision when two particles are moving very close to each other. To prevent the particles from penetrating, a collision model [129] is adopted to mitigate the mesh distortion in the near-collision region, while at the same time it preserves the total mass and momentum within the numerical truncation error.

In the collision model, a short-range repulsive force $\vec{F}_{r,i}$ is introduced and the particle equation of motion for i-th particle, Eq.(51) is to be replaced by

$$m_i \frac{d\vec{U}_i}{dt} = \sum_j \vec{F}_{i,j} = \vec{F}_{h,i} + \vec{F}_{DEP,i} + \vec{F}_{r,i}, \tag{62}$$

Where

$$\vec{F}_{r,i} = \sum_{j=1, j\neq i}^{N} \vec{F}_{i,j}^{R} \tag{63}$$

and

$$\vec{F}_{i,j}^{R} = \begin{cases} 0, & d_{i,j} > a_i + a_j + \rho \\ \frac{1}{\varepsilon}(\vec{x}_{c,i} - \vec{x}_{c,j})(a_i + a_j + \rho - d_{i,j}), & d_{i,j} \leq a_i + a_j + \rho \end{cases}, \tag{64}$$

In these equations, $\vec{F}_{r,i}$ is a short -range replusive force acting on the i-th particle by the other particles, $d_{i,j} = \left|\vec{x}_{c,i} - \vec{x}_{c,j}\right|$ is the distance between the center of i-th particle and j-th particle as showed in Figure 32, ρ is the force range and ε is a small positive stiffness parameter.

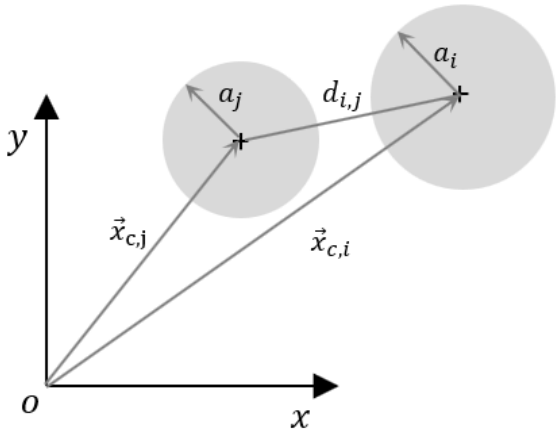

Figure 32 Schematic diagram of the particles in the domain as mentioned in the collision model.

Chapter 6. Numerical Study of Particle Motion under Dielectrophoresis

In this chapter, the pearl chaining process, where particles in a suspension are lined up along the direction of the applied electric field and form a one-dimensional (1D) chain lattice structure [130-132], is numerically simulated to better understand the particle-field-fluid interactions under the influence of dielectrophoresis. Pearl chaining is driven by the attractive DEP force between neighboring particles, which is short-ranged and decays rapidly as a function of R^{-4} where R is the inter-particle distance [133]. Thus, the morphological quality and stability of the 1D chain structure can be easily affected by disturbances in the surrounding fluid medium. Current understanding of the pearl chaining process is restricted primarily to the electrostatic aspect of the particle-particle interactions, whereas the fluid-particle hydrodynamic interactions and their impact on the assembly of 1D chain lattice have been largely neglected. Hence, this chapter aims to fill the present gap between the basic knowledge of pearl chaining and future technological development of DEP directed self-assembly of micro/nanoparticles.

In this study, the ALE method, coupled with the MST approach, is employed to explore the mechanism and process of DEP directed pearl chaining under an uniform electric field applied externally.

6.1 Dielectrophoretic Motion of Two Particles

6.1.1 Model Setup

A model system is set up to elucidate the pearl chaining process of two particles. As shown in Figure 33, it consists of a pair of two spherical particles of radius a, P_1 and P_2, suspended in an incompressible and Newtonian fluid of a size $L \times L$. The intitial inter-particle distance is R. A uniform electric field $\vec{E}$ is applied along the y-direction with the electrostatic potentials being $\phi = \phi_1$ on AB and $\phi = \phi_2$ on CD. The angle between the electric field and the line connecting the centers of the particles is θ. After the electric field is actuated, the two paricles will experience DEP forces and tend to align with the applied field.

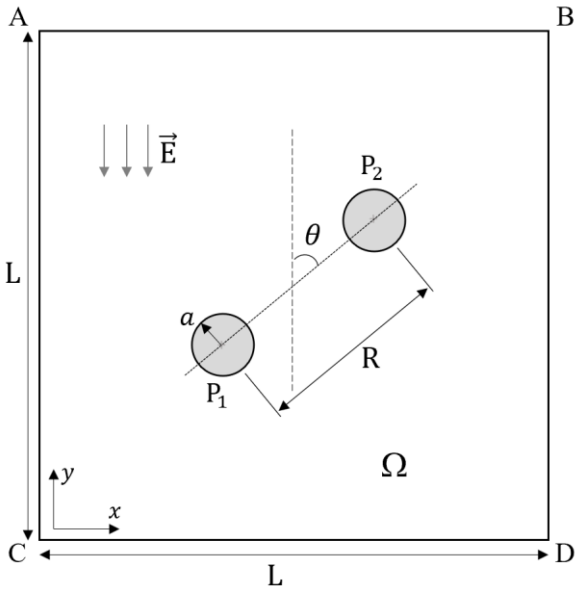

Figure 33 Scheme of simulation domain with two particles under a uniform field

6.1.2 Theoretical Considerations

Some theoretical considerations regarding the relative motion of two interacting identical particles and the Brownian motion of small particles are first discussed in this

subsection to facilitate the understanding of the numerical results that will be presented later.

6.1.2.1 Relative Motion of Interacting Identical Particles

The dielectric force induced by DEP on the particle pair in Figure 33 is derived by Kwan et al. [134]

$$\vec{F}_{DEP} \cong -\frac{6\pi\varepsilon_0\varepsilon E_\infty^2 a^2}{\left(\frac{R}{a}\right)^4}\left[\hat{\vec{i}}\left(cos^2\,\theta - \frac{1}{2}sin^2\,\theta\right) + \hat{\vec{j}}\,sin\,\theta\,cos\,\theta\right], \tag{65}$$

where E_∞ is the applied electric field, ε is the permittivity, $\hat{\vec{i}}$ is the unit vector in the x-direction, $\hat{\vec{j}}$ is the unit vector in the y-direction, ε is the relative permittivity and ε_0 is the Permittivity of vacuum. When the particle moves in the fluid medium, it also experiences the viscous Stokes' drag force. Assuming the particles are under quasi-equilibrium, the dielectric force is balanced by the Stokes' drag, which yields an instantaneous particle velocity

$$\vec{u} = \frac{\vec{F}_{DEP}}{6\pi\mu a} = \cong -\frac{\varepsilon_0\varepsilon E_\infty^2 a}{\mu\left(\frac{R}{a}\right)^4}\left[\hat{\vec{i}}\left(cos^2\,\theta - \frac{1}{2}sin^2\,\theta\right) + \hat{\vec{j}}\,sin\,\theta\,cos\,\theta\right], \tag{66}$$

where μ is the fluid viscosity. The velocity can be presented in the dimensionless form with $R^* = R/a$

$$\vec{u}^* \equiv \frac{\vec{u}}{\frac{\varepsilon_0\varepsilon E_\infty^2 a}{\mu}} = -\frac{1}{(R^*)^4}\left[\hat{\vec{i}}\left(cos^2\,\theta - \frac{1}{2}sin^2\,\theta\right) + \hat{\vec{j}}sin\theta cos\theta\right]. \tag{67}$$

Hence, the following equations in a (R, θ) polar coordinate system is obtained

$$\frac{dR^*}{dt^*} = -\frac{2\cos^2\theta - \sin^2\theta}{R^{*4}} \tag{68}$$

and

$$\frac{d\theta}{dt^*} = -\frac{2\sin\theta\cos\theta}{R^{*5}}, \tag{69}$$

where the dimensionless time is $t^* = \frac{t}{\frac{\mu}{\varepsilon E_\infty^2}}$.

Equations (65), (68)and (69)can be used to describe the relative motion of the particle pair qualitatively. According to Eq.(69), if the initial angle θ falls into the range $0 < \theta < \frac{\pi}{2}$, the RHS is always negative, meaning that θ should decrease toward zero and the particle pair tends to align along the direction of the electric field. Additionally, when $\vec{F}_{DEP}$ in Eq. (65) is projected along the R-direction, the sign of this component will change when θ crosses over the threshold value determined by

$$\left(\cos^2\theta - \frac{1}{2}\sin^2\theta\right)\sin\theta + \sin\theta\cos\theta\cos\theta = 0, \tag{70}$$

which yields $\theta_{c,1} = 63.4°$. For instance, as will be shown later, a pair of particles initially oriented at $\theta = 80°$ and experiencing repulsive DEP forces starts to attract each other as θ decreases to $63.4°$. The variation of the interparticle distance R lags slightly behind $\vec{F}_{DEP}$. When the right side of Eq.(69) becomes zero, i.e., $\theta_{c,2} = 54.7°$, the sign of $\frac{dR^*}{dt^*}$ starts to change from positive to negative. Thus, for the same pair of particles that are oriented with θ, the distance between them first increase and then decrease. Overall, it is expected that when any two particles are moving from $\theta = \frac{\pi}{2}$ to $\theta = 0$, they are repelled at first due to the repulsive DEP force. When θ reahes $\theta_{c,1}$, the DEP force changes the direction to an attractive force. As θ continually decreases to $\theta_{c,2}$, the

particles will attract to each other and the self-assembly process begins till a particle chain is formed.

6.1.2.2 Brownian Motion of Small Particles

When considering the particle-fluid interactions, the impact of Brownian motion, which arises from the random bombardment of solvent molecules on the particle, must be carefully addressed, especially for nanometer-sized particles. The importance of Brownian motion with respect to the DEP motion can be evaluated by the Péclet number [135]

$$Pe = \frac{aU}{D_f}, \tag{71}$$

where a is the particle radius, U is the local particle velocity and D is the applied electric field, the DEP force inserting on the each of particles can be estimated as [134]

$$F_{DEP} = \frac{3\pi\varepsilon_0\varepsilon_m E^2 a^2}{(R/a)^4}, \tag{72}$$

Where ε_m is the permittivity of the fluid, E is the electric field, R is the distance of center to center of particles. As the particle velocity for DEP particles manipulation which is obtained from $\vec{u} = \frac{\vec{F}_{DEP}}{6\pi\mu a}$, and the Brownian motion diffusion coefficient is given as $D_f = \frac{KT}{3\pi\mu a}$, the Peclet number, Eq. (71), can be rederived to

$$Pe = \frac{3\pi\varepsilon_0\varepsilon_m E^2 a^3}{2KT(R/a)^4}, \tag{73}$$

where K and T are the Boltzmann constant ($K = 1.38 \times 10^{-23} J \cdot K^{-1}$) and the temperature respectively, and μ is the fluid viscosity.

As $Pe = \frac{aU}{D_f} = \frac{a^2/D_f}{a/U} = \frac{t_{diff}}{t_{DEP}}$, the Péclet number can be interpreted as the ratio of time that is needed for the particle to travel a distance of *a* due to Brownian motion and DEP, respectively [136]. Therefore, when Pe >> 1, the effect of Brownian motion can be safely neglected; otherwise, it must be taken into consideration in the DEP-directed self-assembly process. The typical values used in this work are $E = 500\ \mathrm{kV}/m$, $a = 10\ \mu\mathrm{m}$, $\varepsilon_0 = 8.85 \times 10^{-12}\ F/m$, $\varepsilon_m = 1$ and $T = 300\ K$, $Pe = 31075 \gg 1$ with $R = 30\ \mu\mathrm{m}$. Therefore, the effect of Brownian motion can be safely neglected.

6.1.3 Numerical Results and Discussion

Numerical simulations were performed for the particle-fluid system with different initial configurations to obtain the particle trajectories during the DEP-directed fluidic assembly process. In the simulations presented here, the material property is indicated in Table 2. The particle radius is $a = 10\ \mu\mathrm{m}$ and the initial center-center distance between the particles is set to be $R = 30\mu\mathrm{m}$. The domain length is set to be $L = 200\mu\mathrm{m}$, which is 20 times the particle size in order to eliminate the boundary effect on the particle motion. The electric field is defined with electrostatic potentials on the domain boundaries: $\phi_{AB} = 100\ \mathrm{V}$ and $\phi_{CD} = 0\ \mathrm{V}$. In the flow problem, no slip boundary conditions are specified on Boundaries AB and CD and the particle surface, and inlet and outlet pressure conditions are set on Boundaries AC and BD.

Table 2 Material Property of Identical Particles in DEP.

Parameter	Definition	Value
ε_0	Permittivity of vacuum	$8.85 \times 10^{-5}\ F/m$
ε_m	Relative permittivity of fluid	1
ε_p	Relative permittivity of particle	100
μ	Fluid dynamic viscosity	1×10^{-3} Pa · S
ρ_m	Fluid density	1×10^{3} Kg/m^3
ρ_p	Particle density	1×10^{3} Kg/m^3

Configuration 1

In the first configuration, a pair of stationary particles are initially positioned at $(\mathrm{x}, \mathrm{y}) = (0, \pm 15\mu\mathrm{m})$ with $\theta = 0°$, as shown in Figure 34(a). After the external field is applied, the two particles are attracted to move toward each other and eventually form a chain structure along the direction of the electric field (Figure 34 (b)).

To illustrate the relative motion, the y-component velocity of the two particles is shown in Figure 35 (a). It is found that the particles always move at the same speed but with opposite directions. As the two particles are approaching, the particle velocity first increases as the attractive DEP force is inversely proportional to the forth power of the center-to-center distance between the particles (Eq. (72)). However, the particle velocity then start to decrease because the viscous drag force and the repulsive pressure force increases rapidly to resist the motion of attraction. When the interparticle distance R reduces to 1μm, the collision model as mentioned before, is activated to prevent penetration of the particles. To do so, a repulsive force $\vec{F}_{i,j}^{R}$ where $\vec{F}_{i,j}^{R} = \frac{1}{\varepsilon}(\vec{x}_{c,i} - \vec{x}_{c,j})(a_i + a_j + \rho - d_{i,j})$ is enforced on each of the two particles [129], where the force range ρ is set to be $\rho = \frac{1}{10}a = 1\mu m$, small positive stiffness parameter. $\varepsilon = 1e - 16$, with the consideration of particle size and the limitation of computational power. As

indicated in Eq. (62), with both the DEP force, hydrodynamic forces and the repulsive force presented at the last stage, particles are eventually paired and aligned along the applied field.

The velocity profile in Figure 35 (b) indicates that the fluid between the two particles is flowing outward as being squeezed by the head-to-head motion of the particles whereas the fluid is replenished through Boundaries AB and CD. Overall, the velocity field is symmetric about the x-axis due to the initial configuration of the system.

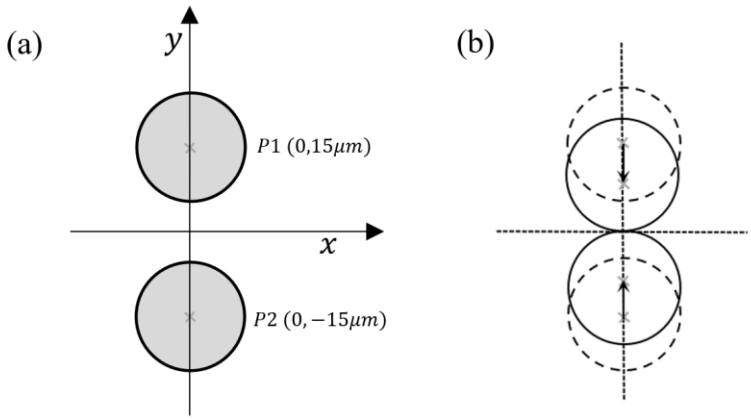

Figure 34 (a) Particle configuration (b) trajectories of two particles with $\theta = 0°$respectively (initial position and final position are indicated by dash line and solid line respectively.)

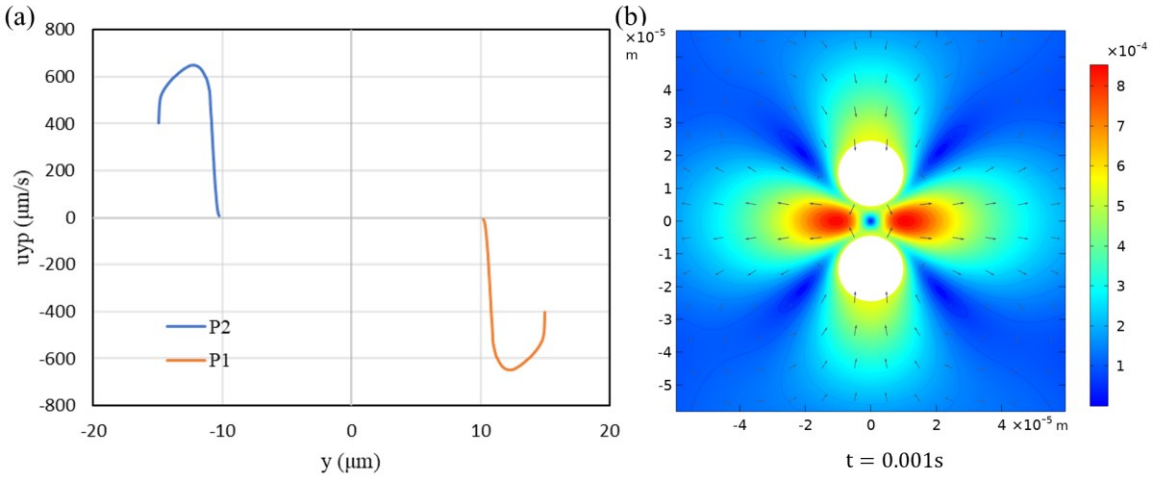

Figure 35 (a) Velocity of pair of particles originally position at $(x, y) = (0, \pm 15\mu m)$ with changing of position, (b) velocity contour when $t = 0.001s$.

Configuration 2

In the second configuration, the particles are arranged with the centerline perpendicular to the electric field, i.e., the particles are located at $(x, y) = (\pm\ 15\ \mu m, 0)$ and $\theta = 90°$, as shown in Figure 36 (a). When the electric field is applied, the instantaneous DEP force is repulsive which repels the two particles away from each other. The particle trajectory is shown schematically in Figure 36 (b). Relative motion between the particles along the *x*-direction is illustrated in Figure 37 (a). As the two particles start moving, the particle velocity increase. Shortly, the velocity decrease since the repulsive DEP force decreases rapidly as an inverse proportion to the forth power of the interparticle distance. The velocity profile in Figure 37 (b) shows that the fluid between the two particles is flowing inward and "pushing" the particle move away from each other. Similar to Configuration 1, the velocity field is symmetric about the y-axis due to the initial configuration of the system.

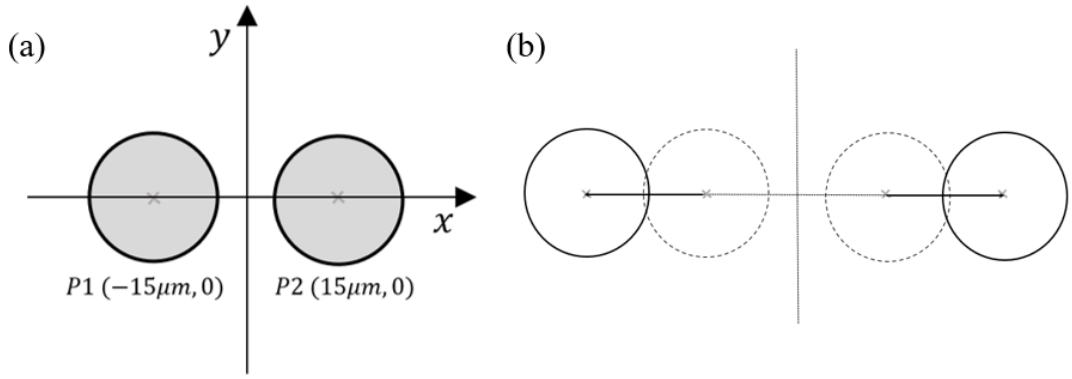

Figure 36. (a) Particle configuration (b) trajectories of two particles with θ = 90°respectively (initial position and final position are indicated by dash line and solid line respectively.).

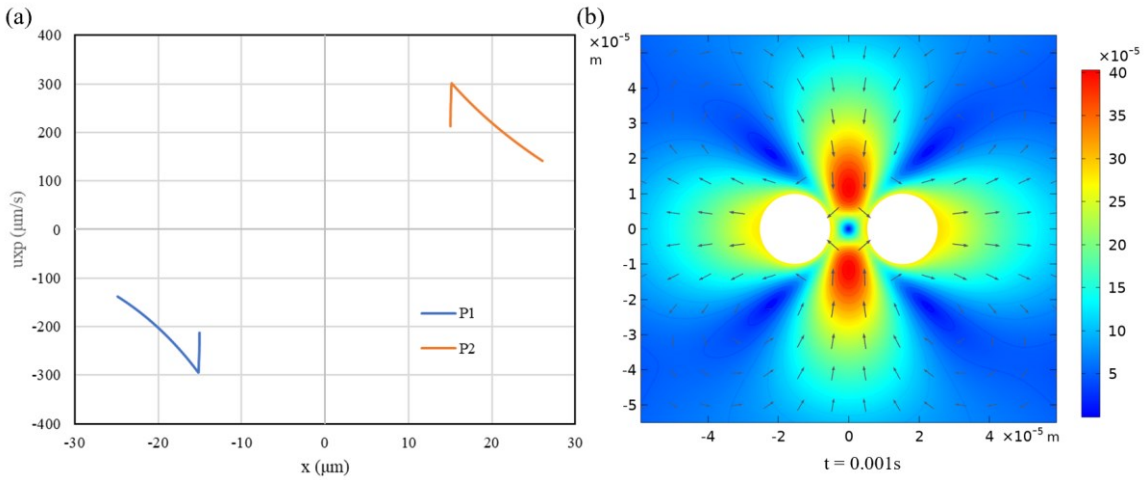

Figure 37. (a) Velocity of pair of particles originally position at $(x, y) = (\pm 15\mu m, 0)$ with changing of position, (b) velocity contour when $t = 0.001s$.

The numerically computed x-component of the DEP force is compared with the analytical result from Eq. (65) in Figure 38. At large values of R, the analytical model provides very good prediction of the DEP force. However, when R is relatively small, the distortion of the local electric field is no longer negligible and the analytical model overpredicts the DEP force. Thus, certain care should be exercised when applying Eq. (65) to study particle interactions under the influence of DEP.

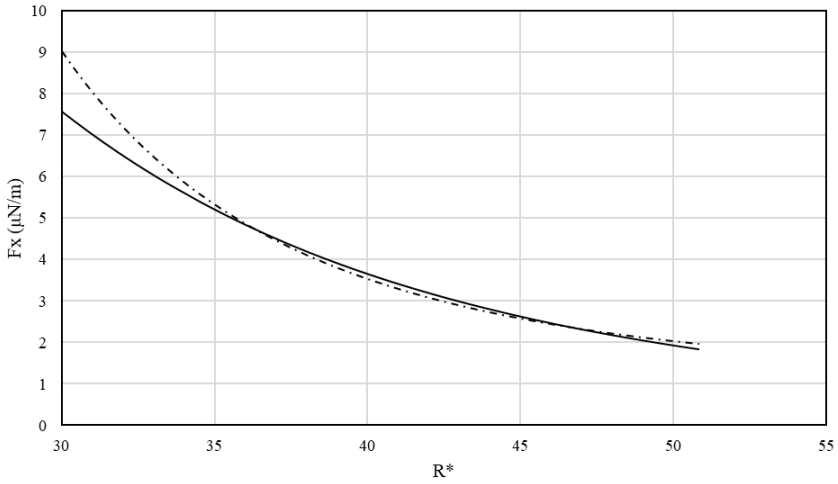

Figure 38 DEP force of particle located at $(x, y) = (\pm 15\mu m, 0)$ derived from MTS method and the relation to the 1/R4, while numerical result and analytical result are in solid line and dash line respectively.

Configuration 3

Configurations 1 and 2 deal with two specific orientations of the particle pair with respect to the applied electric field, one in parallel and one perpendicular. The more general cases are studied in the third configuration, where the initial angle between the centerline of the particle pair and the field θ is chosen to be 30°, 60°, and 80°, as shown in Figure 39 (a)-(c). In general, the simulation results agree with the prediction by Eq.(69), i.e., θ decreases as the two particles align with the electric field. More details of the particle motion will be discussed in the following.

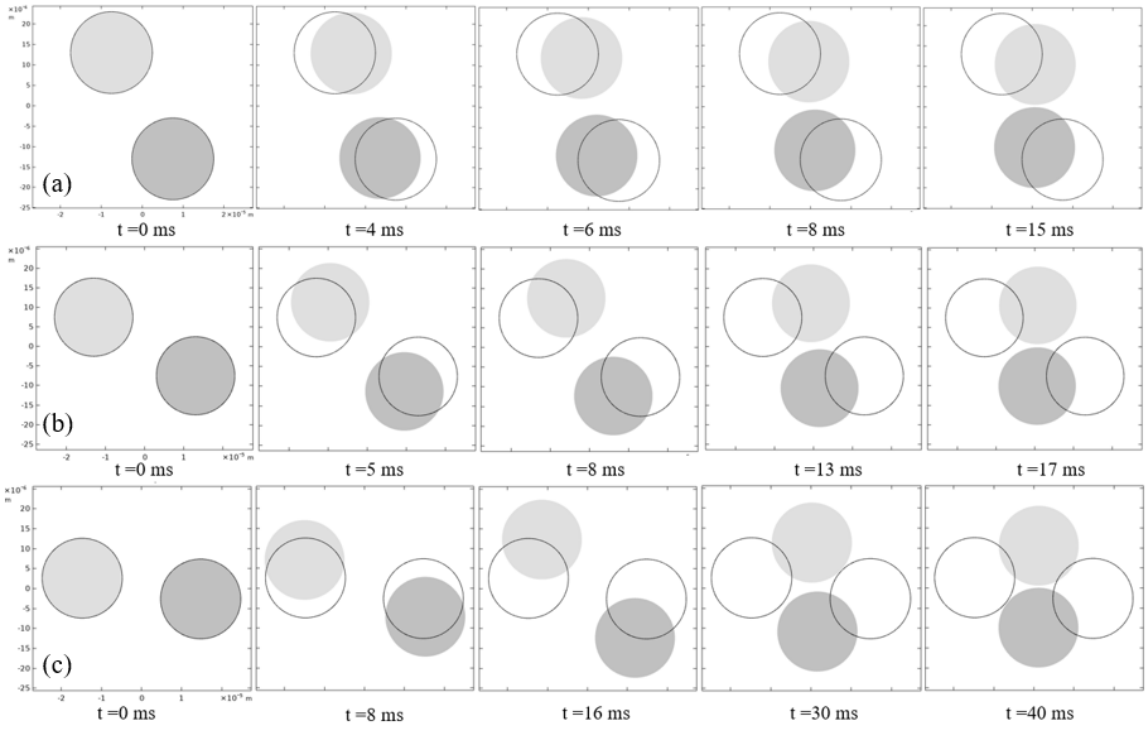

Figure 39 Motion of pair of particles initially located at $\theta = 30°$, $\theta = 60°$, $\theta = 80°$ with $R = 30\mu m$ in (a), (b), and (c) respectively.

For an initial angle $\theta = 30°$, the particles are rotating clockwise and moving closer to each other, as shown in Figure 40 (a). The trajectories of the centers of the two particles are mapped in Figure 40 (b). With the impact of the induced DEP force, the

particles rotate around the origin with a monotonously decreasing θ. In the meanwhile, the center-to-center distance decreases until the particles get into contact with each other.

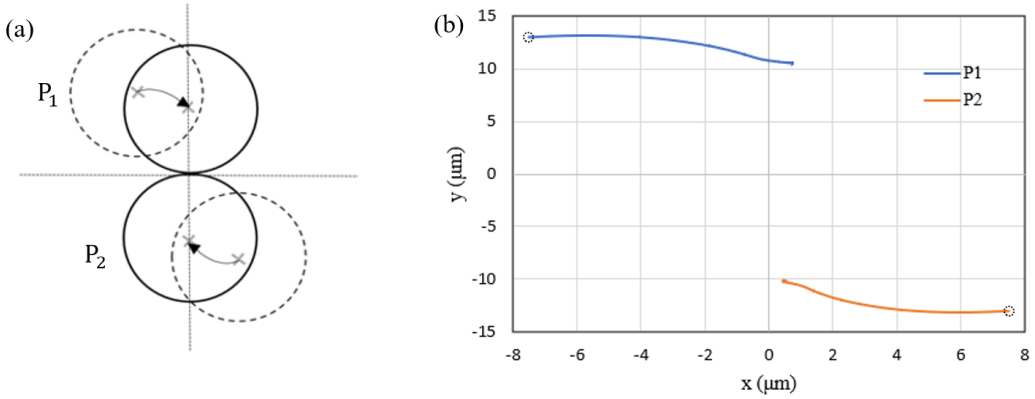

Figure 40 Pair of particles initially located at $(x, y) = (\mp 7.5\mu m, \pm 13\mu m)$ With $R = 30\mu m$, $\theta = 30°$ (a) particle trajectories, (b) relative motion trajectories of a pair of particles (dash line indicated the initial position).

When the particles are initially located at $\theta = 60°$, the particles undergo a more complex motion. As shown in Figure 41 (a), they slightly repel each other in the very beginning. With the constant attractive DEP, which indicated in Figure 41 (b), while F_{DEP} in x and y direction are both in positive direction for P_1 in the beginning, the center-to-center distance between the pair of particles R starts to decrease as particles moving toward to each other once the instantaneous angle crosses $\theta = 53.7°$ which is comparable with θ_c,

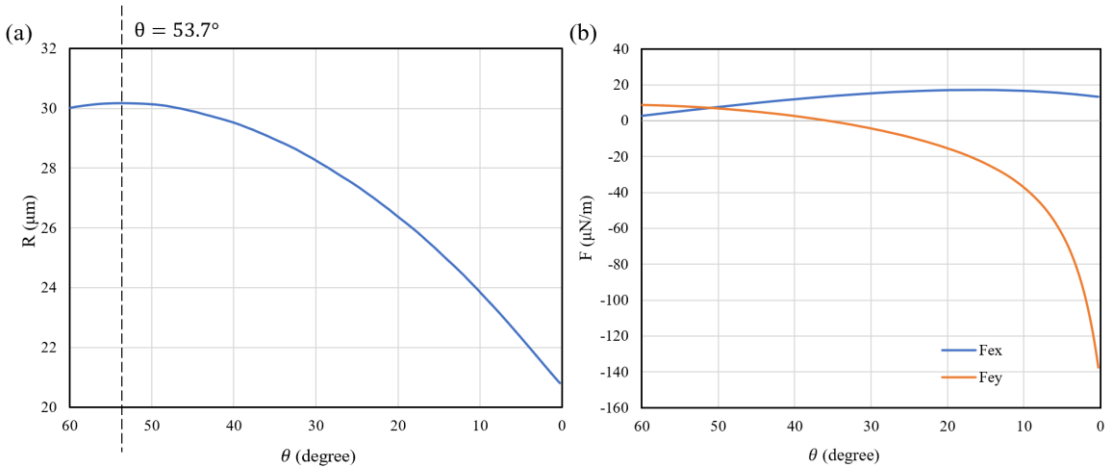

Figure 41 Pair of particles initially located at $(x, y) = (\mp 13\ \mu m, \pm 7.5\ \mu m)$ With $R = 30\ \mu m$, $\theta = 60°$,(a) R with the relation to θ (b) DEP force for P_1.

For an ever larger initial angle θ=80°, the particle trajectories are depicted in Figure 42 (a). It shows more clearly that the particles initially repel each other with the repulsive DEP force, but gradually draw closer as they revolve in the clockwise direction and, finally, they align with the y-direction. The interparticle distance R is shown in Figure 42 (b) as a function of the instantaneous angle θ. The same trend is found: R increases at first because the DEP force between the two particles is repulsive. As indicated in Figure 43, where F_{DEP} on particle P_1 is negative in the x direction and positive in the y direction, thus causing θ to decrease. When θ decreases to 63.9° (this value is comparable with the theoretical solution $\theta_{c,1} = 63.4°$), the sign of F_{DEP} in the x direction changes to positive and an attractive force is exerted on the particle. Due to the lag between the particle acceleration and velocity, R does not decrease immediately. Instead, it reaches the maximum at 52.4° (near the theoretical prediction $\theta_{c,2} = 54.7°$) and, then, gradually decreases till the two particles touch each other, as shown in Figure 42 (b). The difference in the critical values θ between the numerical solution and theoretical prediction is because a uniform electric field E_∞ is considered in the

theoretical model whereas. in reality, the local electric field is distorted by the presence of the two particles.

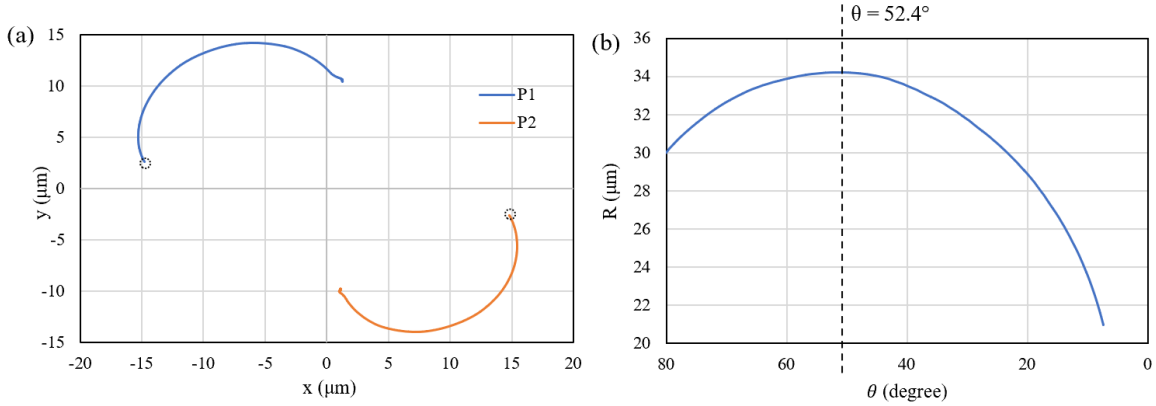

Figure 42 Pair of particles initially located at $(x, y) = (\mp 14.77\mu m, \pm 2.6\mu m)$ With $R = 30\mu m$, $\theta = 80°$,(a) relative motion trajectories of a pair of particles, (b) R with the relation to θ

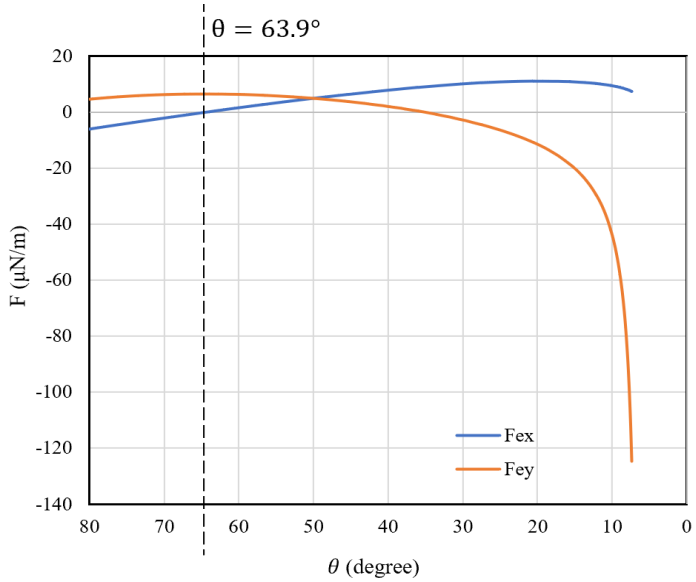

Figure 43 DEP force for P_1 with initial position with $\theta = 80°$

6.2 Dielectrophoretic Motion of Three Particles

Previous studies of DEP-directed assembly of micro/nanoparticles have focused primarily on the experimental aspect of the final patterns formed by the particles [137]. In this section, the simulation results involving the DEP motion of three particles will

be discussed to offer some insight into the dynamics of the DEP directed particle assembly, especially on the interparticle interactions and the particle trajectory during the assembly process.

Three-body problem, in which the motion of three point masses needs to be solved for given initial positions and velocities in the framework of Newtonian mechanics, is notoriously complex due to its sensitivity to the initial conditions and, generally, requires numerical solutions. In this work, three particles randomly located as the configuration shown in Figure 44 (a) is considered. The distance between the centers of the particles are $R_{12} = 37.35\ \mu m$, $R_{23} = 30.92\ \mu m$ and $R_{13} = 63.78\ \mu m$, while $\theta_{12} = 27.94°, \theta_{13} = 9.02°$ and $\theta_{23} = 14.04°$, where θ_{ij} is the angle between the direction of applied field and the centerline R_{ij} connecting particles i and j. As discussed in the foregoing sections, the dielectric force between any two identical particles can be reasonably approximated by Eq. (65) as far as the interparticle distance is sufficiently large. Using this equation for a three-particle system, Kang and Suh [120] found that the DEP-induced motion of the system depends on the relative magnitude of the projected distance between any two particles on the direction perpendicular to the applied electric field. If two particles are initially located at a closer projected distance, they will become paired first and the third particle will react to the two-particle entity. For the configuration in Figure 44 (a), the projected distance between the particles x_{ij} can be calculated from $x_{ij} = R_{ij}\, sin(\theta_{ij})$ and it is easy to show $x_{13} = 10\ \mu m$, $x_{23} = 7.5\ \mu m$ and $x_{12} = 17.5\ \mu m$. Thus, it is expected that, at least qualitatively, particles P_2 and P_3 will pair up first and then P_1 will join.

The simulation results are shown in Figure 44 (b) and (c). Indeed, particles P_2

and P_3 are first moving toward each other, and P_1 revolves in the counterclockwise direction before approaching P_2 and P_3. At t = 14.9 ms, P_2 and P_3 become a pair and then they act as one body which eventually attracts P_1 to form a three-particle pearl chain structure. The results are thus consistent with the predictions by Kang and Suh's model. However, in a slightly different configuration where one particle is located at a relatively large distance from the other two particles ($R'_{12} = 37.35\,\mu m$, $R'_{23} = 67.42\,\mu m$ and $R_{13} = 100.5\,\mu m$) while maintaining the same projected interparticle distances, as shown in Figure 45, P_2 will be attracted to P_1 first before P_3 is drawn to join the pearl chain. Therefore, Kang and Suh's model should be applied with caution in predicting the dynamics of DEP-driven fluidic assembly of particles.

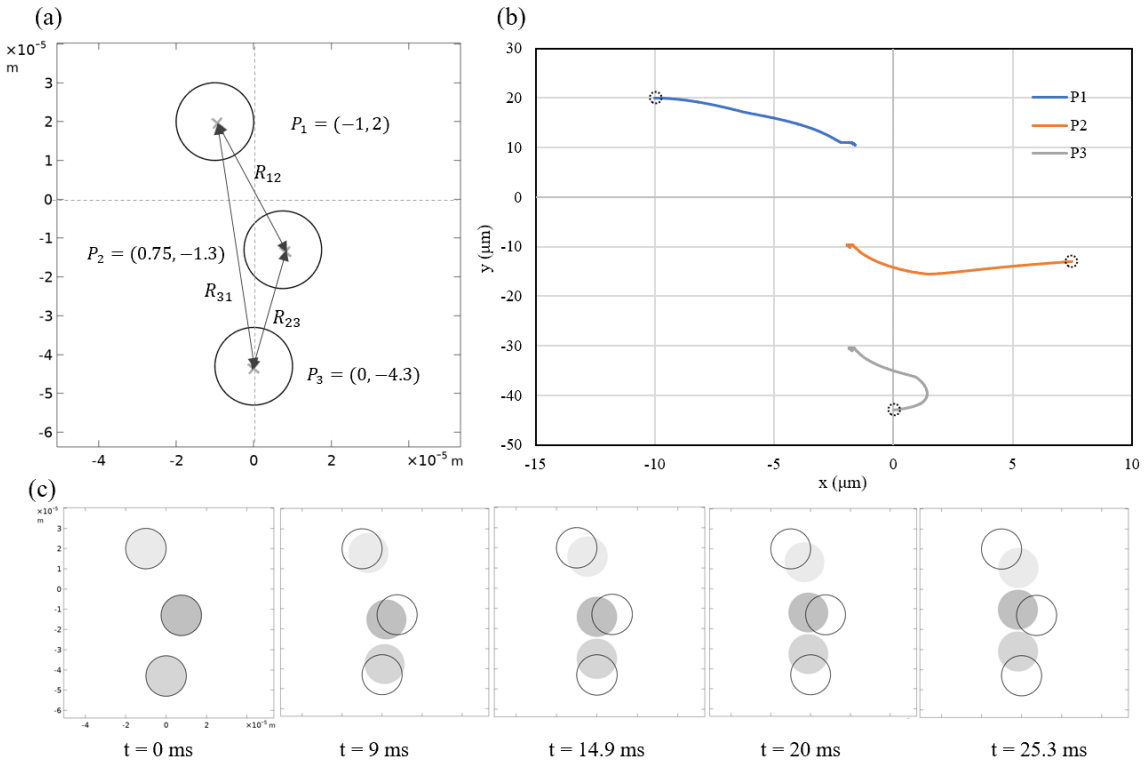

Figure 44 Three particles P_1 (-10 μm,20 μm) , P_2 (7.5μ m, -13 μm) and P_3 (0 μm, - 43 μm) (a) scheme of simulation domain, (b) relative motion trajectory of three particles (dash line indicate the initial position), (c) motion of particles.

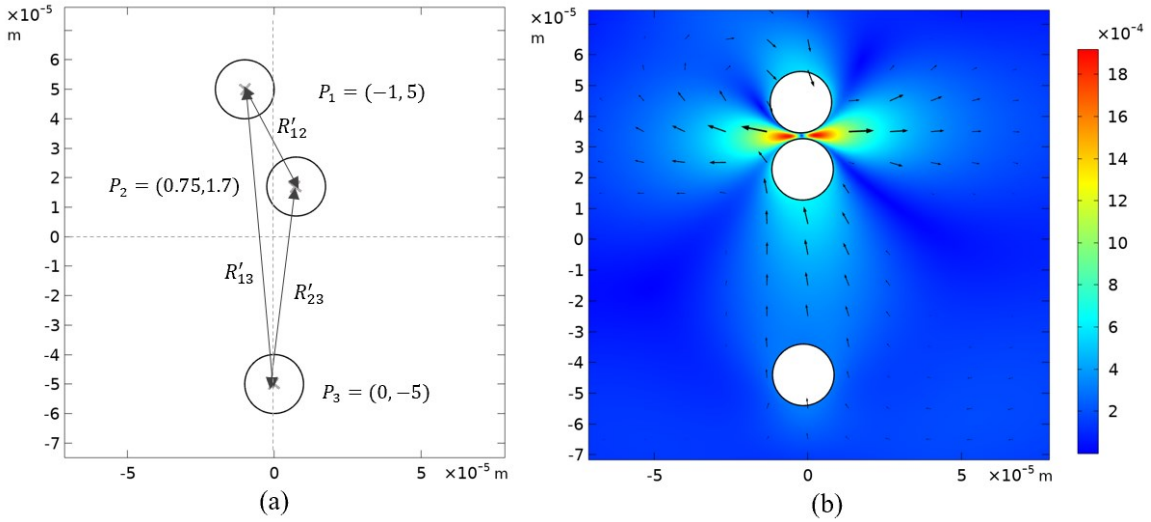

Figure 45 Three particles P_1 $(-10\mu m, 50\mu m)$, P_2(7.5μm, 17 μm) and P_3 (0μm, -50 μm), (a) scheme of simulation domain, (b) velocity of particles when t = 33.4ms.

6.3 Dielectrophoretic Motion of Five Particles

In practice, DEP-driven particle assembly involves numerous particles. After some basic understandings have been obtained, a system of five identical particles is investigated in this section to mimic the actual pearl chaining process.

Before the application of the electric field, five particles, P_1, P_2, P_3, P_4 and P_5, are positioned randomly in the fluid domain, as shown in Figure 46 (a). The particles start to move at t=0 ms when the external field is applied. P_3 and P_4 exhibit the strongest interactions by pairing up very rapidly (at t=11 ms), since the interparticle distance between them is the shortest. Once P_3 and P_4 paired, two particles acted as one body rest in the relatively static position, while other particles P_2, P_1 and P_5 are attracting to join the group consequently as indicated in Figure 47 (b). Finally, all the particles are aligned along the axis which is parallel to the direction of applied field. Instead all the particles in the case of five particles are split and clustered into two groups of three and

two particles indicated by Kang and Suh [120], particles tend to align and form the group one by one according the interpaticle distance.

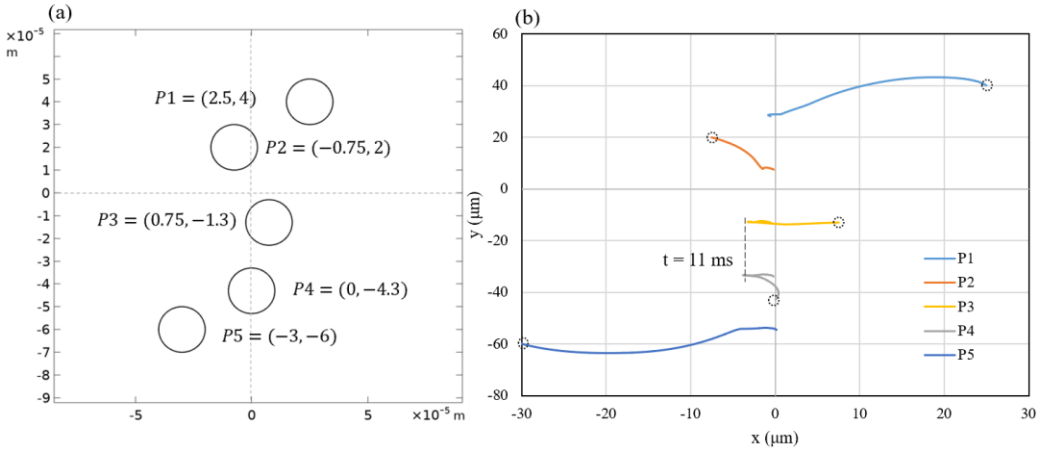

Figure 46 (a) Configuration of simulation domain, (b) relative motion trajectory of five particles (the initial position of particle is indicated in dash line circle)

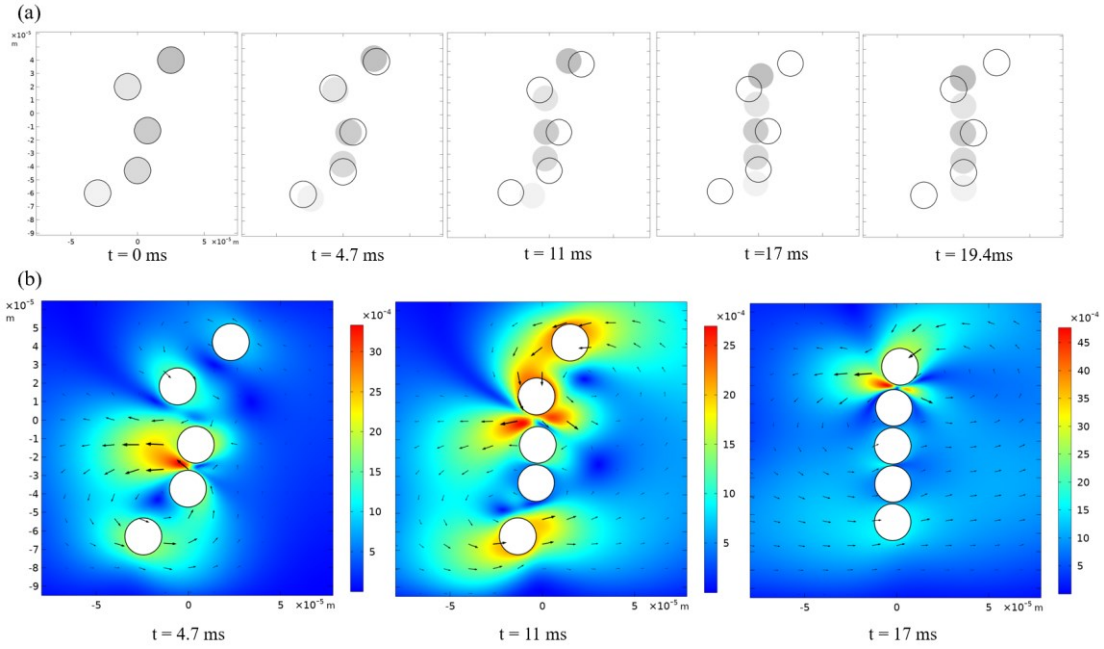

Figure 47 (a) Motion of particles (b) the velocity profile at t = 4.7 ms, t = 11 ms and t =17 ms.

6.4 Conclusion

In this chapter, the motion of DEP-driven assembly of particles are studied numerically. The particle assembly process is simulated, which offers detailed

information of the resilent features of the pearl chain pattern formation as well as the trajectory of the particle motion. The key findings include: 1) with the induced DEP, particles attract to each other if $\theta<63.4°$and symmetrically move toward to pair along the external field once $\theta<54.7°$, 2) The interparticle interactions and the particle trajectory of multiple particles during the assembly process is highly related to the initial configuration of the system, while eventually, identical particles always line to the chain along the electric field.

Chapter 7. Numerical Study of Dielectrophoretic Motion of Dissimilar Particles

The previous chapter is devoted to the study of DEP-induced fluidic assembly of particles into pearl chain structures. The mutual dielectrophoretic forces always drive the identical particles to pair up and align along the applied electric field, no matter if the individual particles experience positive or negative DEP [138,139]. When dissimilar particles (i.e., some particles have higher whereas the rest have a lower relative permittivity than that of the fluid medium) are present, the electric field around the particles is distorted which generates a different electric field intensity in the vicinity of each particle. In this chapter, numerical investigation will be performed to investigate the DEP-induced pattern formation of dissimilar particles with a focus on the difference in the particle-field-fluid interactions from that of identical particles.

7.1 Dielectrophoresis of Dissimilar Particles

The dielectric properties of the particle and the surround fluid medium, especially the relative permittivities (also called dielectric constants), ε_p and ε_m, have a major impact on dielectrophoresis, which originates from the charge redistribution in the particle when an external electric field is applied. The particle with a larger permittivity ($\varepsilon_p > \varepsilon_m$) is more polarizable than the fluid medium. Thus, as shown in Figure 48 (a), more charges accumulate on the particle side of the fluid-particle interface and the induced dipole moment aligns itself with the applied field. In the meanwhile, the polarization-induced internal field weakens the applied field, leading to less dense

field lines inside the particle. If $\varepsilon_p < \varepsilon_m$, the particle is less polarized. The induced dipole moment points opposite to the applied field, and the internal electric field will be intensified inside particle, as shown in Figure 48 (b). Accordingly, the two different type of particles will exhibit different dielectrophoretic behaviors in a non-uniform electric field.

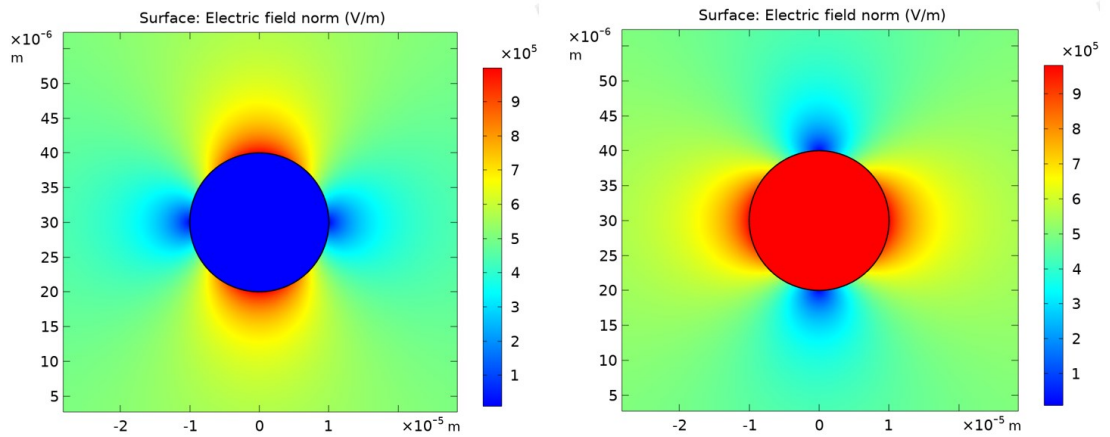

(a) (b)

Figure 48 Electric field in a uniform electric field with (a) $\varepsilon_p > \varepsilon_m$, (b) $\varepsilon_p < \varepsilon_m$

The DEP force experienced by the particle is given by

$$\vec{F}_{DEP} = 2\pi a^3 \varepsilon_m K(\varepsilon_p, \varepsilon_m) \nabla E^2, \tag{74}$$

where the Clausius-Mossotti (CM) factor is $K \equiv \left(\frac{\varepsilon_p - \varepsilon_m}{\varepsilon_p + 2\varepsilon_m}\right)$. Clearly, K controls the direction of the DEP force with respect to the external field. When the particle is more polarizable than the fluid domain ($\varepsilon_p > \varepsilon_m$ and $K > 0$) the particle will be driven toward the region of higher electric field gradient (i.e., the field maxima), a process termed "positive DEP" (pDEP). This is shown in Figure 49(a) and (b), where the electric field is created by placing a positive point charge over a negatively charged bottom plate and the direction of the velocity vectors in the fluid medium indicates the

direction of the particle motion. When the particle is less polarizable than the fluid ($\varepsilon_p < \varepsilon_m$ and $K < 0$), the particle is repelled from the field maxima by the negative DEP (nDEP) force, as indicated by Figure 49 (c) and (d).

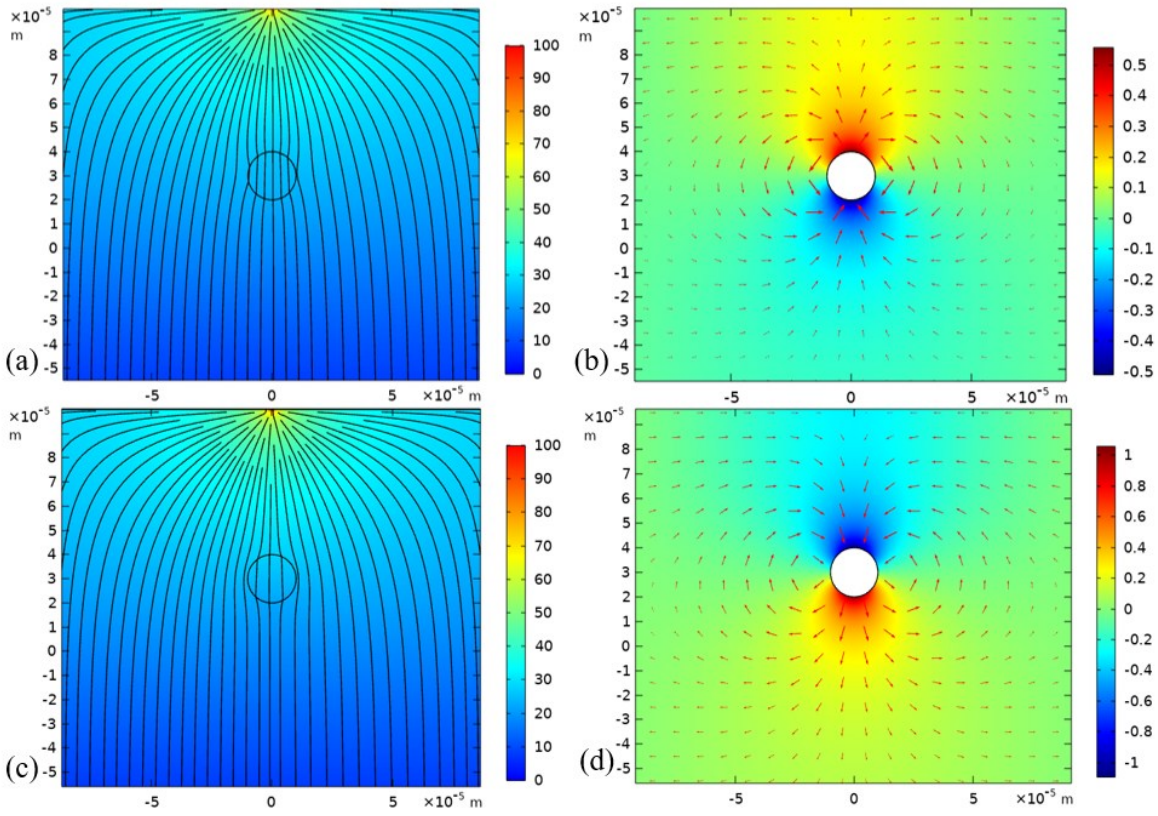

Figure 49 Positive DEP distribution of a) electric potential, b) fluid pressure/velocity field; negative DEP distribution of c) electric potential, d) fluid pressure/velocity field.

Figure 50 shows the electric field simulated for two pairs of identical particles that undergo pDEP ($\varepsilon_p = 150$ vs. $\varepsilon_m = 100$) and nDEP ($\varepsilon_p = 50$ vs. $\varepsilon_m = 100$), respectively. For the pDEP particle, the field maxima are found to be near its north and south poles (marked by brighter color) while the field minima are around its tropics (marked by darker color). Further, it is seen that the global field maxima exist in the space between the two pDEP particles. The situations are just opposite for the nDEP particle. Subsequently, the pDEP particles will be attracted to the global maxima

(Figure 50.(a)), i.e., they move closer to each other, and the nDEP particles will be expelled to the global minima (Figure 50 (b)), i.e., they also move toward each other. Therefore, although the electric field distributions are drastically different for nDEP and pDEP particles, the particle motion is the same in both cases since the particles are identical (similar) in each pair. In both cases, particles will pair and align along the direction of applied field, while for multiple particles, chain will form. However, in the presence of dissimilar particles, some present as pDEP and some are nDEP, different electric field intensity in the vicinity of each particles are generated due to the distorted electric field, where the assembly process will be distinct from the identical particles. To further investigate the dynamics of the dissimilar particle self-assembly process, numerical simulations are then performed.

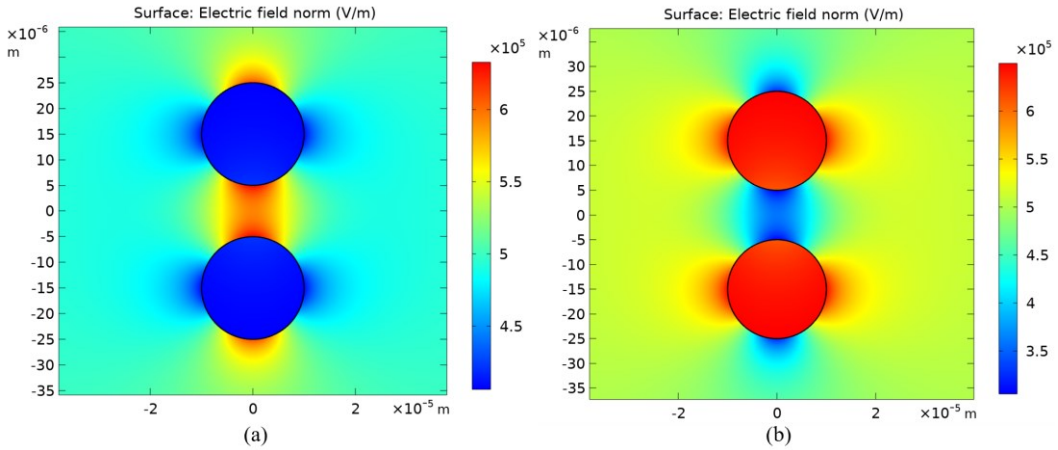

Figure 50 Electric field of two identical particles located at (x,y) = (0, ± 15 μm) with different permittivity (a) pDEP ($\varepsilon_p > \varepsilon_m$), (b) nDEP ($\varepsilon_p < \varepsilon_m$).

7.2 Problem Setup

A model system is set up to elucidate the self-assembly process of two dissimilar particles. As shown in Figure 51, it consists of a pair of two dissimilar spherical particles of radius a, P_1 and P_2, suspended in an incompressible and Newtonian fluid of a size $L \times L$. The intitial inter-particle distance is R. A uniform electric field $\vec{E}$ is applied along the y-direction with the electrostatic potentials being $\phi = \phi_1$ on AB and $\phi = \phi_2$ on CD. The angle between the electric field and the line connecting the centers of the particles is θ. After the electric field is actuated, the two paricles will experience DEP forces and itimiate the self-assembly process.

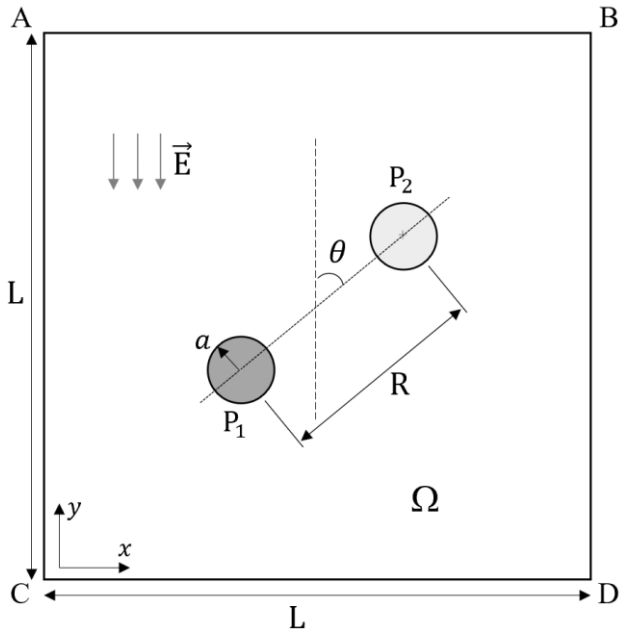

Figure 51 Scheme of simulation domain of particles with permittivity difference under a uniform field.

7.3 Numerical Results

7.3.1 Motion of Two Dissimilar Particles

Numerical simulations were performed for the particle-fluid system with

different initial configurations to obtain the particle trajectories during the DEP-directed fluidic assembly process of dissimilar particles. In the simulations presented here, the material property is indicated in Table 3. The particle radius is $a = 10$ μm and the initial center-center distance between the particles is set to be $R = 30\mu m$. The domain length is set to be $L = 200\mu m$, which is 20 times the particle size in order to eliminate the boundary effect on the particle motion. The electric field is defined with electrostatic potentials on the domain boundaries: $\phi_{AB} = 100$ V and $\phi_{CD} = 0$ V. In the flow problem, no slip boundary conditions are specified on Boundaries AB and CD and the particle surface, and inlet and outlet pressure conditions are set on Boundaries AC and BD.

Table 3 Material Property of Dissimilar Particles in DEP

Parameter	**Definition**	**Value**
ε_0	Permittivity of vacuum	$8.85 \times 10^{-5}\ F/m$
ε_m	Relative permittivity of fluid	100
ε_{p1}	Relative permittivity of P_1	150
ε_{p2}	Relative permittivity of P_2	50
μ	Fluid dynamic viscosity	1×10^{-3} Pa · S
ρ_m	Fluid density	1×10^3 Kg/m^3
ρ_p	Particle density	1×10^3 Kg/m^3

Configuration1

In the first configuration, the line connecting the centers of the particles makes an angle of $\theta = 0°$ with respect to the direction of the applied electric field. Figure 52 (a) (b) show that, unlike what happens for identical particles in Figure 50, the local field maxima occurs near the north pole of P_1 and the minima appears near the south pole of P_2. Thus, the pDEP particle P_1 will move upward to the field maxima whereas the nDEP P_2 go downward to the field minima, causing the two particles to separate from the

original positions. This is verified by the particle trajectories shown in Figure 52 (c) and the velocity field at the time instant t = 0.002s shown in Figure 52. (d). However, it will be shown next that this configuration is unstable and, if θ deviates slightly from 0°, the two particles will demonstrate a repulsion-then-attraction type of motion and line up along a direction perpendicular to the electric field.

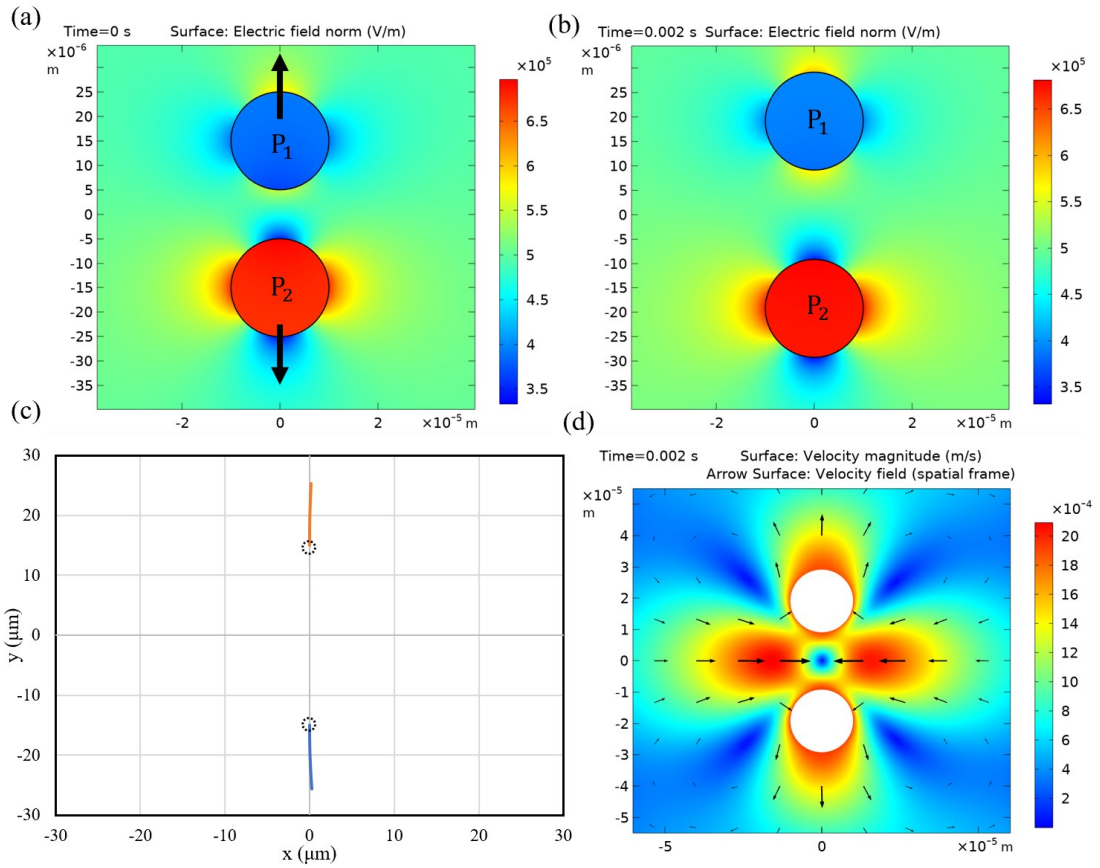

Figure 52 Particle-particle interaction with dissimilar particles, P_1 and P_2 located at $(x, y) = (0, \pm 13.9\ \mu m)$ (a) electric field at t = 0 s, (b) electric field at t = 0.002 s, (c) particle trajectories (the initial position of particle is indicated in dash line circle), (d) flow field at t = 0.002 s.

Configuration 2

In the more general scenario, two dissimilar particles are placed at initial locations $(x, y) = (\mp 2.6\ \mu m, \pm 14.77\ \mu m)$, respectively, corresponding to $\theta = 10°$.

From Figure 53 (a)-(d), it is seen that the electric field distribution changes drastically as time elapses. Initially, the field is almost identical to that shown in Figure 52. However, as the particles are displaced, the local minima region near the tropics of P_1 is shifted to a closer proximity of the local minima region near the north pole of P_2. In the meanwhile, the local maxima region near the south pole of P_1 is also getting closer to the local maxima region near the tropics of P_2. As a result, new global field maxima and minima are created simultaneously in the interparticle space, with the minima near P_1 and the maxima near P_2, Consequently, both particles are eventually attracted into contact.

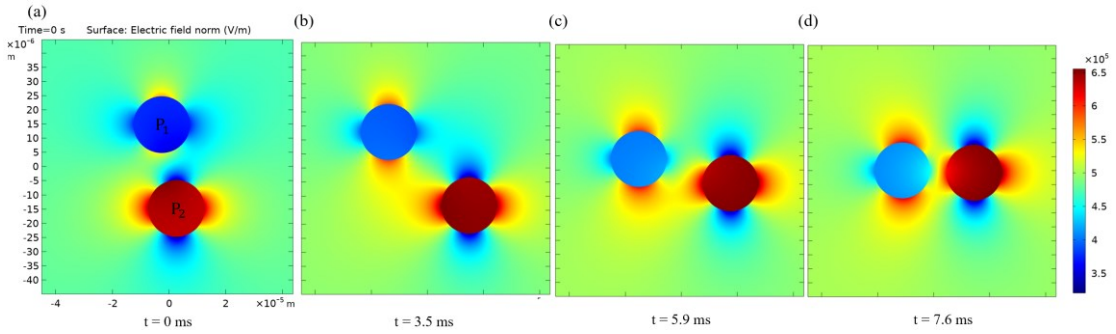

Figure 53 Electric field of dissimilar particles at (a) t = 0 ms, (b) t = 3.5 ms, (c) t = 5.9 ms

The instantaneous locations and the trajectories of the particles are shown in Figure 54 (a) (b), where the expulsion, rotation and attraction of the particles can be clearly observed. In particular, Figure 54 (c) depicts the variation of the interparticle distance, *R*, as a function of θ. It indicates the particles revolve around the origin in the counter clockwise direction while they are first pushing away from and then drawing closer to each other till, finally, they line up perpendicularly to the applied field. The maximum of *R* is found at $49.4°$

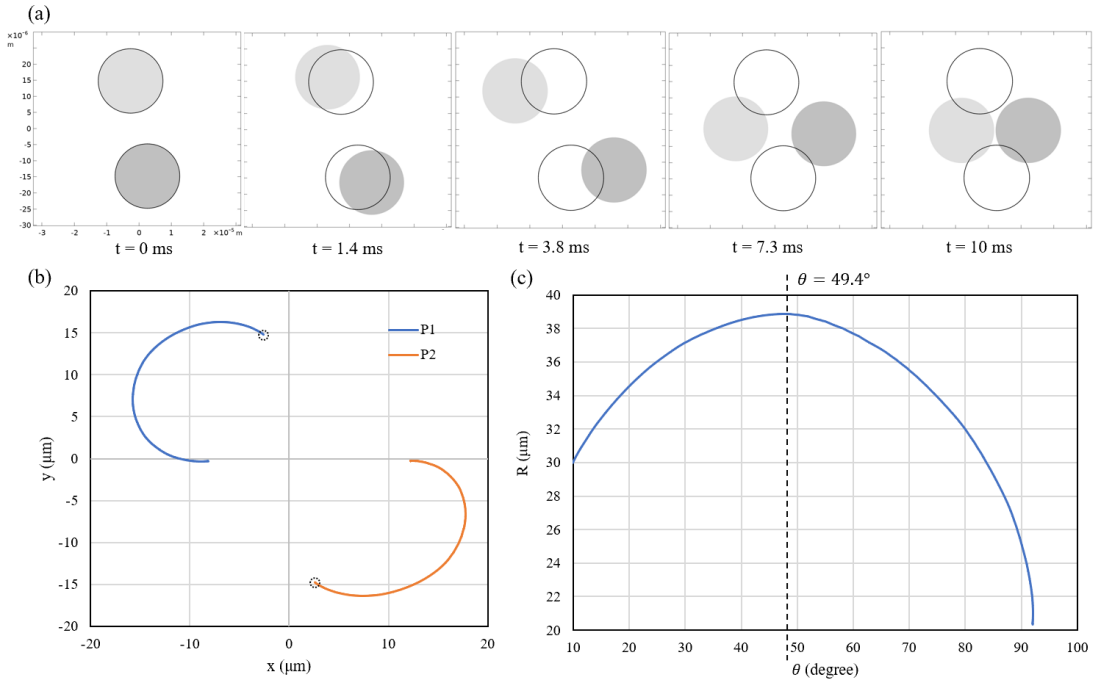

Figure 54 Dissimilar particles, P1 and P2 located at $(x, y) = (\mp 2.6\mu m, \pm 14.77\mu m)$, (a) motion of pair of particles, (b) relative motion trajectories of particles(dash line circle indicated the initial position), (c) R with the relation to θ.

Configuration 3

After the discussion the previous two particle configurations, the case for $\theta = 90°$, where P_1 and P_2 are located at $(x, y) = (\mp 15\mu m, 0)$, is almost trivial. As expected, the two particles attract to each other and form a chain along the centerline direction, as shown in Figure 55 (a). The x-component velocities of P_1 and P_2 are illustrated in Figure 55 (b), which shows that the particles first accelerate due to the DEP attraction force but then decelerate as the hydrodynamic pressure increases quickly when they are approaching each other.

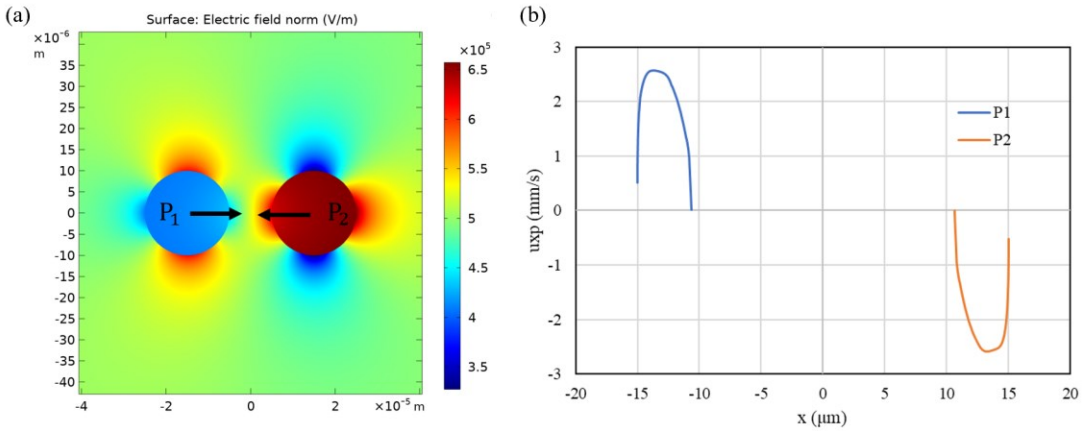

Figure 55 Dissimilar particles, P_1 and P_2 located at (x,y)=(∓15 μm,0), (a)electric field at t = 0 s, (b) velocity of pair of particles with changing of position x.

7.3.2 Motion of Three Dissimilar Particles

As discussed in Chapter 6, the two-particle system provides some basic information of the DEP-induced particle self-assembly process, but it is insufficient to reveal the key features of the particle-field-flow interactions involving multiple particles. Thus, a three-particle system is set up for the latter purpose. Figure 56 shows two different initial configurations where in (a) an array of three particles are located nearly perpendicular to the applied electric field and in (b) the array are nearly in parallel to the field. The exact locations of the particles are marked in the Figure 56. The particles have identical geometry, dimensions and physical properties except for the electric permittivity, $\varepsilon_{p1} = 150$, $\varepsilon_{p2} = 50$ and $\varepsilon_{p3} = 150$, i.e., P_1 and P_3 are pDEP particles and P_2 is a nDEP particle.

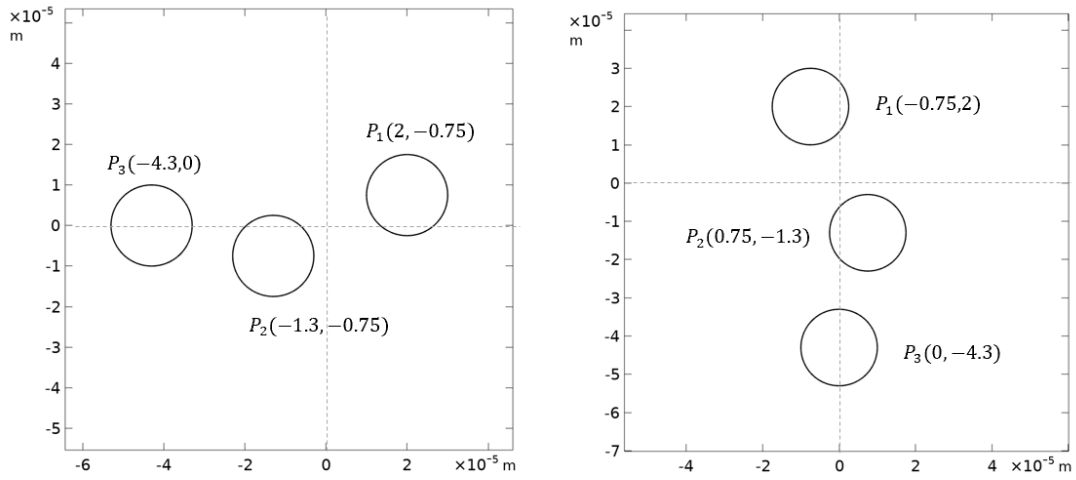

(a) (b)

Figure 56 Scheme of simulation domain, (a) P_1(20 μm,-75μm) and P_2 (-13 μm, -7.5 μm) and P_3 (-43 μm, 0 μm), (b) P_1(-7.5 μm,20 μm), P_2 (7.5 μm, -13 μm) and P_3 (0 μm, -43 μm).

Figure 57 shows the evolution of the electric field at some representative time instants for the first configuration. With the higher field gradient between P_2 and P_3, two particles exhibit strong interactions at the very beginning of the process. The local maxima region near the south pole of P_3 is getting closer to the local maxima region near the tropics of P_2. As a result, new local field maxima and minima are created simultaneously between P_2 and P_3, with minima near P_3 and the maxima near P_2. Therefore, P_2 and P_3 are first paired as indicated in Figure 57 (b). While at the at time, Figure 57 (c) shows that the local maxima region of P_1 is also getting closer to the local maxima region on the other side which directs P_1 gradually attract to P_2.

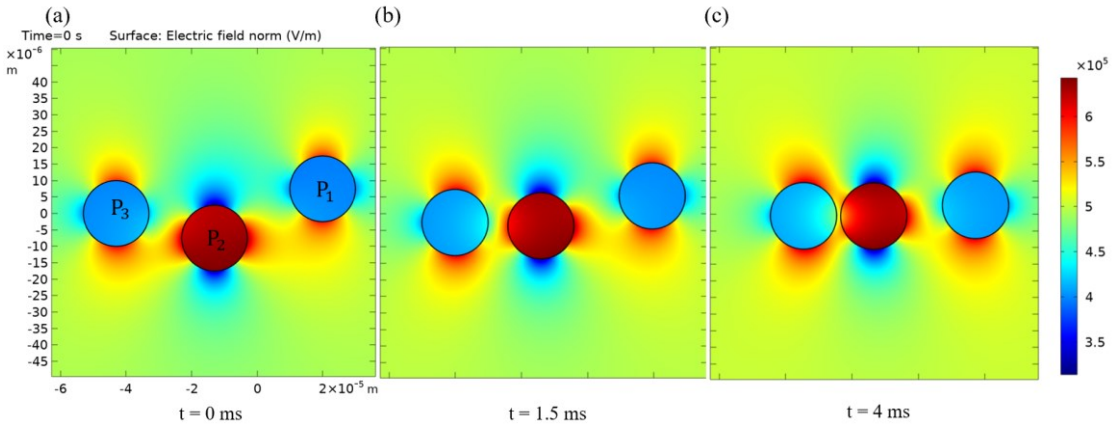

Figure 57 Electric field of three particles with P_2 as nDEP, P_1 and P_3 as pDEP at (a) t = 0 ms, (b) t = 1.5 ms, (c) t = 4 ms.

Figure 58 (a) shows the snapshots of motion of the three particles. Treating P_1 and P_2 as one pair of dissimilar particles and P_2 and P_3 as another, it is easy to see the particle motion follows what has been discussed in the last section. At the end, a pearl chain structure with three constituent particles is formed along the direction perpendicular to the electric field. This can be expected as one of the basic morphological units of the DEP-driven self-assembly of any three dissimilar particles that are oriented originally nearly perpendicular to the external electric field. The particle trajectories are shown in Figure 58 (b). Similar to motion of multiple identical particles, P_2, P_3 with the shortest interpaticle distance are paired very rapid (Figure 58 (c)). Once the P_2 and P_3 line up as a whole, P_1 is then attracted to join.

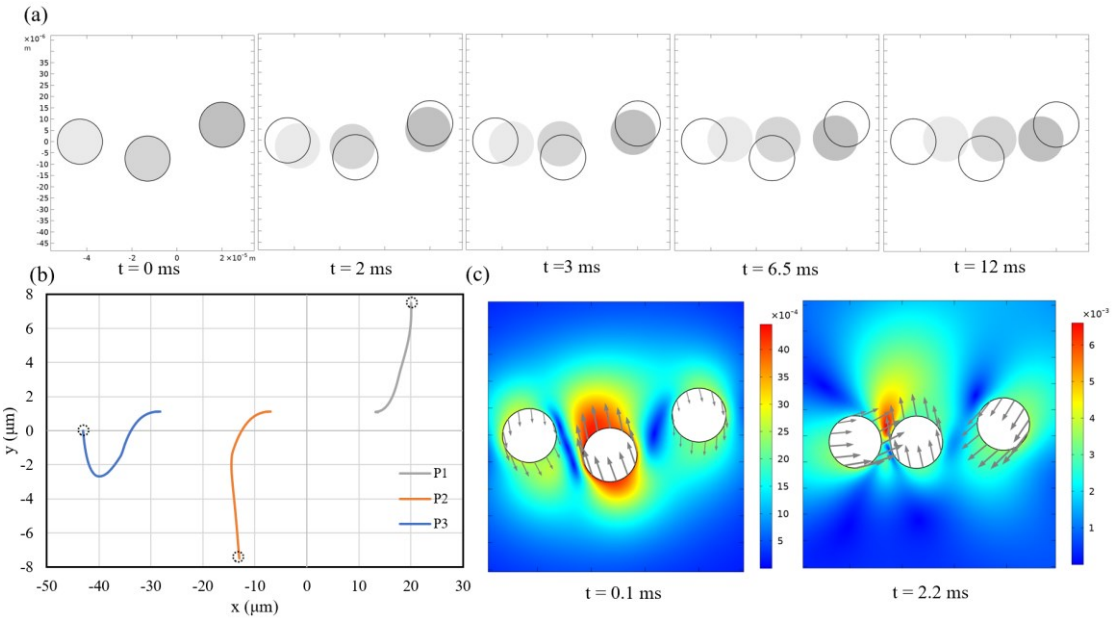

Figure 58 (a) Motion of pair of particles, (b) relative motion trajectories of particles,(dash line circle indicated the initial position), (c) fluid field in velocity at t = 0.1 ms and t = 2.2 ms.

Figure 59 shows the evolution of the electric field at some representative time instants for the second configuration. Initially, with the relatively close interpaticle distance, the local minima region near the south pole of P_2 are first shifted to a closer proximity of local minima near the tropics of P_3 as indicated in Figure 59 (b). In the meanwhile, the local maxima region near the north pole of P_3 is simultaneously getting close to both the local maxima region near the south pole of P1 and the tropics of P2. As a result, the new local maxima and minima region between P2 P3are created in the tropics of P3 and P2 respectively (Figure 59 (c)), which drive them moving toward to each other. While at the same time, the local maxima between P1 and P3 attract them into contact.

The particle motion is depicted in Figure 60. This time, particles P_1 and P_3 act as one pair of similar particles where P_2 and P_3 as the dissimilar pair. Accordingly, it

can be observed that the particle motion follows the behaviors that have been discussed in Sections 6.1.3 and 7.3.1. At equilibrium, the three particles form a triangular array, which can be expected as the second basic morphological unit of the DEP-driven self-assembly of any three dissimilar particles that are oriented originally nearly along the external electric field.

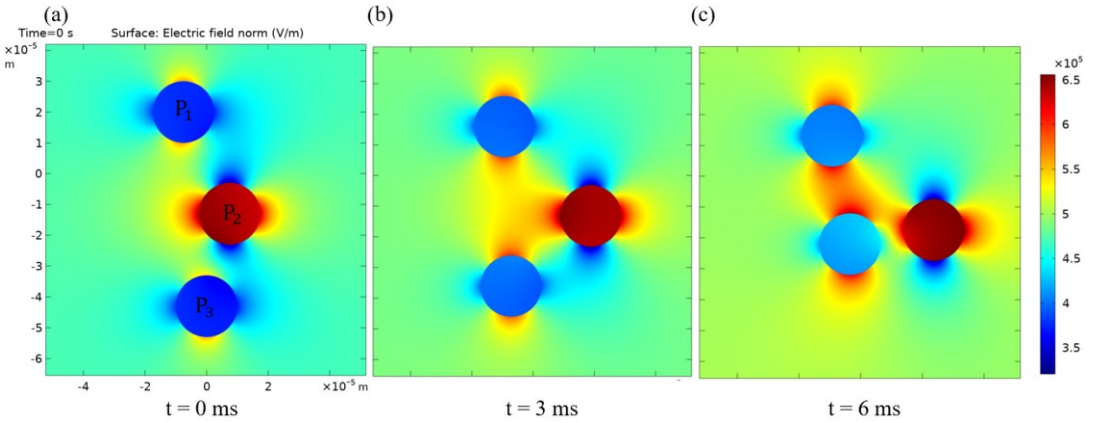

Figure 59 Electric field of three particles with P_2 as nDEP, P_1 and P_3 as pDEP at (a) t = 0 ms, (b) t = 3 ms, (c) t = 6 ms.

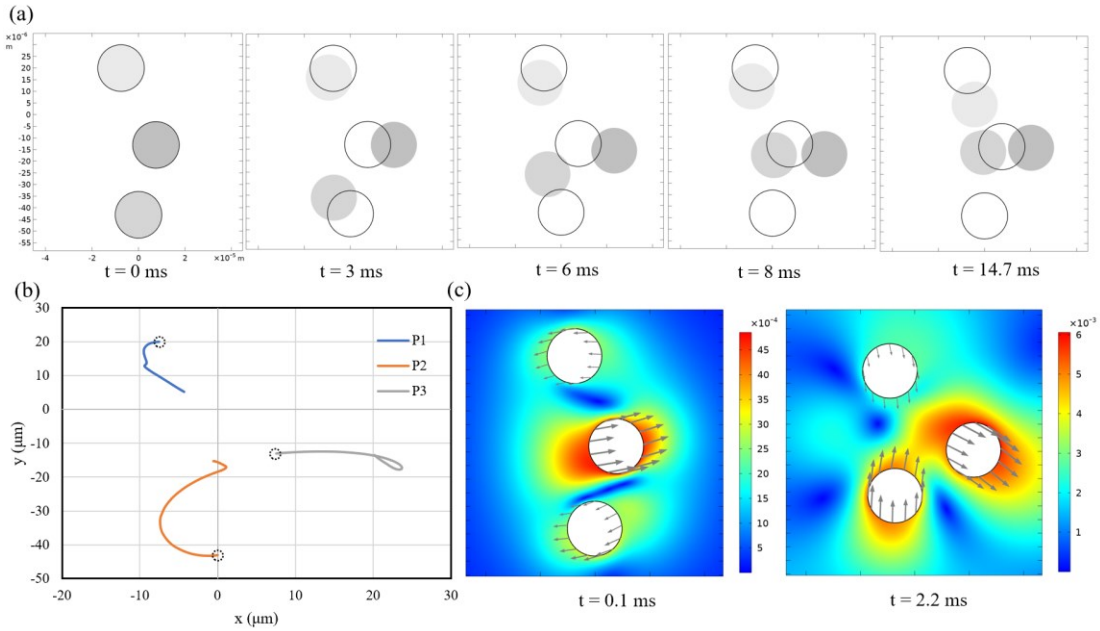

Figure 60 (a) Motion of pair of particles, (b) relative motion trajectories of particles,(dash line circle indicated the initial position), (c) fluid field in velocity at t = 0.1ms and t = 2.2ms.

To verify the basic morphological configurations just discovered, the DEP-driven self-assembly of a new set of dissimilar particles is investigated, for which the electric permittivities are chosen as $\varepsilon_{p1} = 150$, $\varepsilon_{p2} = 50$ and $\varepsilon_{p3} = 50$ for P_1, P_2 and P_3, respectively. The initial particle locations are shown in Figure 61 (a) and (b) for two different configurations. The simulated particle assembly processes are illustrated in Figure 61 (c) and (d). The motion of particles follows the same mechanisms discussed in the previous sections. The only exception is that just triangular arrays are formed at the end of the self-assembly process, which is due to the initial relative locations of the particles. The results prove again that the pearl chain or the triangular array will be the basic unit of DEP-driven particle assembly.

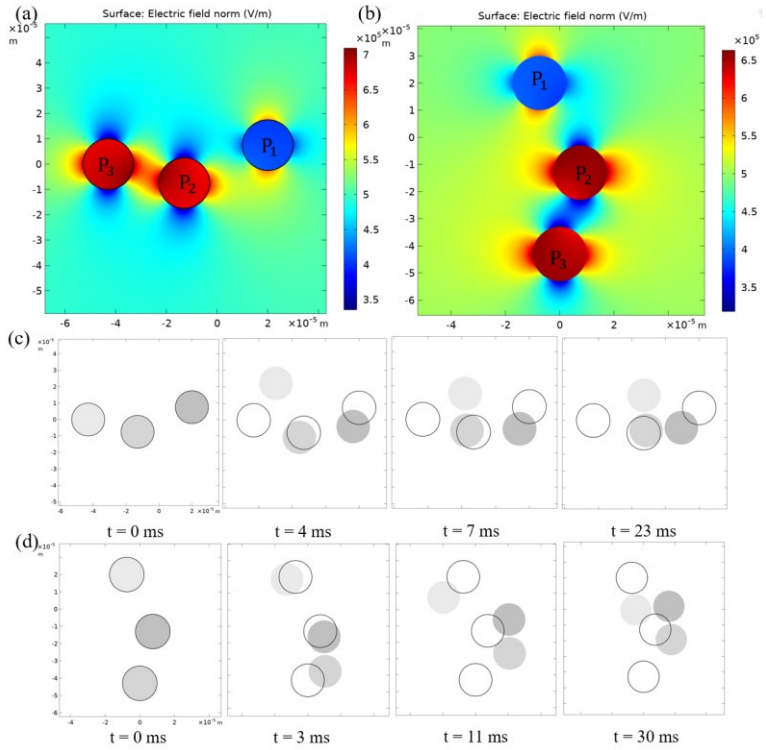

Figure 61 Three particles with P_2 and P_3 as nDEP, P_1 as pDEP, electric field in (a) configuration 1, (b) configuration 2., with the particle motion respectively in (c) configuration 1, (d) configuration 2.

7.3.3 Motion of Five Dissimilar Particles

Two basic morphological units in DEP-driven particle self-assembly have been identified from the study of the two-particle and three-particle systems. In this section, the motion of five dissimilar particles will be scrutinized to further pinpoint any issues that may emerge in more complex systems.

First, five Particles, P_1, P_2, P_3, P_4 and P_5, with similar-dissimilar particle arrangement are first studied, among which among which P_2, P4 are nDEP particles ($\varepsilon_{p1} = \varepsilon_{p2} = 50$) and the rest are pDEP particles ($\varepsilon_{p1} = \varepsilon_{p3} = \varepsilon_{p5} = 150$) as indicated in Figure 62.

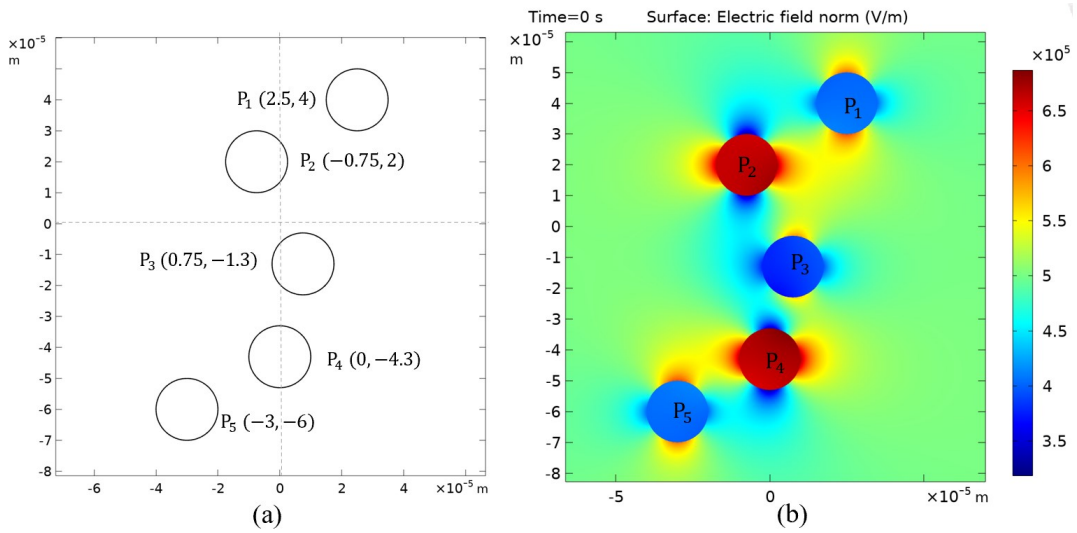

Figure 62 (a) Scheme of simulation domain, (b) electric field with P_1, P_3 P_5 as pDEPs, and P_2, P_4 as nDEPs.

Figure 63 shows the evolution of the electric field at consecutive time instants to represent the self-assembly process and interaction of five dissimilar particles. Initially, although P_3, P_4 with the shortest interpaticle distance, instead of exhibiting strong interaction and paring, P_3 and P_4 are respectively moving toward P_5 and P_1 due to the different electric field intensity in the vicinity of each particle. Once the particles

are displaced, the local minima and maxima in the interparticle space of P_4 and P_5 attracted them into contact. In the meanwhile, the local maxima region near the south pole of P_1 is simultaneously getting closer to both the local maxima region near the tropics of P_2 and north pole of P_3. As a result, P_4 and P_5 are paired firstly, while P_1, P_2 and P_3 form a triangular array as discussed in previous section.

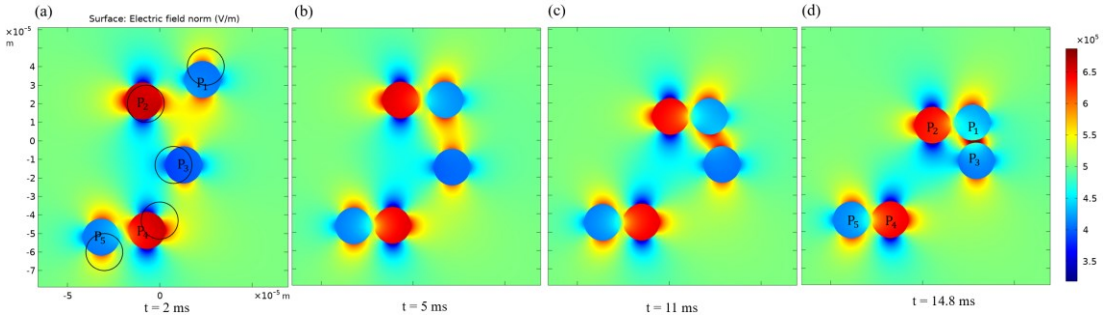

Figure 63 Electric field of three particles with P_2, P4 as nDEP, P_1, P_3 and P5 as pDEP at (a) t = 2 ms, (b) t = 5 ms, (c) t = 11 ms.(d) t = 14.8 ms (black circle indicated initial position of particles at t = 0 ms)

Then, Figure 64 (a) shows five particles with P_1 is a nDEP particle ($\varepsilon_{p1} = 50$) and the rest are pDEP particles ($\varepsilon_{p2} = \varepsilon_{p3} = \varepsilon_{p4} = \varepsilon_{p5} = 150$) which is investigated as below. Figure 64 (c) shows the particle motion at consecutive time instants. As expected from Chapter 6, similar particles P_3 and P_4 first line up along the direction of the external field since they have the shortest projected interparticle distance along the *x*-direction. Meanwhile, dissimilar particles P_1 and P_2 form a pair in a direction perpendicular to the field direction and, then, they move together under the DEP attraction forces to join the P_3-P_4-P_5 assembly, leading to the final pattern shown at t = 12.7 ms, which is consistent with the results obtained in [138] as in Figure 65.

In the third case, P_1, P_2 and P_3 are set as nDEP particles with $\varepsilon_p = 50$, while P_4 and P_5 are kept as pDEP particles $(\varepsilon_p = 150)$ as shown in Figure 64 (b). The DEP-

driven self-assembly process is shown in Figure 64 (d). It appears that similar particle groups are assembled into two pearl chain structures before the two chains start to interact. Starting from t = 10 ms, the pDEP particle chain is attracted to the field maxima near the tropics of the nDEP particle chain. During the process, the two chains retain their individual structural integrity without any deformation. Since the nDEP particle chain is larger, it has a higher inertia and experiences greater viscous resistance from the surrounding fluid medium. Thus, it is mainly the pDEP particle chain that moves to join the nDEP particle chain. Examining the final pattern formed reveals that, indeed, dissimilar particles are positioned in such a manner that their centerline is perpendicular to the external field, and the basic morphological units identified earlier remain in the DEP-driven self-assembly of the five-particle system.

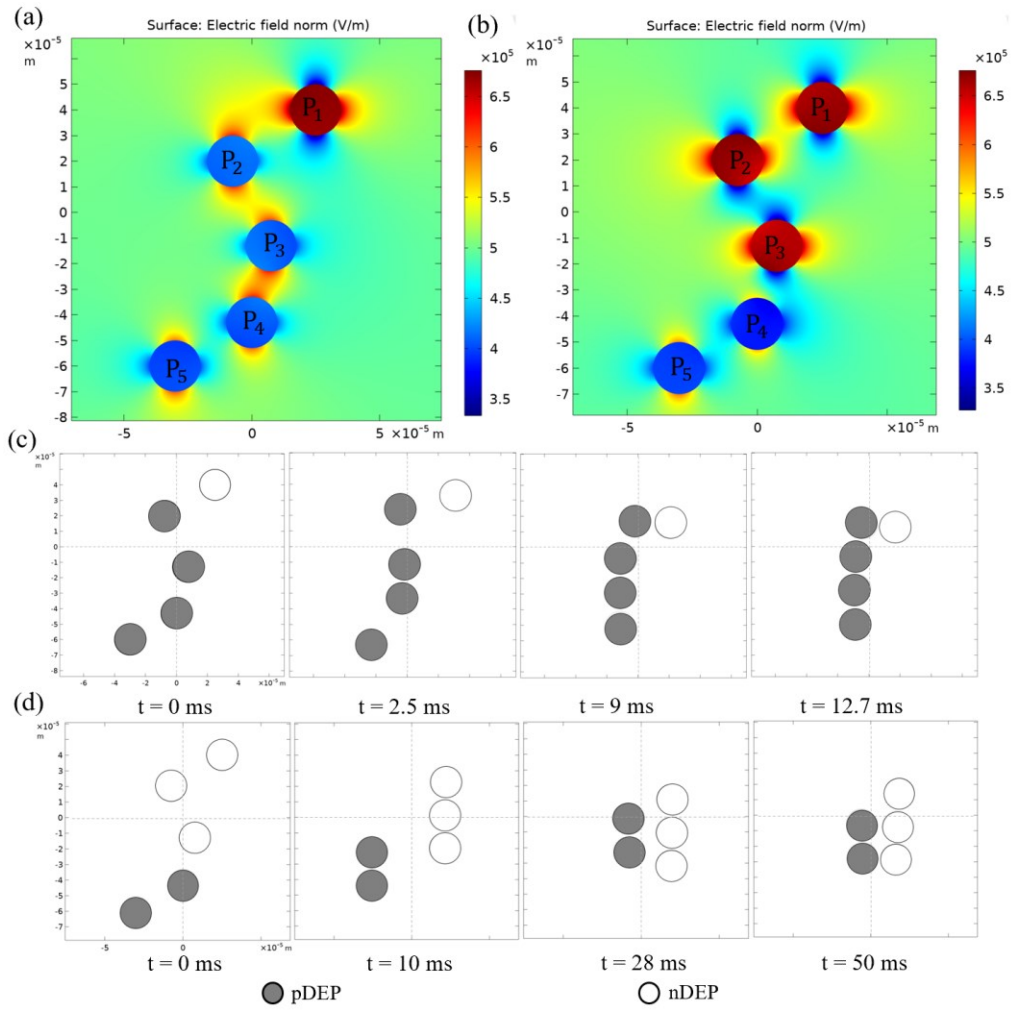

Figure 64 Four particles interaction (a) (c), $\varepsilon_{p1} = 50, \varepsilon_{p2} = \varepsilon_{p3} = \varepsilon_{p4} = \varepsilon_{p5} = 150$ in electric filed and particle motion, (b) (d), $\varepsilon_{p1} = \varepsilon_{p2} = \varepsilon_{p3} = 50, \varepsilon_{p4} = \varepsilon_{p5} = 150$ where where pDEP and nDEP particles are indicated in dark circle and white circle respectively.

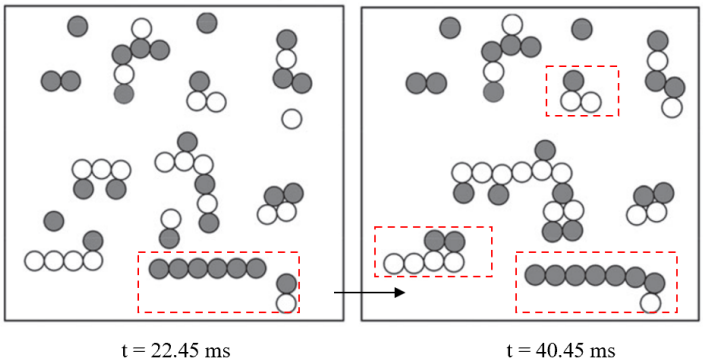

Figure 65 Model by Liu and Xie at t = 22.45 ms and t = 40.45 ms [138].

7.4 Conclusion

In this chapter, the motion of DEP self-assembly of dissimilar particles are studied in term of assembled structure, and the relative motion trajectory during the self-assembly. As the induced dipole in the dielectric particles experiences uneven electric field, DEP force is generated and dependent on the polarizability of the particles and surrounding media. When $\varepsilon_p > \varepsilon_m$, the positive DEP (pDEP) force drives the particles to the local maxima field strength. While conversely when $\varepsilon_p < \varepsilon_m$, particles are moving toward to the local minima field strength with the induced negative DEP (nDEP) force. Considering both pDEP and nDEP force in self-assembly, the dissimilar particles tend to be chained in the direction perpendicular to the applied field. While for multiple particles, comparing with identical particle with single chain structure, dissimilar particles are more likely to form multiple chains.

Chapter 8. Numerical Study of Particle Motion under Magnetophoresis

Manipulation of bioparticles by using magnetic field has found increasing utility in biological and biomedicine applications, such as tissue engineering and disease treatment, due to its noninvasiveness, simplicity, sensitivity and specificity compared to other means. Magnetophoresis (MAP), as the underlying driving mechanism, is the general term that describes the motion of magnetic particles through a viscous fluid under the influence of an external magnetic field. In most practical applications, where permanent magnets are used as the magnetic source and no current flow is involved, dielectrophoresis and magnetophoresis find a nearly perfect analogy in terms of the governing laws if the electrostatic potential is replaced by between the magnetic scalar potential and the electric field is replaced by the magnetic field strength. All the previous results obtained for dielectrophoresis can be translated to magnetophoresis with almost modifications, which can be applied to understand the particle-fluid-field interactions and guide the self-assembly process driven by magnetophoresis [140,141]. Recently, with the rapid advances in particles syntheses methods, complex particles with a myriad of shapes, compositions and functionalities are fabricated to serve the diverse applications, especially, in biology and medicine [142-146], where the particles incorporated in various bio-cells are highly irregular in geometry. Thus, this section focus on studying the magnetophoretic rotation and self-assembly of non-spherical particles under the effect of an applied external magnetic field.

8.1 Magnetophoretic Rotation of an Ellipsoidal Particle

8.1.1 Model Setup

A model system for the magnetophoretic rotation of an ellipsoidal particle is depicted schematically in Figure 66. The particle has a semi-major axis a and a semi-minor axis b and is suspended in an incompressible Newtonian fluid of a size $L \times L$. In this work, only prolate spheroid ($a > b = c$) is studied, where c is the third semi-minor axis which is parallel to the z-axis in the three-dimensional space. A uniform stationary magnetic field $\vec{H}$ is applied along the y-direction with the magnetic scalar potentials being $\psi = \psi_1$ on AB and $\psi = \psi_2$ on CD, where $\overrightarrow{H_{\parallel}}$ and $\overrightarrow{H_{\perp}}$ are the two components of the magnetic field strength vector $\vec{H}$ parallel and perpendicular to the semi-major axis, respectively. The angle between $\vec{H}$ and the semi-major axis is α.

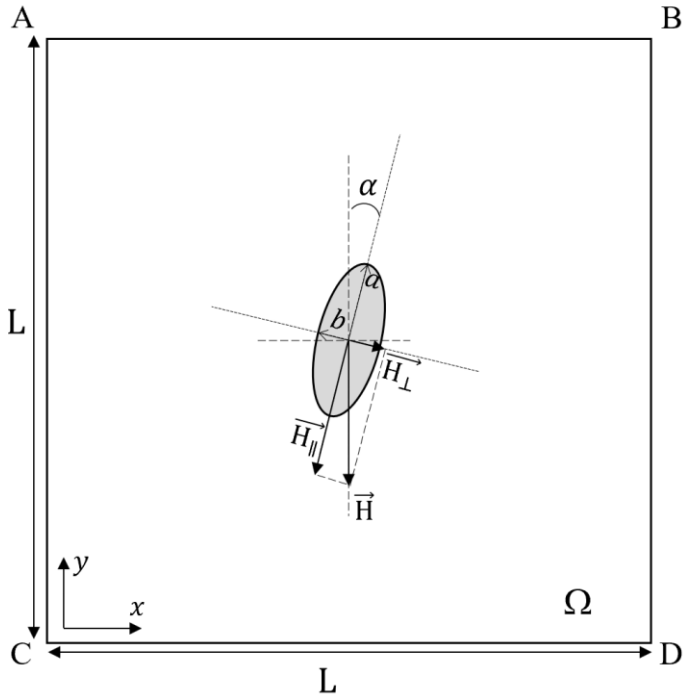

Figure 66 The computational domain of an ellipsoidal particle in MAP.

8.1.2 Theoretical Considerations

For a spherical particle exposed to a uniform magnetic field, it experiences a zero torque since the local magnetic force due to the Maxwell stress tensor $\overleftrightarrow{T}_M = \mu(\vec{H}\vec{H} - \frac{1}{2}H^2\overleftrightarrow{I})$ is always normal to the surface and passes through the centroid of the particle. For an ellipsoidal particle, measured by an aspect ratio ($p = \frac{a}{b}$) greater than unity, the magnetic force is distributed non-uniformly on the particle, leading to a magnetic torque that tends to align the major axis of the particle along the direction of $\vec{H}$, if $\alpha \neq 0$ initially. Some examples are shown Figure 67 where ellipsoids of different aspect ratios rotate from their initial positions until $\alpha = 0$.

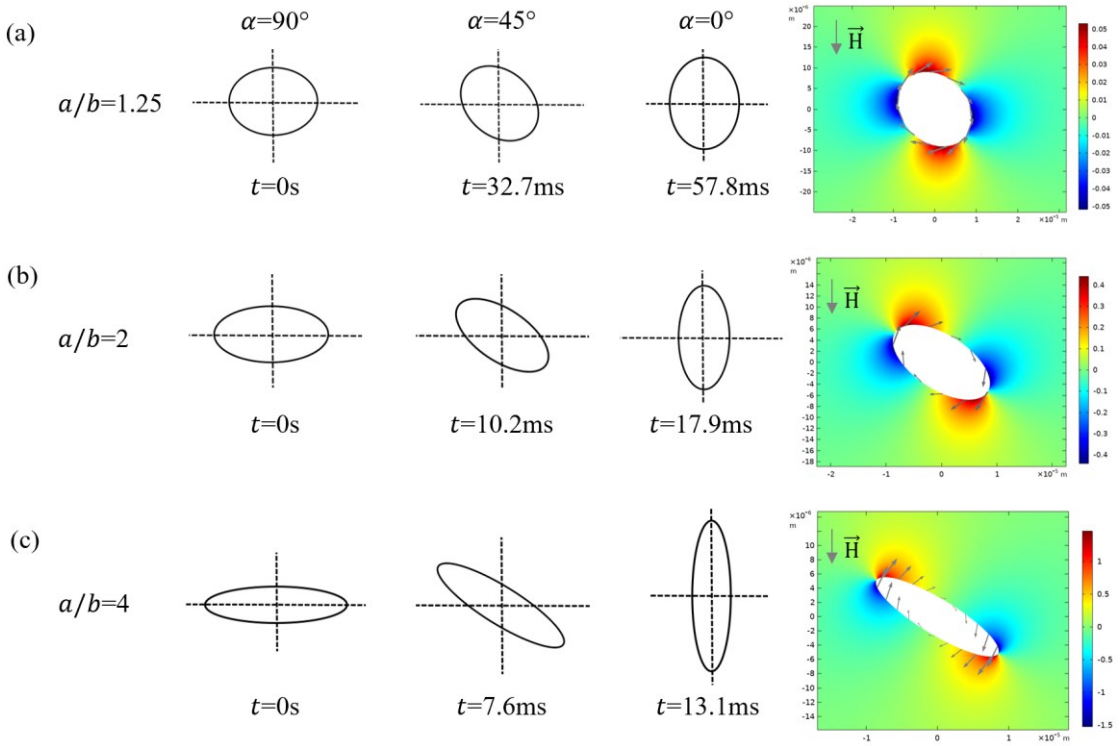

Figure 67. Ellipsoidal particle orientates to equilibrium state with applied magnetic field, indicated in pressure and velocity field with aspect ratio (a) 1.25, (b) 2 and (c) 4 respectively

The expression for the magnetic torque on an elliptical particle can be derived

rigorously, however, instead, it is obtained in this work with resort to the analogy between dielectrophoretic response of linear dielectric materials and magnetic response of linear magnetizable materials. The torque for dielectrophoretic-orientation of ellipsoid was given by Jones [102]

$$\vec{\tau}_{DEP} = \frac{4\pi abc\left(\varepsilon_p - \varepsilon_m\right)^2 (L_\perp - L_\parallel) E_\parallel E_\perp}{3\varepsilon_0 \varepsilon_m \left[1 + (\frac{\varepsilon_p - \varepsilon_m}{\varepsilon_m}) L_\parallel\right]\left[1 + (\frac{\varepsilon_p - \varepsilon_m}{\varepsilon_m}) L_\perp\right]} \hat{\vec{k}}. \tag{75}$$

Thus, the torque on magnetic ellipsoids takes an almost identical form

$$\vec{\tau}_{MAP} = \frac{4\pi abc\left(\mu_p - \mu_m\right)^2 (L_\perp - L_\parallel) H_\parallel H_\perp}{3\mu_0 \mu_m \left[1 + (\frac{\mu_p - \mu_m}{\mu_m}) L_\parallel\right]\left[1 + (\frac{\mu_p - \mu_m}{\mu_m}) L_\perp\right]} \hat{\vec{k}}, \tag{76}$$

where μ_p and μ_m are the magnetic relative permeability of the particle and the medium, respectively, $\hat{\vec{k}}$ is the unit vector in the *z*-direction, c is the third semi-minor axis, $L_\perp$ and $L_\parallel$ are the depolarization factor which is defined as below.

For ellipsoid, $a > b = c$, the following relations can be found

$$L_\perp = (1 - L_\parallel)/2, \tag{77}$$

$$L_\parallel = \frac{b^2}{2a^2 e^3}\left[ln\left(\frac{1+e}{1-e}\right) - 2e\right], \tag{78}$$

and

$$e \equiv \sqrt{1 - b^2/a^2}. \tag{79}$$

Further, since $H_\parallel = H\cos\alpha$ and $H_\perp = H\sin\alpha$, Eq. (76) becomes

$$\tau_{MAP} = \frac{2\pi abc{\mu_0}^2\left(\mu_p - \mu_m\right)^2 (L_\perp - L_\parallel)}{3\mu_m \left[1 + (\frac{\mu_p - \mu_m}{\mu_m}) L_\parallel\right]\left[1 + (\frac{\mu_p - \mu_m}{\mu_m}) L_\perp\right]} H^2 \sin 2\alpha. \tag{80}$$

According to Eq. (80), the magnitude of τ_{MAP} depends critically on the angle between

the major axis and the applied field. The magnetic torque vanishes when $\alpha = 0$ and the maximum appears at $\alpha_c = 45°$. This has some significant implications on the particle motion when it is under the influence of a rotating magnetic field, as will be shown by the simulation results.

8.1.3 Numerical Results and Discussion

Numerical simulations were performed for the particle-fluid system shown in Figure 66 to study the MAP-driven rotational motion of the particle. The material properties are summarized in Table 4. The domain size is set to be $L = 200$ μm. In the flow problem, no slip boundary conditions are specified at the particle surface and boundaries AB and CD, and inlet and outlet pressure conditions are set on boundaries AC and BD.

Table 4 Material Property of Particles in MAP

Parameter	**Definition**	**Value**
μ_0	Magnetic permeability of free space	$1.257 \times 10^{-6}\ H/m$
μ_m	Relative permeability of fluid	1
μ_p	Relative permeability of particle	2
μ	Fluid dynamic viscosity	1×10^{-3} Pa · S
ρ_m	Fluid density	1×10^3 Kg/m^3
ρ_p	Particle density	1×10^3 Kg/m^3

Uniform magnetic field

To gain basic understanding of the particle rotational behavior, an ellipsoidal particle with a size of $a = 10\ \mu m$ and $b = 2\ \mu m$ ($p = 5$) is firstly positioned at $\alpha = 90°$ in a uniform, stationary magnetic field. The field is defined by specifying the magnetic potentials on the domain boundaries: $\psi_{AB} = 1$ A and $\psi_{CD} = 0$ A. The particle starts to rotate once the magnetic field is applied. Due to the symmetry of the Maxwell

stress tensor, the net force on the particle is zero and, thus, it will not undergo translational motion. According to Eq. (80), the torque on the particle increases as α decreases until 45°, at which the torque reaches its maximum. This is verified by the simulation results shown in Figure 68 (a). The simulation is also seen to compare well with the theoretical prediction. Additionally, it is expected that the angular velocity of the particle will be influenced by not only the magnetic torque but also the viscous torque exerted by the surrounding fluid medium. This will be examined in greater detail in a later section. Nevertheless, the instantaneous velocity field around the rotating particle shown in Figure 68 (b) indicates that the maximum velocity (and also angular velocity) is obtained at $\alpha = 45°$ when the magnetic torque is the greatest.

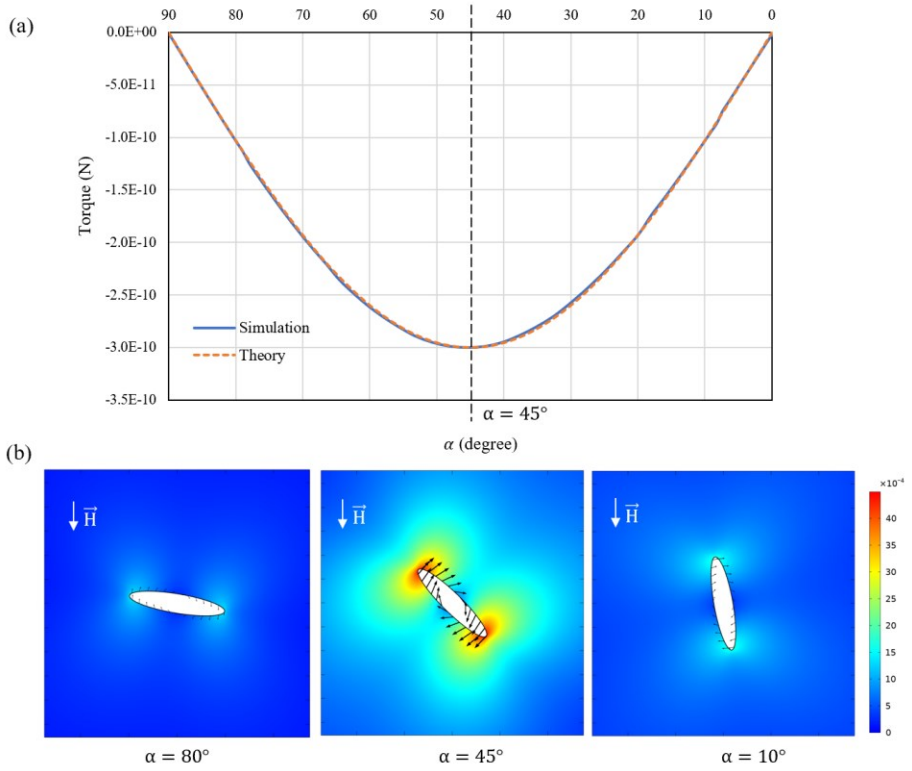

Figure 68 (a) Velocity contour of the flow field at three instantaneous particle locations ($\alpha = 80°$, $\alpha = 45°$, and $\alpha = 10°$, (b) Variation of the magnetic torque on the particle during the rotation process (the numerical result is denoted by the solid line and the analytical result is by the dashed line).

Next, the effect of the particle aspect ratio p on the magnetic torque is investigated. Using Eq. (80), the magnetic torque is nondimensionalized as

$$\tau_{MAP}^{*} = \frac{\tau_{MAP}}{\frac{2}{3}\pi abcH^{2}\mu_{0}\, sin\, 2\theta} = \frac{(L_{\perp} - L_{\parallel})}{(1 + L_{\parallel})(1 + L_{\perp})}, \tag{81}$$

where the depolarization factors $L_{\perp}$ and $L_{\parallel}$ are given in Eq. (77) to (79) and both are related to p. Figure 69 shows the variation of τ_{MAP}^{*} as a function of p. For $p = 1$, the ellipsoid degenerates into a sphere and no torque will be exerted on the particle. For larger p values, for instance, the particle becomes needle-like when p increases to 30, τ_{MAP}^{*} increases due to the asymmetry of the particle as suggested by Eq. 8. A total of 11 different particle geometries ($p = 1$, 2, 3, 4, 5, 7, 10, 15, 20, 30, and 40) have been tested, and the comparison of the results with the theoretical prediction (Eq. (81)) in Figure 69 shows that the theoretical expression provides a reasonable estimate of τ_{MAP}^{*} for aspect ratio up to $p = 9$, after which it significantly underpredicts τ_{MAP}^{*}, pointing to the necessity of numerical simulations in yielding accurate description of the magnetic manipulation of non-spherical particles.

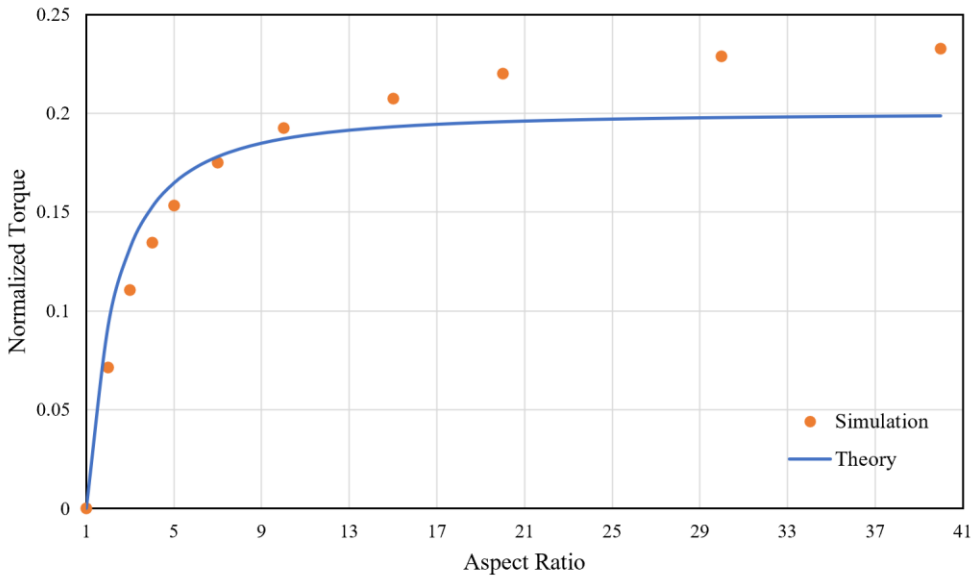

Figure 69 MAP torque with the relation to aspect ratio (numerical solution and analytical solution are indicated in solid line and dot respectively).

Rotating external field

Magnetic rotation of ellipsoidal particles with a rotating magnetic field is then investigated due to its extensive application in micro/nanofluidics and biomedical engineering, such as nanomotor [147], drug delivery [148], and nanosensors [149]. Depending on the angular velocity of the external applied field ω_H, the rotation of the ellipsoidal particle can be either synchronous, where the angle between the external field and the semi-major axis α_L is constant, or asynchronous, where α_L shows periodic oscillation [150,151].

As the external magnetic field $\vec{H}$ is applied with the constant angular velocity ω_H as indicated in Figure 70, the ellipsoidal particle tends to follow the rotation with its own angular velocity ω_p in an effort to align its semi-major axis with the direction of the applied field, as previous discussed. However, owing to the impact of viscous drag

from the surrounding medium, there is always a lag angle α_L between the particle and the field direction [152]. Therefore, the angular momentum equation of the particle can be written as

$$\vec{\tau}_{MAP} - \vec{\tau}_d = I\frac{d^2\alpha_p}{dt^2}, \tag{82}$$

$$\vec{\tau}_{MAP} = 2\pi ab^2 M_s H \sin\alpha_L, \tag{83}$$

and

$$\vec{\tau}_d = \gamma\omega_p = \frac{8}{3}\omega_p \pi\mu a^3 C. \tag{84}$$

where μ is the viscosity of fluid and C is the geometric constant related to the aspect ratio of the particle. Based on this, Yang et al. [153] derived the governing equation for ellipsoidal particles with high aspect ratio ($p > 20$)

$$\frac{d\alpha_L}{dt} + \omega_c \sin\alpha_L = \omega_H, \tag{85}$$

where

$$\omega_c = \frac{3M_s H}{\mu C}\left(\frac{b}{2a}\right)^2. \tag{86}$$

where ω_c is the critical angular velocity and M_s is the saturation magnetization.

When $\omega_H \leq \omega_c$, a steady-state solution for Eq. (85) is

$$\alpha_L = arcsin\left(\frac{\omega_H}{\omega_c}\right). \tag{87}$$

With constant lag angle, the ellipsoidal particle rotates synchronously with the magnetic field and motion of particle is stable. When $\frac{\omega_H}{\omega_c} \leq 1$, the magnetic torque is balance with viscous torque to maintain the constant lag angle.

If $\omega_H > \omega_c$, the ellipsoidal particle is in the asynchronous rotation, there is a

periodic solution for Eq. (85).

When $0 \leq \alpha_L < \pi$

$$\alpha_L = 2\,arctan(\frac{\omega_c}{\omega_H} + \sqrt{1-\left(\frac{\omega_c}{\omega_H}\right)^2}\,tan\frac{(\omega_H t + \beta\sqrt{1-\left(\frac{\omega_c}{\omega_H}\right)^2}}{2}. \quad (88)$$

Therefore, α_L exhibit time periodic oscillations, while the ellipsoidal particle will rotate back-and-forth with respect to the external magnetic field.

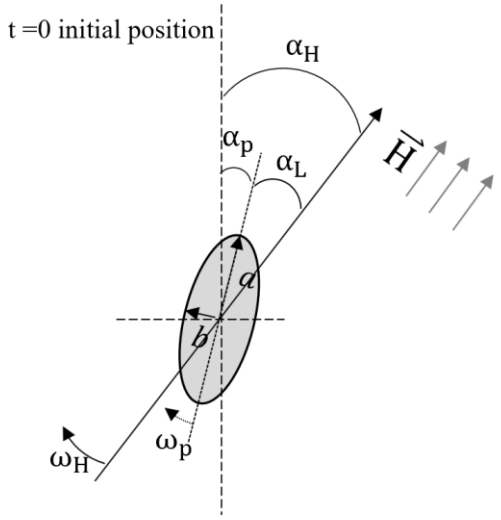

Figure 70 Schematic of magnetophoretic rotation of an ellipsoidal particle in a rotating magnetic field.

While the magnetic rotation of non-spherical particles, especially, nanowires, has been systematically studied both analytically and experimentally, most available work was for nanowire with very large aspect ratios ($p > 20$) and the dynamic behavior of ellipsoidal particles with small-to-medium aspect ratios has not been fully studied. In this work, the rotation of an elliptical particle of an aspect ratio $p = 5$ ($a = 10\mu m$ and $b = 2\mu m$) is simulated in a uniform magnetic field with $H = 5000\ A/m$ rotating with a constant angular velocity.

First, a low annular velocity of the magnetic field, $\omega_H = 5.48\, rad/s$, is used to study the synchronous rotation of ellipsoidal particles. As indicated by Figure 71, the particle is initially aligned with the magnetic field with $\alpha_L = 0$ and, once the magnetic field starts rotation, the particle is driven into motion by the magnetic torque to follow the moving field. Figure 71 (a) shows that α_L increases from zero and eventually reaches a steady state value at t = 6 ms, where the particle is moving with the magnetic field with the same angular velocity, i.e., $\omega_p = \omega_H$.

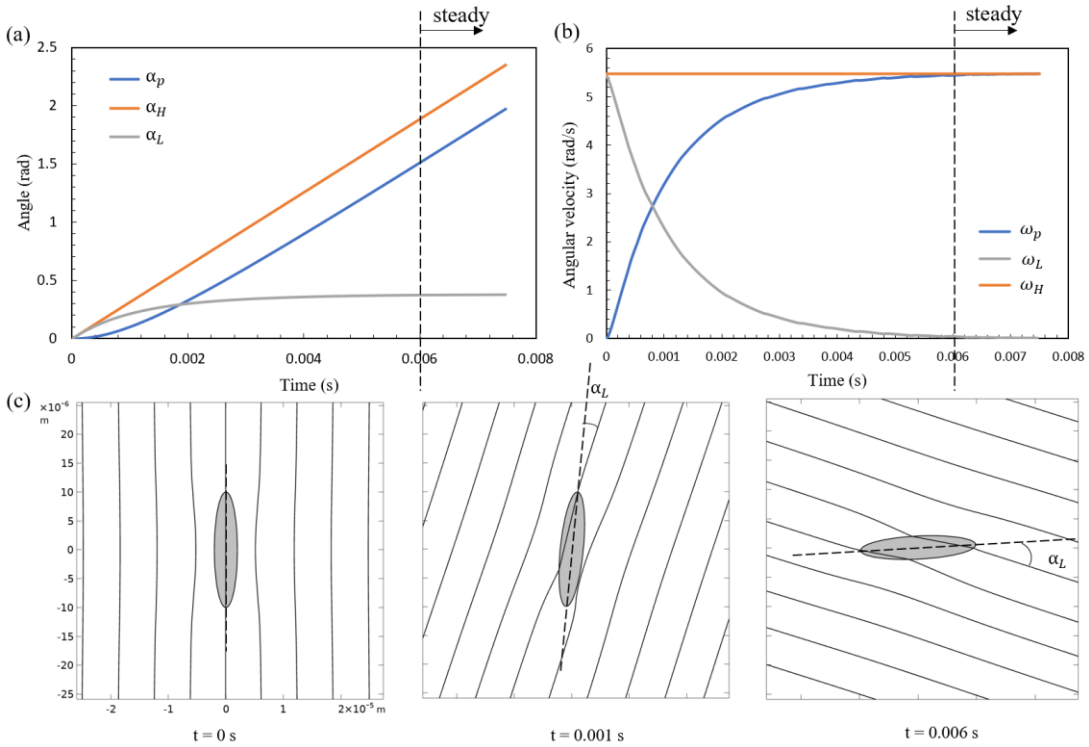

Figure 71 Synchronous rotation of ellipsoidal particle, (a) angle (α_L, α_p, α_H) changes with time (b) angular velocity (ω_L ω_P, ω_H) changes with time, (c) particle motion

With an increase in the angular velocity of the magnetic field, the asynchronous rotation is obtained. For the simulation shown in Figure 72, the external magnetic field is rotating at $\omega_H = 13.32\, rad/s$. In the beginning, the angular velocity of ellipsoidal particle ω_p is increasing to follow the rotation of the magnetic field as indicated in

Figure 72 (a). After reaching the highest speed at t = 2.1 ms (Figure 72 (b)), the angular velocity of particles is decreased.to zero when $\alpha_L = \frac{\pi}{2}$, where magnetic momentum of particles and the magnetic field are aligned opposite and the ellipsoid particle becomes static. As the external field continuously rotating, the ellipsoid particle is rotating backward as shown in Figure 72 (b). Since the ellipsoid particle and the field are moving opposite to each other, the lag angle is rapidly increased to π, where the ellipsoid particle and the magnetic field are perfectly aligned as indicated in Figure 72 (c) when t = 5.49 ms.

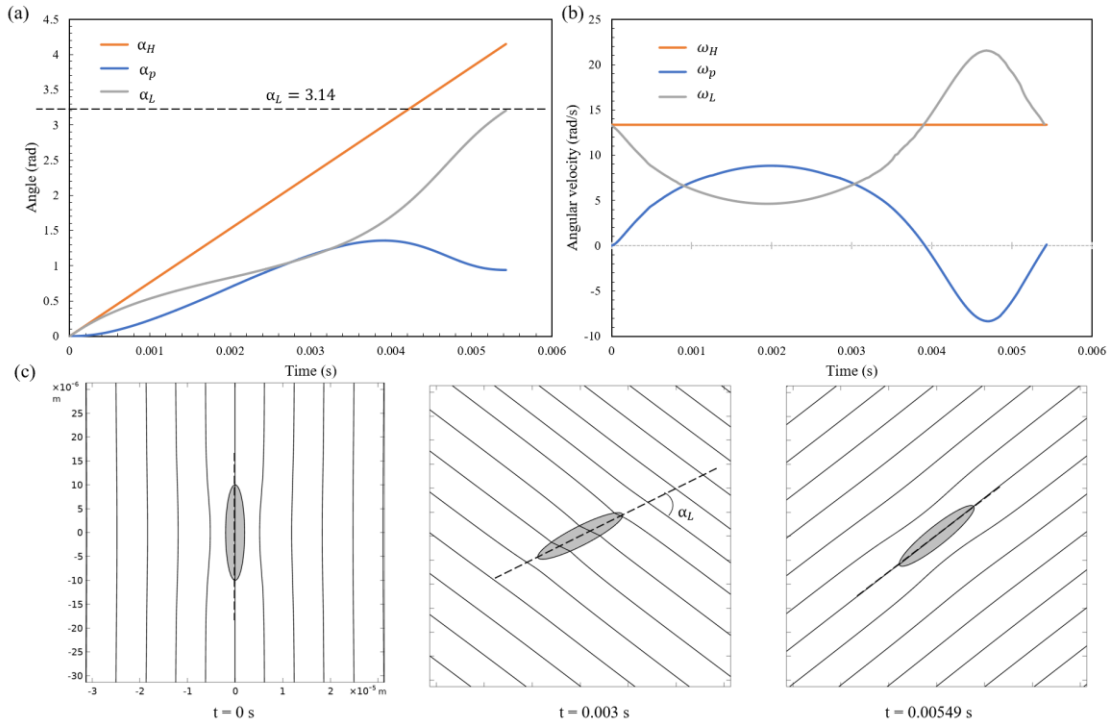

Figure 72 Asynchronous rotation of ellipsoidal particle, (a) angle (α_L, α_p, α_H) changes with time (b) angular velocity (ω_L ω_P, ω_H) changes with time, (c) particle motion

8.2 Magnetophoretic Motion of Multiple Ellipsoidal Particles

Similar to the investigations on the pearl chaining phenomenon in DEP-driven particle motion, magnetically-induced self-assembly of multiple elliptical particles will

be studied in this section.

8.2.1 Model Setup

The scheme for this study is shown in Figure 73. Two ellipsoidal particles P_1 and P_2 are suspended in the fluid medium, which have identical geometry with a semi-major axis of $a = 15$ μm and a semi-minor axis of $b = 5\mu m$. The corresponding initial angles with respect to the direction of the magnetic field are α_1 and α_2, respectively. The intitial interparticle distance is R and the angle between the magnetic field and the line connecting the centers of the particles is θ. After the magnetic field is actuated, the ellipsoidal paricles will experience magnetic force and torque, and start to assembly while aligning with the applied field.

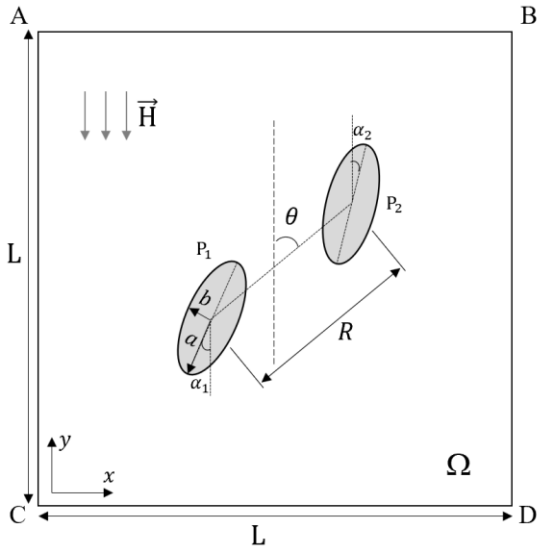

Figure 73 Scheme of simulation domain with ellipsoids under a uniform field.

8.2.2 Numerical Results and Discussion

Motion of two particles

Numerical simulations are performed for the particle-fluid system with different

initial configurations to obtain the particle trajectories during the MAP-directed fluidic assembly process. In the simulations presented here, the material properties are listed in Table 4. The initial position of two elliptical particles are located at the center positions ($\mp 14.77\ \mu m, \pm 2.6\ \mu m$). The initial center-center distance is $R = 30\mu$m and the angle with respect to the field is $\theta = 80°$.

Two particles oriented with $\alpha_1 = 0°$ and $\alpha_2 = 0°$ are firstly studied. The particle motion in represented in Figure 74 (a). The particle motion mimics the DEP-driven motion of spherical particles in that the two ellipsoids initially repel each other by the induced magnetic force and, with continuous revolution of the centerline in the clockwise direction, the particles then move closer. Eventually, they align themselves along the direction of the applied field.

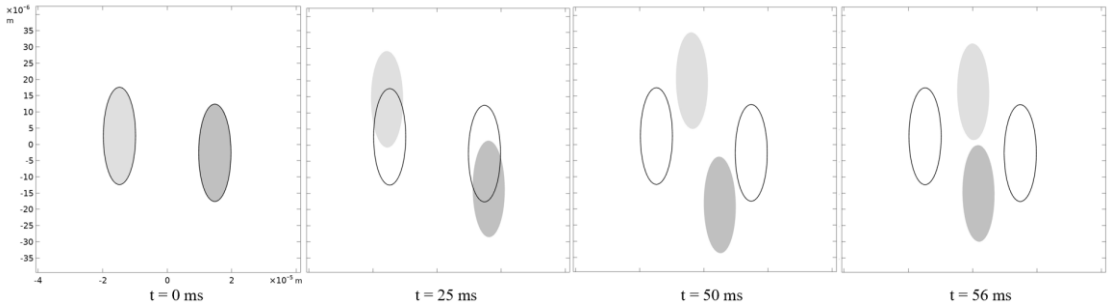

Figure 74 Motion of pair of ellipsoidal particles located at $(x, y) = (\mp 14.77\mu m, \pm 2.6\mu m)$ with $R = 30\ \mu m$, $\theta = 80°$, $\alpha_1 = \alpha_2 = 0°$, $p = 5$,

To further study the impact of initial particle orientation on the self-assembly process, the initial angles α_1 and α_2 are set to be 0° and 90°. The simulated particle motion is shown in Figure 75 (a), where, in the very beginning, P_2 undergoes primarily rotational motion due to the induced magnetic torque to attain the orientational equilibrium till its semi-major axis is parallel to the applied field. Figure 75 (b) shows α_2 as a function of the instantaneous angle θ where α decreases dramatically with

decreasing θ and reaches to 0 when $\theta = 65.9°$. Particle P_1 with $\alpha_1 = 0°$ does not exhibit much rotational behavior, but rather, it translates upward to reach a new equilibrium that puts it in a chain with P_2. Further, as indicated by Figure 75 (c), during the magnetic rotation of P_2, its translational velocity is almost negligible. The change of θ in the beginning of the process is mainly due to the translational motion of P_1.

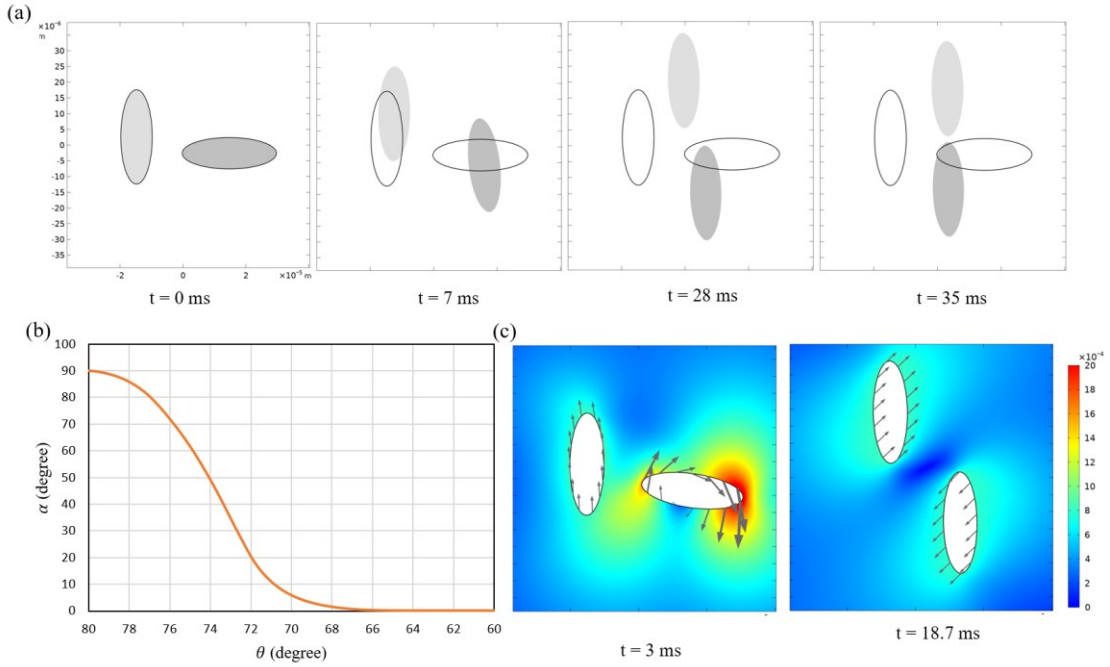

Figure 75 Pair of ellipsoidal particles located at $(x, y) = (\mp 14.77\mu m, \pm 2.6\mu m)$ with $R = 30\mu m$, $\theta = 80°$, $\alpha_1 = 0°$, $\alpha_2 = 90°$, $p = 5$, (a) motion of particles, (b) the relation between α and θ (c) velocity contour with the same color range from (0, 0.002 m/s) at $t = 3\ ms$, $t = 18.7\ ms$.

Motion of three particles

Considering the complexity of multiple particles system, the simulation is extended to three elliptical particles to investigate the impact of both the magnteic rotation and interparticle interaction on the particle pattern formation.

Three particles are located in a configuration shown in Figure 76 (a), with the orientatial angels $\alpha_1 = 60°$, $\alpha_2 = 60°$, $\alpha_3 = 30°$,interparticle distance $R_{12} = 41.8\mu m$, $R_{23} = 37.8\mu m$, and $\theta_{12} = 24.7°$, $\theta_{23} = 11.5°$. The simulated particle motion is shown in Figure 76 (a). With the closest interparticle distance R_{23}, P_2 and P_3 first move toward each other by the induced interparticle magnetic force while, simultaneously, they adjust their major axii to be both aligned with the external magnetic field. At *t* = 5.4 ms, P_2 and P_3 become a pair and then act as one body which eventually attracts P_1 to form a three-particle pearl chain structure. The angel between the semi-major axis to external field α is shown in Figure 76 (c) as a function of time. With the external magnetic field applied, the magnetic torque is induced and it directs the particle to align its major axis to the applied field regardless of the initial position. Although the translational motion of P_1 becomes significant until P_2 and P_3 paired at t = 5.4 ms, the magnetic rotation of P_1 is simultaneously initiated with P_2 and P_3 once magnetic field applied.

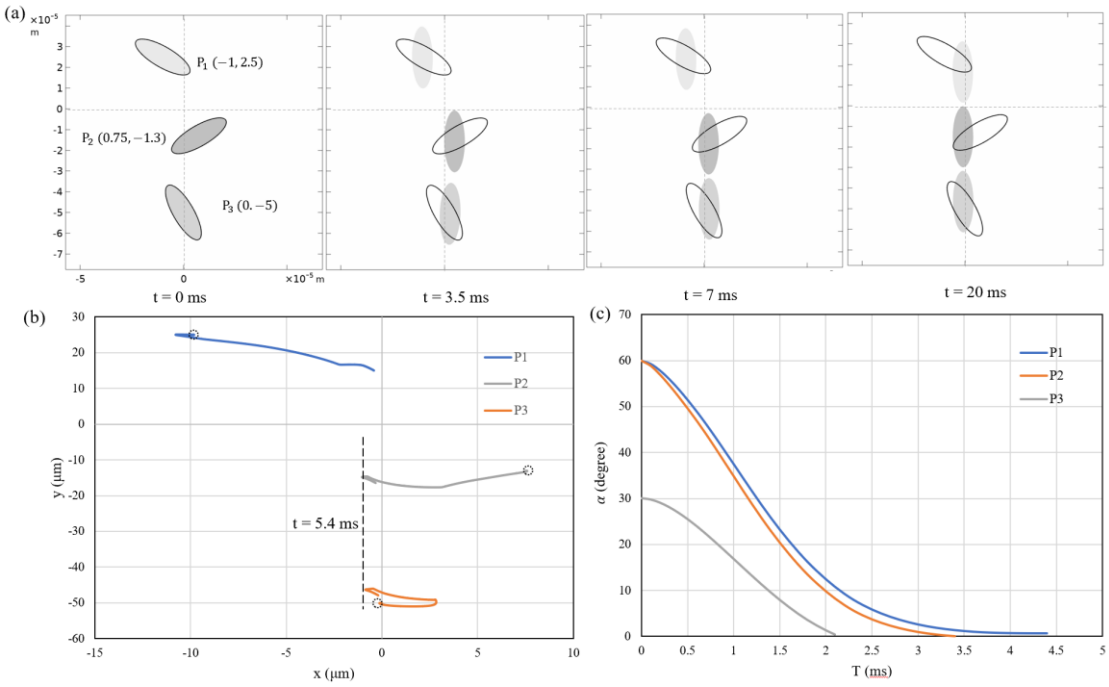

Figure 76 Three ellipsoidal particles with $\alpha_1 = 60°$, $\alpha_2 = 60°$, $\alpha_3 = 30°$, (a) motion of particles, (b) relative motion trajectories (c) The angel between the semi-major axis to external field α of P_1, P_2, and P_3.

8.3 Conclusion

In this chapter, the motion of MAP driven of ellipsoidal particles motion are studied numerically in terms of particle orientation and self-assembly. Ellipsoidal particle tends to align with its longest axis parallel with the induced magnetic torque to attain the orientational equilibrium with the induced MAP torque, which is highly dependent on the particle shape when in relatively small aspect ratio. For ellipsoidal particles self-assembly process, the magnetic torque and interparticle MAP force take place simultaneously to reach the final equilibrium state. The ellipsoidal particles with the initial angle $\alpha \neq 0$ will go through the electro-rotation process at the very beginning of the self-assembly process

Chapter 9. Conclusion and Future Work

9.1 Conclusion

To develop an effective cure for spinal cord injury (SCI), self-assembly of neural stem cells (NSCs) impregnated with superparamagnetic iron oxide nanoparticles (SPIONs) are exploiting with experimental and numerical study in this dissertation.

First, in vitro experiments are conducted. Cationic magnetoliposomes (CMLs) is first synthesized with SPIONs encapsulated in the core. The procedure for CMLs synthesis is established in two method, reverse-phase evaporation and inverted emulsion method. Before cell study, the biocompatibility study of SPIONs and CMLs are performed respectively to evaluate the toxicity. CMLs are then co-culture with targeted cell lines for cellular internalization. With the SPIONs-labeled 3T3 cells and NSCs, the morphology and proliferation of the two-dimensional (2D) and three-dimensional (3D) bioscaffold self-assembled are investigated. Under the designed external magnetic field, the SPIONs labeled NSCs are spontaneously self-assemble into structured lattices, thereby forming a scaffold to guide the directional regrowth of axons.

To further investigate the aggregation kinetics and pattern formation of particles in a fluid medium. A multiphysics numerical framework is established to simulate the particle motion and self-assembly undergoing DEP and MAP respectively. The numerical models are developed by combing the Maxwell Stress Tensor (MST) approach and arbitrary Lagrangian-Eulerian (ALE) method to solve the particle-fluid-field interaction problem, in which the motion of the particles (both translation and rotation), the flow field and the external electric/magnetic field are closely coupled. The Maxwell stress tensor (MST) approach, which enable the calculation of particles with

arbitrary shape or in the region with strong gradient, is applied to investigate the particle-particle and particle-field interactions and irregular shaped particles. Using this framework, the DEP and MEP alignment processes and interparticle interaction are studied in terms of identical particles, dissimilar particles and irregular-shaped particles.

In conclusion, the experimental data in this work proves the efficacy of the proposed approach in fabricating injectable and alignable bioscaffold for neural tissue engineering and the numerical model provides a powerful tool to investigate the particle motion in multiphysics problem.

9.2 Future Work

In the foregoing procedures, in vitro experiments are expected to investigate the SPIONs-labeled NSCs to obtain the ideal scaffold for spinal cord nerve repair with the feature of injectabilty, alignability and bioactivity. Numerical framework can be extend to 3D simulation and represent the flexibility and deformability of soft particles, which will prove more relevant to future studies in biological and biomedical applications.

References

1. Filous, A. R., & Schwab, J. M. (2018). Determinants of Axon Growth, Plasticity, and Regeneration in the Context of Spinal Cord Injury. *Am J Pathol, 188*(1), 53-62.
2. Han, S. M., Baig, H. S., & Hammarlund, M. (2016). Mitochondria Localize to Injured Axons to Support Regeneration. *Neuron, 92*(6), 1308-1323.
3. Tam, R. Y., Fuehrmann, T., Mitrousis, N., & Shoichet, M. S. (2014). Regenerative therapies for central nervous system diseases: a biomaterials approach. *Neuropsychopharmacology : official publication of the American College of Neuropsychopharmacology, 39*(1), 169-188.
4. Assunção-Silva, R. C., Gomes, E. D., Sousa, N., Silva, N. A., & Salgado, A. J. (2015). Hydrogels and Cell Based Therapies in Spinal Cord Injury Regeneration. *Stem Cells Int, 2015*, 948040.
5. Katoh, H., Yokota, K., & Fehlings, M. G. (2019). Regeneration of Spinal Cord Connectivity Through Stem Cell Transplantation and Biomaterial Scaffolds. *Frontiers in cellular neuroscience, 13*, 248-248.
6. Dulin, J. N., & Lu, P. (2014). Bridging the injured spinal cord with neural stem cells. *Neural regeneration research, 9*(3), 229-231.
7. Cummings, B. J., Uchida, N., Tamaki, S. J., Salazar, D. L., Hooshmand, M., Summers, R., Gage, F. H., & Anderson, A. J. (2005). Human neural stem cells differentiate and promote locomotor recovery in spinal cord-injured mice. *Proc Natl Acad Sci U S A, 102*(39), 14069-14074.

8. Okano, H., Ogawa, Y., Nakamura, M., Kaneko, S., Iwanami, A., & Toyama, Y. (2003). Transplantation of neural stem cells into the spinal cord after injury. *Semin Cell Dev Biol, 14*(3), 191-198.

9. French, D. D., Campbell, R. R., Sabharwal, S., Nelson, A. L., Palacios, P. A., & Gavin-Dreschnack, D. (2007). Health care costs for patients with chronic spinal cord injury in the Veterans Health Administration. *J Spinal Cord Med, 30*(5), 477-481.

10. Kerschensteiner, M., Schwab, M. E., Lichtman, J. W., & Misgeld, T. (2005). In vivo imaging of axonal degeneration and regeneration in the injured spinal cord. *Nat Med, 11*(5), 572-577.

11. Rolls, A., Shechter, R., & Schwartz, M. (2009). The bright side of the glial scar in CNS repair. *Nat Rev Neurosci, 10*(3), 235-241.

12. Neumann, S., Skinner, K., & Basbaum, A. I. (2005). Sustaining intrinsic growth capacity of adult neurons promotes spinal cord regeneration. *Proc Natl Acad Sci U S A, 102*(46), 16848-16852.

13. Neumann, S., Bradke, F., Tessier-Lavigne, M., & Basbaum, A. I. (2002). Regeneration of sensory axons within the injured spinal cord induced by intraganglionic cAMP elevation. *Neuron, 34*(6), 885-893.

14. Qiu, J., Cai, D., Dai, H., McAtee, M., Hoffman, P. N., Bregman, B. S., & Filbin, M. T. (2002). Spinal axon regeneration induced by elevation of cyclic AMP. *Neuron, 34*(6), 895-903.

15. Romero, M. I., Rangappa, N., Garry, M. G., & Smith, G. M. (2001). Functional regeneration of chronically injured sensory afferents into adult spinal cord after neurotrophin gene therapy. *J Neurosci, 21*(21), 8408-8416.

16. Ramer, M. S., Priestley, J. V., & McMahon, S. B. (2000). Functional regeneration of sensory axons into the adult spinal cord. *Nature, 403*(6767), 312-316.

17. Lu, P., Jones, L. L., Snyder, E. Y., & Tuszynski, M. H. (2003). Neural stem cells constitutively secrete neurotrophic factors and promote extensive host axonal growth after spinal cord injury. *Exp Neurol, 181*(2), 115-129.

18. Pallini, R., Vitiani, L. R., Bez, A., Casalbore, P., Facchiano, F., Di Giorgi Gerevini, V., Falchetti, M. L., Fernandez, E., Maira, G., Peschle, C., & Parati, E. (2005). Homologous transplantation of neural stem cells to the injured spinal cord of mice. *Neurosurgery, 57*(5), 1014-1025; discussion 1014-1025.

19. Gelain, F., Panseri, S., Antonini, S., Cunha, C., Donega, M., Lowery, J., Taraballi, F., Cerri, G., Montagna, M., Baldissera, F., & Vescovi, A. (2011). Transplantation of nanostructured composite scaffolds results in the regeneration of chronically injured spinal cords. *ACS Nano, 5*(1), 227-236.

20. Chen, G., Hu, Y. R., Wan, H., Xia, L., Li, J. H., Yang, F., Qu, X., Wang, S. G., & Wang, Z. C. (2010). Functional recovery following traumatic spinal cord injury mediated by a unique polymer scaffold seeded with neural stem cells and Schwann cells. *Chin Med J (Engl), 123*(17), 2424-2431.

21. Teng, Y. D., Lavik, E. B., Qu, X., Park, K. I., Ourednik, J., Zurakowski, D., Langer, R., & Snyder, E. Y. (2002). Functional recovery following traumatic

spinal cord injury mediated by a unique polymer scaffold seeded with neural stem cells. *Proc Natl Acad Sci U S A, 99*(5), 3024-3029.

22. Deumens, R., Koopmans, G. C., Honig, W. M., Maquet, V., Jérôme, R., Steinbusch, H. W., & Joosten, E. A. (2006). Chronically injured corticospinal axons do not cross large spinal lesion gaps after a multifactorial transplantation strategy using olfactory ensheathing cell/olfactory nerve fibroblast-biomatrix bridges. *J Neurosci Res, 83*(5), 811-820.

23. Petri-Fink, A., & Hofmann, H. (2007). Superparamagnetic iron oxide nanoparticles (SPIONs): from synthesis to in vivo studies--a summary of the synthesis, characterization, in vitro, and in vivo investigations of SPIONs with particular focus on surface and colloidal properties. *IEEE Trans Nanobioscience, 6*(4), 289-297.

24. Dobson, J. (2008). Remote control of cellular behaviour with magnetic nanoparticles. *Nat Nanotechnol, 3*(3), 139-143.

25. Lin, M. M., Kim, D. K., El Haj, A. J., & Dobson, J. (2008). Development of superparamagnetic iron oxide nanoparticles (SPIONS) for translation to clinical applications. *IEEE Trans Nanobioscience, 7*(4), 298-305.

26. Rosengart, A. J., Kaminski, M. D., Chen, H., Caviness, P. L., Ebner, A. D., & Ritter, J. A. (2005). Magnetizable implants and functionalized magnetic carriers: A novel approach for noninvasive yet targeted drug delivery. *Journal of Magnetism and Magnetic Materials, 293*(1), 633-638.

27. Gneveckow, U., Jordan, A., Scholz, R., Brüss, V., Waldöfner, N., Ricke, J., Feussner, A., Hildebrandt, B., Rau, B., & Wust, P. (2004). Description and

characterization of the novel hyperthermia- and thermoablation-system MFH 300F for clinical magnetic fluid hyperthermia. *Med Phys, 31*(6), 1444-1451.

28. Sigal, R., Vogl, T., Casselman, J., Moulin, G., Veillon, F., Hermans, R., Dubrulle, F., Viala, J., Bosq, J., Mack, M., Depondt, M., Mattelaer, C., Petit, P., Champsaur, P., Riehm, S., Dadashitazehozi, Y., de Jaegere, T., Marchal, G., Chevalier, D., Lemaitre, L., Kubiak, C., Helmberger, R., & Halimi, P. (2002). Lymph node metastases from head and neck squamous cell carcinoma: MR imaging with ultrasmall superparamagnetic iron oxide particles (Sinerem MR) -- results of a phase-III multicenter clinical trial. *Eur Radiol, 12*(5), 1104-1113.

29. Kalish, H., Arbab, A. S., Miller, B. R., Lewis, B. K., Zywicke, H. A., Bulte, J. W., Bryant, L. H., Jr., & Frank, J. A. (2003). Combination of transfection agents and magnetic resonance contrast agents for cellular imaging: relationship between relaxivities, electrostatic forces, and chemical composition. *Magn Reson Med, 50*(2), 275-282.

30. Hughes, S., Dobson, J., & El Haj, A. J. (2007). Magnetic targeting of mechanosensors in bone cells for tissue engineering applications. *J Biomech, 40 Suppl 1*, S96-104.

31. Hughes, S., El Haj, A. J., & Dobson, J. (2005). Magnetic micro- and nanoparticle mediated activation of mechanosensitive ion channels. *Med Eng Phys, 27*(9), 754-762.

32. Hughes, S., McBain, S., Dobson, J., & El Haj, A. J. (2008). Selective activation of mechanosensitive ion channels using magnetic particles. *J R Soc Interface, 5*(25), 855-863.

33. Melle, S., Rubio, M. A., & Fuller, G. G. (2001). Time scaling regimes in aggregation of magnetic dipolar particles: scattering dichroism results. *Phys Rev Lett, 87*(11), 115501.

34. Wen, W., Zhang, L., & Sheng, P. (2000). Planar magnetic colloidal crystals. *Phys Rev Lett, 85*(25), 5464-5467.

35. Alsberg, E., Feinstein, E., Joy, M. P., Prentiss, M., & Ingber, D. E. (2006). Magnetically-guided self-assembly of fibrin matrices with ordered nano-scale structure for tissue engineering. *Tissue Eng, 12*(11), 3247-3256.

36. Jing, Y., Mal, N., Williams, P. S., Mayorga, M., Penn, M. S., Chalmers, J. J., & Zborowski, M. (2008). Quantitative intracellular magnetic nanoparticle uptake measured by live cell magnetophoresis. *Faseb j, 22*(12), 4239-4247.

37. Bulte, J. W., Laughlin, P. G., Jordan, E. K., Tran, V. A., Vymazal, J., & Frank, J. A. (1996). Tagging of T cells with superparamagnetic iron oxide: uptake kinetics and relaxometry. *Acad Radiol, 3 Suppl 2*, S301-303.

38. Sipe, J. C., Filippi, M., Martino, G., Furlan, R., Rocca, M. A., Rovaris, M., Bergami, A., Zyroff, J., Scotti, G., & Comi, G. (1999). Method for intracellular magnetic labeling of human mononuclear cells using approved iron contrast agents. *Magn Reson Imaging, 17*(10), 1521-1523.

39. Soenen, S. J., Hodenius, M., & De Cuyper, M. (2009). Magnetoliposomes: versatile innovative nanocolloids for use in biotechnology and biomedicine. *Nanomedicine (Lond), 4*(2), 177-191.

40. Soenen, S. J., Baert, J., & De Cuyper, M. (2007). Optimal conditions for labelling of 3T3 fibroblasts with magnetoliposomes without affecting cellular viability. *Chembiochem, 8*(17), 2067-2077.

41. De Cuyper, M., & Joniau, M. (1988). Magnetoliposomes. Formation and structural characterization. *Eur Biophys J, 15*(5), 311-319.

42. Chen, Y., Bose, A., & Bothun, G. D. (2010). Controlled release from bilayer-decorated magnetoliposomes via electromagnetic heating. *ACS Nano, 4*(6), 3215-3221.

43. Bangham, A. D., & Horne, R. W. (1964). Negative staining of phospholipids and their structural modification by surface-active agents as observed in the electron microscope. *J Mol Biol, 8*, 660-668.

44. Deb, P. K., Al-Attraqchi, O., Chandrasekaran, B., Paradkar, A., & Tekade, R. K. (2019). Chapter 16 - Protein/Peptide Drug Delivery Systems: Practical Considerations in Pharmaceutical Product Development. In R. K. Tekade (Ed.), *Basic Fundamentals of Drug Delivery* (pp. 651-684): Academic Press.

45. Akbarzadeh, A., Rezaei-Sadabady, R., Davaran, S., Joo, S. W., Zarghami, N., Hanifehpour, Y., Samiei, M., Kouhi, M., & Nejati-Koshki, K. (2013). Liposome: classification, preparation, and applications. *Nanoscale Res Lett, 8*(1), 102.

46. Waterhouse, D. N., Madden, T. D., Cullis, P. R., Bally, M. B., Mayer, L. D., & Webb, M. S. (2005). Preparation, characterization, and biological analysis of liposomal formulations of vincristine. *Methods Enzymol, 391*, 40-57.

47. Rojanapanthu, P., Sarisuta, N., Chaturon, K., & Kraisintu, K. (2003). Physicochemical properties of amphotericin B liposomes prepared by reverse-phase evaporation method. *Drug Dev Ind Pharm, 29*(1), 31-37.

48. Deamer, D. W. (1978). Preparation and properties of ether-injection liposomes. *Ann N Y Acad Sci, 308*, 250-258.

49. Pereno, V., Carugo, D., Bau, L., Sezgin, E., Bernardino de la Serna, J., Eggeling, C., & Stride, E. (2017). Electroformation of Giant Unilamellar Vesicles on Stainless Steel Electrodes. *ACS Omega, 2*(3), 994-1002.

50. Bangham, A. D., Standish, M. M., & Watkins, J. C. (1965). Diffusion of univalent ions across the lamellae of swollen phospholipids. *J Mol Biol, 13*(1), 238-252.

51. Mortazavi, S. M., Mohammadabadi, M. R., Khosravi-Darani, K., & Mozafari, M. R. (2007). Preparation of liposomal gene therapy vectors by a scalable method without using volatile solvents or detergents. *J Biotechnol, 129*(4), 604-613.

52. Szoka, F., Jr., & Papahadjopoulos, D. (1978). Procedure for preparation of liposomes with large internal aqueous space and high capture by reverse-phase evaporation. *Proc Natl Acad Sci U S A, 75*(9), 4194-4198.

53. Pautot, S., Frisken, B. J., & Weitz, D. A. (2003). Production of Unilamellar Vesicles Using an Inverted Emulsion. *Langmuir, 19*(7), 2870-2879.

54. Souza, G. R., Molina, J. R., Raphael, R. M., Ozawa, M. G., Stark, D. J., Levin, C. S., Bronk, L. F., Ananta, J. S., Mandelin, J., Georgescu, M. M., Bankson, J. A., Gelovani, J. G., Killian, T. C., Arap, W., & Pasqualini, R. (2010). Three-

dimensional tissue culture based on magnetic cell levitation. *Nat Nanotechnol, 5*(4), 291-296.

55. Souza, G. R., Christianson, D. R., Staquicini, F. I., Ozawa, M. G., Snyder, E. Y., Sidman, R. L., Miller, J. H., Arap, W., & Pasqualini, R. (2006). Networks of gold nanoparticles and bacteriophage as biological sensors and cell-targeting agents. *Proc Natl Acad Sci U S A, 103*(5), 1215-1220.

56. Tseng, H., Gage, J. A., Shen, T., Haisler, W. L., Neeley, S. K., Shiao, S., Chen, J., Desai, P. K., Liao, A., Hebel, C., Raphael, R. M., Becker, J. L., & Souza, G. R. (2015). A spheroid toxicity assay using magnetic 3D bioprinting and real-time mobile device-based imaging. *Sci Rep, 5*, 13987.

57. Zafar, M. S., Ullah, R., Qamar, Z., Fareed, M. A., Amin, F., Khurshid, Z., & Sefat, F. (2019). 2 - Properties of dental biomaterials. In Z. Khurshid, S. Najeeb, M. S. Zafar, & F. Sefat (Eds.), *Advanced Dental Biomaterials* (pp. 7-35): Woodhead Publishing.

58. Anderson, J. M., & Voskerician, G. (2010). 14 - The challenge of biocompatibility evaluation of biocomposites. In L. Ambrosio (Ed.), *Biomedical Composites* (pp. 325-353): Woodhead Publishing.

59. Souza, G. R., Yonel-Gumruk, E., Fan, D., Easley, J., Rangel, R., Guzman-Rojas, L., Miller, J. H., Arap, W., & Pasqualini, R. (2008). Bottom-up assembly of hydrogels from bacteriophage and Au nanoparticles: the effect of cis- and trans-acting factors. *PLoS One, 3*(5), e2242.

60. Tseng, H., Gage, J. A., Raphael, R. M., Moore, R. H., Killian, T. C., Grande-Allen, K. J., & Souza, G. R. (2013). Assembly of a three-dimensional multitype

bronchiole coculture model using magnetic levitation. *Tissue Eng Part C Methods, 19*(9), 665-675.

61. Castro-Chavez, F., Vickers, K. C., Lee, J. S., Tung, C. H., & Morrisett, J. D. (2013). Effect of lyso-phosphatidylcholine and Schnurri-3 on osteogenic transdifferentiation of vascular smooth muscle cells to calcifying vascular cells in 3D culture. *Biochim Biophys Acta, 1830*(6), 3828-3834.

62. Daquinag, A. C., Souza, G. R., & Kolonin, M. G. (2013). Adipose tissue engineering in three-dimensional levitation tissue culture system based on magnetic nanoparticles. *Tissue Eng Part C Methods, 19*(5), 336-344.

63. Weyhe, D., Hoffmann, P., Belyaev, O., Mros, K., Muller, C., Uhl, W., & Schmitz, F. (2007). The role of TGF-beta1 as a determinant of foreign body reaction to alloplastic materials in rat fibroblast cultures: comparison of different commercially available polypropylene meshes for hernia repair. *Regul Pept, 138*(1), 10-14.

64. Raffaelli, L., Rossi Iommetti, P., Piccioni, E., Toesca, A., Serini, S., Resci, F., Missori, M., De Spirito, M., Manicone, P. F., & Calviello, G. (2008). Growth, viability, adhesion potential, and fibronectin expression in fibroblasts cultured on zirconia or feldspatic ceramics in vitro. *J Biomed Mater Res A, 86*(4), 959-968.

65. Viney, M. E., Bullock, A. J., Day, M. J., & MacNeil, S. (2009). Co-culture of intestinal epithelial and stromal cells in 3D collagen-based environments. *Regen Med, 4*(3), 397-406.

66. Bioarray, C. Trypan Blue Staining Assay. Retrieved from https://www.creative-bioarray.com/support/trypan-blue-staining-assay.htm

67. Riss, T. L., Moravec, R. A., Niles, A. L., Duellman, S., Benink, H. A., Worzella, T. J., & Minor, L. (2004). Cell Viability Assays. In S. Markossian, G. S. Sittampalam, A. Grossman, K. Brimacombe, M. Arkin, D. Auld, C. P. Austin, J. Baell, J. M. M. Caaveiro, T. D. Y. Chung, N. P. Coussens, J. L. Dahlin, V. Devanaryan, T. L. Foley, M. Glicksman, M. D. Hall, J. V. Haas, S. R. J. Hoare, J. Inglese, P. W. Iversen, S. D. Kahl, S. C. Kales, S. Kirshner, M. Lal-Nag, Z. Li, J. McGee, O. McManus, T. Riss, P. Saradjian, O. J. Trask, Jr., J. R. Weidner, M. J. Wildey, M. Xia, & X. Xu (Eds.), *Assay Guidance Manual*. Bethesda (MD): Eli Lilly & Company and the National Center for Advancing Translational Sciences.

68. Todaro, G. J., & Green, H. (1963). Quantitative studies of the growth of mouse embryo cells in culture and their development into established lines. *J Cell Biol, 17*(2), 299-313.

69. Rose, S. P., Pruss, R. M., & Herschman, H. R. (1975). Initiation of 3T3 fibroblast cell division by epidermal growth factor. *J Cell Physiol, 86 Suppl 2*(3 Pt 2), 593-598.

70. Bhandari, R. N., Riccalton, L. A., Lewis, A. L., Fry, J. R., Hammond, A. H., Tendler, S. J., & Shakesheff, K. M. (2001). Liver tissue engineering: a role for co-culture systems in modifying hepatocyte function and viability. *Tissue Eng, 7*(3), 345-357.

71. Kirby, L., Jin, J., Cardona, J. G., Smith, M. D., Martin, K. A., Wang, J., Strasburger, H., Herbst, L., Alexis, M., Karnell, J., Davidson, T., Dutta, R., Goverman, J., Bergles, D., & Calabresi, P. A. (2019). Oligodendrocyte precursor cells present antigen and are cytotoxic targets in inflammatory demyelination. *Nat Commun, 10*(1), 3887.

72. Nishiyama, A., Komitova, M., Suzuki, R., & Zhu, X. (2009). Polydendrocytes (NG2 cells): multifunctional cells with lineage plasticity. *Nat Rev Neurosci, 10*(1), 9-22.

73. Cukierman, E., Pankov, R., Stevens, D. R., & Yamada, K. M. (2001). Taking cell-matrix adhesions to the third dimension. *Science, 294*(5547), 1708-1712.

74. Abbott, A. (2003). Cell culture: biology's new dimension. *Nature, 424*(6951), 870-872.

75. Pampaloni, F., Reynaud, E. G., & Stelzer, E. H. K. (2007). The third dimension bridges the gap between cell culture and live tissue. *Nature Reviews Molecular Cell Biology, 8*(10), 839-845.

76. Griffith, L. G., & Swartz, M. A. (2006). Capturing complex 3D tissue physiology in vitro. *Nat Rev Mol Cell Biol, 7*(3), 211-224.

77. Atala, A. (2007). Engineering tissues, organs and cells. *J Tissue Eng Regen Med, 1*(2), 83-96.

78. Harunaga, J. S., & Yamada, K. M. (2011). Cell-matrix adhesions in 3D. *Matrix Biol, 30*(7-8), 363-368.

79. Zhang, S. (2004). Beyond the Petri dish. *Nat Biotechnol, 22*(2), 151-152.

80. Nakamura, M., Toyama, Y., & Okano, H. (2005). Transplantation of neural stem cells for spinal cord injury. *Rinsho shinkeigaku = Clinical neurology, 45*(11), 874-876.

81. Takeuchi, H., Natsume, A., Wakabayashi, T., Aoshima, C., Shimato, S., Ito, M., Ishii, J., Maeda, Y., Hara, M., Kim, S. U., & Yoshida, J. (2007). Intravenously transplanted human neural stem cells migrate to the injured spinal cord in adult mice in an SDF-1- and HGF-dependent manner. *Neuroscience Letters, 426*(2), 69-74.

82. Li, J., Sun, C. R., Zhang, H., Tsang, K. S., Li, J. H., Zhang, S. D., & An, Y. H. (2007). Induction of functional recovery by co-transplantation of neural stem cells and Schwann cells in a rat spinal cord contusion injury model. *Biomed Environ Sci, 20*(3), 242-249.

83. Kornblum, H. I. (2007). Introduction to neural stem cells. *Stroke, 38*(2 Suppl), 810-816.

84. Clarke, D. L., Johansson, C. B., Wilbertz, J., Veress, B., Nilsson, E., Karlström, H., Lendahl, U., & Frisén, J. (2000). Generalized potential of adult neural stem cells. *Science, 288*(5471), 1660-1663.

85. Zheng, K., Liu, T. Q., Dai, M. S., Ge, D., Li, X. Q., Ma, X. H., & Cui, Z. F. (2006). Comparison of different culture modes for long-term expansion of neural stem cells. *Cytotechnology, 52*(3), 209-218.

86. Ge, J., Wood, D. K., Weingeist, D. M., Prasongtanakij, S., Navasumrit, P., Ruchirawat, M., & Engelward, B. P. (2013). Standard fluorescent imaging of

live cells is highly genotoxic. *Cytometry. Part A : the journal of the International Society for Analytical Cytology, 83*(6), 552-560.

87. Shao, B., Zlatanovic, S., Ozkan, M., Birkbeck, A. L., & Esener, S. C. (2006). Manipulation of microspheres and biological cells with multiple agile VCSEL traps. *Sensors and Actuators B: Chemical, 113*(2), 866-874.

88. Huang, S. B., Wu, M. H., Lin, Y. H., Hsieh, C. H., Yang, C. L., Lin, H. C., Tseng, C. P., & Lee, G. B. (2013). High-purity and label-free isolation of circulating tumor cells (CTCs) in a microfluidic platform by using optically-induced-dielectrophoretic (ODEP) force. *Lab Chip, 13*(7), 1371-1383.

89. Lilliehorn, T., Simu, U., Nilsson, M., Almqvist, M., Stepinski, T., Laurell, T., Nilsson, J., & Johansson, S. (2005). Trapping of microparticles in the near field of an ultrasonic transducer. *Ultrasonics, 43*(5), 293-303.

90. Tanyeri, M., & Schroeder, C. M. (2013). Manipulation and confinement of single particles using fluid flow. *Nano letters, 13*(6), 2357-2364.

91. Voldman, J. (2006). Electrical forces for microscale cell manipulation. *Annu Rev Biomed Eng, 8*, 425-454.

92. Jubery, T. Z., Srivastava, S. K., & Dutta, P. (2014). Dielectrophoretic separation of bioparticles in microdevices: a review. *Electrophoresis, 35*(5), 691-713.

93. Qian, C., Huang, H., Chen, L., Li, X., Ge, Z., Chen, T., Yang, Z., & Sun, L. (2014). Dielectrophoresis for bioparticle manipulation. *Int J Mol Sci, 15*(10), 18281-18309.

94. Pamme, N., & Manz, A. (2004). On-Chip Free-Flow Magnetophoresis: Continuous Flow Separation of Magnetic Particles and Agglomerates. *Analytical Chemistry, 76*(24), 7250-7256.

95. Williams, P. S., Carpino, F., & Zborowski, M. (2010). Characterization of magnetic nanoparticles using programmed quadrupole magnetic field-flow fractionation. *Philosophical Transactions of the Royal Society A: Mathematical, Physical and Engineering Sciences, 368*(1927), 4419-4437.

96. Yang, R.-J., Hou, H.-H., Wang, Y.-N., & Fu, L.-M. (2016). Micro-magnetofluidics in microfluidic systems: A review. *Sensors and Actuators B: Chemical, 224*, 1-15.

97. Rezk, A., Friend, J., & Yeo, L. (2013). 3 - Actuation mechanisms for microfluidic biomedical devices. In X. Li & Y. Zhou (Eds.), *Microfluidic Devices for Biomedical Applications* (pp. 100-138): Woodhead Publishing.

98. Ali, M., Ostrikov, K., Abdul Khalid, F., Majlis, B., & Kayani, A. (2016). Active Bioparticle Manipulation in Microfluidic Systems. *RSC Advances, 6*.

99. Grimnes, S., & Martinsen, Ø. G. (2015). Chapter 7 - Electrodes. In S. Grimnes & Ø. G. Martinsen (Eds.), *Bioimpedance and Bioelectricity Basics (Third Edition)* (pp. 179-254). Oxford: Academic Press.

100. Gascoyne, P. R. C., Huang, Y., Pethig, R., Vykoukal, J., & Becker, F. F. (1992). Dielectrophoretic separation of mammalian cells studied by computerized image analysis. *Measurement Science and Technology, 3*(5), 439-445.

101. Pohl, H. A., Pollock, K., & Crane, J. S. (1978). Dielectrophoretic force: A comparison of theory and experiment. *Journal of Biological Physics, 6*(3), 133-160.

102. Jones, T. B. (1995). *Electromechanics of Particles*. Cambridge: Cambridge University Press.

103. Morgan, H., Izquierdo, A. G., Bakewell, D., Green, N. G., & Ramos, A. (2001). The dielectrophoretic and travelling wave forces generated by interdigitated electrode arrays: analytical solution using Fourier series. *Journal of Physics D: Applied Physics, 34*(10), 1553-1561.

104. Wang, X., Wang, X.-B., & Gascoyne, P. R. C. (1997). General expressions for dielectrophoretic force and electrorotational torque derived using the Maxwell stress tensor method. *Journal of Electrostatics, 39*(4), 277-295.

105. Griffiths, D. J. (2017). *Introduction to Electrodynamics* (4 ed.). Cambridge: Cambridge University Press.

106. Pethig, R. (2010). Review article-dielectrophoresis: status of the theory, technology, and applications. *Biomicrofluidics, 4*(2), 022811.

107. Jones, T. B. (2003). Basic theory of dielectrophoresis and electrorotation. *IEEE Eng Med Biol Mag, 22*(6), 33-42.

108. Cetin, B., & Li, D. (2011). Dielectrophoresis in microfluidics technology. *Electrophoresis, 32*(18), 2410-2427.

109. Antfolk, M., Antfolk, C., Lilja, H., Laurell, T., & Augustsson, P. (2015). A single inlet two-stage acoustophoresis chip enabling tumor cell enrichment from white blood cells. *Lab Chip, 15*(9), 2102-2109.

110. Sridharan, S., Zhu, J., Hu, G., & Xuan, X. (2011). Joule heating effects on electroosmotic flow in insulator-based dielectrophoresis. *Electrophoresis, 32*(17), 2274-2281.

111. Erb, R., & Yellen, B. (2009). Magnetic Manipulation of Colloidal Particles. In (pp. 563-590).

112. Plouffe, B. D., Murthy, S. K., & Lewis, L. H. (2015). Fundamentals and application of magnetic particles in cell isolation and enrichment: a review. *Reports on progress in physics. Physical Society (Great Britain), 78*(1), 016601-016601.

113. Winoto-Morbach, S., Tchikov, V., & Müller-Ruchholtz, W. (1994). Magnetophoresis: I. detection of magnetically labeled cells. *Journal of Clinical Laboratory Analysis, 8*(6), 400-406.

114. Hartig, R., Hausmann, M., Schmitt, J., Herrmann, D. B., Riedmiller, M., & Cremer, C. (1992). Preparative continuous separation of biological particles by means of free-flow magnetophoresis in a free-flow electrophoresis chamber. *Electrophoresis, 13*(9-10), 674-676.

115. Jain, T. K., Richey, J., Strand, M., Leslie-Pelecky, D. L., Flask, C. A., & Labhasetwar, V. (2008). Magnetic nanoparticles with dual functional properties: drug delivery and magnetic resonance imaging. *Biomaterials, 29*(29), 4012-4021.

116. Huh, Y. M., Jun, Y. W., Song, H. T., Kim, S., Choi, J. S., Lee, J. H., Yoon, S., Kim, K. S., Shin, J. S., Suh, J. S., & Cheon, J. (2005). In vivo magnetic

resonance detection of cancer by using multifunctional magnetic nanocrystals. *J Am Chem Soc, 127*(35), 12387-12391.

117. Pankhurst, Q. A., Connolly, J., Jones, S. K., & Dobson, J. (2003). Applications of magnetic nanoparticles in biomedicine. *Journal of Physics D: Applied Physics, 36*(13), R167-R181.

118. Boyer, T. H. (1988). The force on a magnetic dipole. *American Journal of Physics, 56*(8), 688-692.

119. Kurgan, E., & Gas, P. (2018, 18-22 June 2018). *Methods of Calculation the Magnetic Forces Acting on Particles in Magnetic Fluids.* Paper presented at the 2018 Progress in Applied Electrical Engineering (PAEE).

120. Kang, S., & Suh, Y. K. (2011). Direct simulation of flows with suspended paramagnetic particles using one-stage smoothed profile method. *Journal of Fluids and Structures, 27*(2), 266-282.

121. Reddy, J. N., & Gartling, D. K. (2010). *The finite element method in heat transfer and fluid dynamics third edition*.

122. Jin, J. (2014). *The Finite Element Method in Electromagnetics*: Wiley-IEEE Press.

123. Zienkiewicz, O. C., Taylor, R. L., & Fox, D. (2014). Chapter 1 - General Problems in Solid Mechanics and Nonlinearity. In O. C. Zienkiewicz, R. L. Taylor, & D. Fox (Eds.), *The Finite Element Method for Solid and Structural Mechanics (Seventh Edition)* (pp. 1-20). Oxford: Butterworth-Heinemann.

124. Rosato, D., & Rosato, D. (2003). 5 - COMPUTER-AIDED DESIGN. In D. Rosato & D. Rosato (Eds.), *Plastics Engineered Product Design* (pp. 344-380). Amsterdam: Elsevier Science.

125. O.C, Z., Taylor, R., & Zhu, J. (2005). *The Finite Element Method: Its Basis and Fundamentals* (Vol. I).

126. Li, Q., Ito, K., Wu, Z., Lowry, C., & Loheide, S. (2009). COMSOL Multiphysics: A novel approach to ground water modeling. *Ground water, 47*.

127. Dickinson, E., Ekström, H., & Fontes, E. (2014). COMSOL Multiphysics (R) : Finite element software for electrochemical analysis. A mini-review. *Electrochemistry Communications, 40*, 71–74.

128. Dukowicz, J. K., & Kodis, J. W. (1987). Accurate conservative remapping (rezoning) for arbitrary Lagrangian-Eulerian computations.

129. Glowinski, R., Pan, T. W., Hesla, T. I., & Joseph, D. D. (1999). A distributed Lagrange multiplier/fictitious domain method for particulate flows. *International Journal of Multiphase Flow, 25*(5), 755-794.

130. Suehiro, J., & Pethig, R. (1998). The dielectrophoretic movement and positioning of a biological cell using a three-dimensional grid electrode system. *Journal of Physics D: Applied Physics, 31*(22), 3298-3305.

131. Morgan, H., & Green, N. (2003). AC electrokinetics: colloids and nanoparticles. In.

132. Velev, O. D., & Bhatt, K. H. (2006). On-chip micromanipulation and assembly of colloidal particles by electric fields. *Soft Matter, 2*(9), 738-750.

133. Simonova, T. S., Shilov, V. N., & Shramko, O. A. (2001). Low-Frequency Dielectrophoresis and the Polarization Interaction of Uncharged Spherical Particles with an Induced Debye Atmosphere of Arbitrary Thickness. *Colloid Journal, 63*(1), 108-115.

134. Kang, K. H., & Li, D. (2006). Dielectric Force and Relative Motion between Two Spherical Particles in Electrophoresis. *Langmuir, 22*(4), 1602-1608.

135. Wilson, H. J., Pietraszewski, L. A., & Davis, R. H. (2000). Aggregation of Charged Particles under Electrophoresis or Gravity at Arbitrary Péclet Numbers. *Journal of Colloid and Interface Science, 221*(1), 87-103.

136. van der Zande, B. M. I., Koper, G. J. M., & Lekkerkerker, H. N. W. (1999). Alignment of Rod-Shaped Gold Particles by Electric Fields. *The Journal of Physical Chemistry B, 103*(28), 5754-5760.

137. Kretschmer, R., & Fritzsche, W. (2004). Pearl Chain Formation of Nanoparticles in Microelectrode Gaps by Dielectrophoresis. *Langmuir, 20*(26), 11797-11801.

138. Liu, L., Xie, C., Chen, B., & Wu, J. (2016). Numerical study of particle chains of a large number of randomly distributed DEP particles using iterative dipole moment method. *Journal of Chemical Technology & Biotechnology, 91*(4), 1149-1156.

139. Pohl, H. A. A., Mauro. (1980). Dielectrophoresis: The Behavior of Neutral Matter in Nonuniform Electric Fields. . *The Quarterly Review of Biology, 55*(1), 68-69.

140. Zborowski, M., & Chalmers, J. J. (2015). Magnetophoresis: Fundamentals and Applications. 1-23.

141. Kang, S., & Maniyeri, R. (2012). Dielectrophoretic motions of multiple particles and their analogy with the magnetophoretic counterparts. *Journal of Mechanical Science and Technology, 26*(11), 3503-3513.

142. Zhang, J., Luijten, E., & Granick, S. (2015). Toward design rules of directional janus colloidal assembly. *Annu Rev Phys Chem, 66*, 581-600.

143. Lash, M. H., Fedorchak, M. V., McCarthy, J. J., & Little, S. R. (2015). Scaling up self-assembly: bottom-up approaches to macroscopic particle organization. *Soft Matter, 11*(28), 5597-5609.

144. Wan, Y., & Keh, H. (2010). Electrophoresis of an axisymmetric particle along its axis of revolution perpendicular to two parallel plane walls. *Microfluidics and Nanofluidics, 9*, 623-634.

145. Nunes, J., Herlihy, K. P., Mair, L., Superfine, R., & DeSimone, J. M. (2010). Multifunctional shape and size specific magneto-polymer composite particles. *Nano letters, 10*(4), 1113-1119.

146. Glotzer, S. C., & Solomon, M. J. (2007). Anisotropy of building blocks and their assembly into complex structures. *Nature Materials, 6*(8), 557-562.

147. Morozov, K. I., & Leshansky, A. M. (2014). The chiral magnetic nanomotors. *Nanoscale, 6*(3), 1580-1588.

148. Zhang, L., Petit, T., Peyer, K. E., & Nelson, B. J. (2012). Targeted cargo delivery using a rotating nickel nanowire. *Nanomedicine: Nanotechnology, Biology and Medicine, 8*(7), 1074-1080.

149. Cappallo, N., Lapointe, C., Reich, D. H., & Leheny, R. L. (2007). Nonlinear microrheology of wormlike micelle solutions using ferromagnetic nanowire probes. *Physical Review E, 76*(3), 031505.

150. Helgesen, G., Pieranski, P., & Skjeltorp, A. T. (1990). Nonlinear phenomena in systems of magnetic holes. *Phys Rev Lett, 64*(12), 1425-1428.

151. Helgesen, G., Pieranski, P., & Skjeltorp, A. T. (1990). Dynamic behavior of simple magnetic hole systems. *Physical Review A, 42*(12), 7271-7280.

152. Yang, L., Zhao, N., & Jia, L. (2015). Fluid resistance characteristics research of nanowire rotation under a magnetic field. *Journal of Thermal Science, 24*(1), 73-81.

153. Yang, L., Zhao, N., & Liu, D. (2015). Dynamics of ferromagnetic nanowires in a rotating magnetic field. *Advances in Mechanical Engineering, 7*(7), 1687814015589686.